BLOCH OSCILLATIONS OF COLD ATOMS IN A CAVITY

BLOCH OSCILLATIONS OF COLD ATOMS IN A CAVITY

By

PRASANNA VENKATESH BALASUBRAMANIAN, M.Sc.

A Thesis
Submitted to the School of Graduate Studies
in Partial Fulfillment of the Requirements
for the Degree
Doctor of Philosophy

McMaster University

DOCTOR OF PHILOSOPHY (2012) McMaster University
(Physics) Hamilton, Ontario

TITLE: Bloch oscillations of cold atoms in a cavity

AUTHOR: Prasanna Venkatesh Balasubramanian, M.Sc.(McMaster University)

SUPERVISOR: Dr. D. H. J. O'Dell

NUMBER OF PAGES: xx, 144

Preface

This thesis is a compilation of the research work completed during my Ph.D. studies since September 2008 under the supervision of Dr. Duncan O'Dell in the Department of Physics & Astronomy at McMaster University. The thesis is broadly concerned with the theoretical study of ultracold atoms confined inside an optical cavity. Although cavity quantum electrodynamics (cQED) is a relatively old discipline, the development of high quality optical cavities and the ability to cool and manipulate atoms using laser light is a more recent advance. This has stimulated quite a lot of theoretical and experimental research in the last two decades. Study of atom-cavity systems in the strong coupling regime where a single atom can strongly influence the intracavity light field and vice-versa are now routinely done by many research groups around the world. Atom-cavity systems in the strong coupling regime offer a simple, controllable setting to study various fundamental aspects of quantum mechanics and are also promising candidate systems for quantum information processing. An important feature of this system is the open nature of the cavity, i.e. the system of interest is always in contact with an external bath of electromagnetic modes via the partially transmissive cavity mirrors. This means the outcoupled cavity light field provides an interesting way to measure and manipulate the atomic system. This aspect of cQED is important to the main problem I worked on during my PhD, where we proposed a continuous and non-destructive method to probe the Bloch oscillation dynamics of atoms in the cavity potential by measurement of the light transmitted through the cavity.

The thesis is organized in the 'sandwich' format with the three middle chapters (Chapters 3,4,5), coming from three publications (two published and one under peer-review at the time of writing), providing the central material ('meat'). Chapters that are papers have their own independent bibliography. The rest of the thesis has a single bibliography at the end of the entire text. The first publication presented concerns the aforementioned measurement scheme to determine the Bloch frequency of ultracold atoms in a cavity subject to an additional linear potential. The idea for this problem came from my supervisor and some of the ground work was carried out during my Masters from 2006-08 ans subsequently continued during my doctoral studies. The paper was co-authored with two other collaborators (M. Trupke & E. A. Hinds) apart from my supervisor and published in 2009. I contributed mainly to the conceptualisation and calculations, and to a lesser extent the writing of the paper. The second publication (Chapter 4) concerns some interesting ramifications of the nonlinear atom-light interaction in ultracold atom-cavity systems. The strong individual interaction between the different atoms and the single mode light field in the cavity leads to an effective mutual interaction between the atoms which are otherwise non-interacting. The idea for this project arose from discussions with one of the co-authors Jonas Larson and my supervisor. I contributed equally

to the conceptualisation, calculations and writing and the paper was published in 2011. The third paper (Chapter 5) presented in the thesis is both a natural extension and a more detailed study of the problem introduced in the first paper (Chapter 2). In the first paper we modelled the light field and atoms as classical fields, whereas in the third paper we consider the dynamics of quantized fluctuations about the classical solutions. This, apart from providing some suggestions regarding the regimes in which the experiment proposed in the first paper would be feasible also uncovers other interesting modifications to the coupled atom-cavity system brought about by including the linear potential. I conceptualised and performed the calculations presented in this paper. The paper was co-authored with my supervisor who also played a significant role in refining and streamlining the subject matter.

Contributed Works

Chapters 3, 4, and 5 in this thesis represent original works written by myself, Prasanna Venkatesh Balasubramanian, in conjunction with my listed co-authors. The submission and publication status is as follows:

Chapter 3: Physical Review A 80, 063834 (2009) (arXiv:0811.3993)
Chapter 4: Physical Review A 83, 063606 (2011) (arXiv:1101.1570)
Chapter 5: Currently under submission in the journal Physical Review A, and is available on the preprint server, arXiv at (arXiv:1212.3594).

All of these works have been produced with and co-authored by my supervisor, Dr. D. H. J. O'Dell. Dr. Edward Hinds and Dr. Michael Trupke co-authored chapter 3 [Physical Review A 80, 063834 (2009)], and Dr. Jonas Larson co-authored chapter 4 [Physical Review A 83, 063606 (2011)].

Material from previously published works have been reformatted to conform to the required thesis guidelines. I grant an irrevocable, non-exclusive license to McMaster University and the National Library of Canada to reproduce this material as part of this thesis.

Abstract

Ultracold atoms in an optical lattice Bloch oscillate when subject to a constant force. In the first work presented in this thesis we have theoretically studied the scenario where the optical lattice potential is provided by the electric field inside an optical cavity. The coherent atom-light interaction in a cavity gives rise to a backaction effect on the light field which can modify the intracavity field amplitude and phase. In our first treatment of this problem we model the cavity light field and atoms by classical fields and solve the coupled atom-light equations of motion. As a result, we find that the amplitude and phase of the transmitted light field is modulated at the Bloch frequency. Remarkably, the Bloch frequency itself is not modified by the backaction. Thus the transmitted light field can be used to observe the oscillations continuously, allowing high-precision measurement with small clouds of atoms.

In the second problem presented in this thesis, we explore the band structure of the steady state solutions of the atom-cavity system. A crucial first step towards determining the band structure is the identification of an energy functional that describes the coupled atom-light system. Although, we do not include direct atom-atom interactions in our models, the coupling of the atoms to the single mode light field of the cavity introduces an effective mutual interaction which is correctly taken into account by the energy functional we introduce. Corresponding to each point in the band there exists a steady state light field associated with an average cavity photon number. The dispersive nonlinear atom-light interaction can lead to bistable solutions for this intracavity photon number. For parameters where the atom-cavity system exhibits bistability, the atomic band structure develops loop structures akin to the ones predicted for Bose-Einstein condensates in ordinary (non-cavity) optical lattices. However, in our case the nonlinearity derives from the cavity backaction rather than from direct interatomic interactions. We find both bi- and tri-stable regimes associated with the lowest band, and show that the multistability we observe can be analysed in terms of swallowtail catastrophes. Dynamic and energetic stability of the meanfield solutions is also studied, and we show that the bistable solutions have, as expected, one unstable and two stable branches. The presence of loops in the band structure can lead to a breakdown in adiabaticity during Bloch oscillations as the entire band is sampled during the dynamics. We therefore use the insight gleaned from this work in choosing parameters for the Bloch oscillation measurement proposal presented in the rest of the thesis.

In the third work presented in the thesis, we go beyond the mean field description and consider effects of the quantised nature of the light and atomic fields. The cavity light field is always in contact with external electromagnetic fields through the partially transmissive mirrors. This coupling to the external modes enters as quantum noise in the dynamics of the intracavity field and can also be viewed as a manifestation of quantum measurement backaction corresponding to the continuous observation of the transmitted light field. We solve the Heisenberg-Langevin equations for linearized fluctuations about the atomic and optical meanfields and examine how this influences the signal-to-

noise ratio of a measurement of external forces using this system. In particular, we investigate the effects of changing the number of atoms, the intracavity lattice depth, and the atom-light coupling strength, and show how resonances between the Bloch oscillation dynamics and the quasiparticle spectrum have a strong influence on the signal-to-noise ratio as well as heating effects. One of the hurdles we overcome along the way is the proper treatment of fluctuations about time-dependent meanfields in the context of cold atom cavity-QED.

To Amma!

Acknowledgements

I would like to thank my supervisor Duncan O'Dell. Over the past seven years I have learnt quite a lot from him. His constant encouragement and faith in my skills, even when I constantly doubted myself, has played a major role in the completion of my graduate studies. His enthusiasm for physics and kindness towards his students are qualities I seek to emulate. I would like to thank Dr. Sung-Sik Lee for being on my supervisory committee. I have been inspired by his approach to Physics and research in general. I would like to thank Dr. Erik Sorensen for being on my supervisory committee and providing invaluable academic and practical advice throughout my graduate studies. I would like to thank all the wonderful teachers from my undergraduate institution, Chennai Mathematical Institute. They have shaped my approach to learning and understanding physics. I would also like to thank Jonas Larson for his encouragement and enthusiastic collaboration on our shared projects. I would like to thank Ed Hinds for his insights into cavity QED in general and our problem in particular. I would like to thank Ed Taylor for many useful discussions regarding the subject matter of my thesis and ultracold atoms in general.

On the personal front, I have to begin by thanking Rajat da and Manju Boudi. Rajat da played a very important role in my move to McMaster and his family have been incredibly generous during my stay in Hamilton. My life in the Physics department has been greatly enriched by the many friends I made at McMaster. In no particular order I would like to thank Allan, Phil, Clare, Andreas, Josh, Sedigh, Saeed, Annie, Rory, Laura, Mark Ilton, Wen and Peter Lunts. I would like to thank Shouvik for his friendship. The many discussions on Physics and other myriad shared interests with Shouvik have made my life more enjoyable and help me grow as a human being (not to mention made us world experts on procrastination). I would like to thank all the staff in the Physics office for being resourceful and helping out with the various administrative tasks.

Outside the Physics department, my time in Hamilton was fun thanks to the great set of friends I made here. Over the years they have become my pillars of support and a second family. Thanks to Nilesh, Kunal, Sneha, Rahul, Chinar, PJ, Manraj, Amol, Aditi, Nishad, Shailesh and Kinjal.

As with every one of my endeavours, my family has been the main source of unflinching support and unconditional love. I cannot thank them enough.

Contents

List of Figures

Chapter 1

Introduction

This thesis concerns a theoretical study of ultracold atoms confined within an optical cavity. The study of matter cooled down to low temperatures has a rich history but in recent times the interest in the field has exploded due to the creation of the first atomic Bose-Einstein condensate (BEC), a macroscopic quantum coherent state, in 1995 [1, 2]. Before the creation of an atomic BEC, superfluidity in liquid helium, superconductivity in materials and the laser were the best known systems where quantum mechanics manifests itself on a macroscopic scale. The ability to control and vary different aspects such as interactions, external potentials and measurement protocols makes BEC systems suitable for testing various fundamental quantum phenomena and also powerful analogue systems to understand aspects of many body physics [3]. A key element used in the control and manipulation of BEC systems is the electromagnetic field of laser light. In cavity quantum electrodynamics (cQED), electromagnetic waves are confined within a small spatial region using mirrors. With the advances made in mirror fabrication and use of different ranges of electromagnetic frequencies (such as microwave and optical frequencies), present day cavities have very high quality factors, i.e. a single photon makes millions of round trips before exiting the cavity. Consequently, the interactions between atoms and the electric field inside a cavity are enhanced greatly compared to free space and the resulting cooperative atom-light behaviour is qualitatively different. This novel system has been used to verify some of the most basic yet counterintuitive predictions of quantum theory [4] and its importance was recognized by the award of the 2012 Nobel Prize (in part) to Serge Haroche who is one of the pioneers of modern cQED.

This thesis investigates Bloch oscillation dynamics of ultracold atoms confined in an optical cavity. To set the stage for the main subject matter of the thesis, in the following section we provide short summaries of the relevant research highlights in ultracold atoms with special emphasis on Bloch oscillations. In the second section we summarize various developments in cQED leading up to the recent experiments that have inspired the subject matter of this thesis. In the final section we give an outline of the different chapters of the thesis.

1.1 Ultracold Atoms- A short survey

The idea that a collection of non-interacting bosons when cooled to very low temperatures would exhibit a spontaneous transition to a BEC state with a macroscopic fraction of the particles occupying the ground state dates back to Einstein [6] closely following the discovery of Bose statistics [5]. In a BEC state, the entire condensed fraction of particles can be described by a single macroscopic quantum wave function. A prerequisite to reach such a state is to ensure that the interparticle separation in the collection of bosons is comparable to the de Broglie wavelength (which increases at lower temperatures) at which point it becomes impossible to distinguish individual quantum particles. A gaseous BEC is not in general the natural ground state of cold atoms since interparticle interactions (especially three body collisions) tend to lead to crystallization at low temperatures. Thus, to realise a BEC it is important to have a dilute enough cloud of atoms (minimising interactions) well isolated and cooled to low enough temperatures. In order to achieve a BEC with a gas of neutral atoms (as eventually done in [1, 2]) it was important to first find ways to manipulate the external states of atoms and move them around.

The elucidation of mechanical effects of laser light in the 1970s, 1980s, and 1990s provided the tools necessary to control the external states of atoms. Lasers provide intense sources of coherent light waves that can cause substantial mechanical effects. Arthur Ashkin's pioneering work in the 70s [7] showing the acceleration and trapping of micron sized latex spheres freely suspended in water set the stage for more sophisticated experiments. Following this Wineland reported the first experimental realisation of radiation pressure induced cooling for trapped Magnesium ions [1] in [8]. This was followed by the demonstration of deceleration of (neutral) sodium atoms by W. Phillips [9]. The first steps towards trapping neutral atoms was taken by Chu and co-workers [11]. Microscopically, the radiation pressure force on neutral atoms arises due to the absorption and spontaneous emission of laser photons. Since the absorption is directed and spontaneous emission has no preferred direction there is a net force in the direction of the laser beam. By using counterpropogating beams tuned near an atomic resonance [11] one can take advantage of the doppler effect: moving atoms tune into resonance with the beam opposing the direction of motion. With three orthogonal pairs of counterpropogating lasers this leads to a a region where the atoms experience a viscous force ('optical molasses') and are confined for several milliseconds. This led to a considerable amount of work devoted to developing trapping schemes for atoms exclusively using laser light by a combination of the radiation pressure force and the dipole force (which arises from the coherent redistribution, via stimulated emission, of photons between counterpropogating laser modes [12]). Although eventually these methods succeeded in trapping significant numbers of atoms and are widely used in present day Far Off-Resonance Trap (FORT) schemes [13], at the time they were not optimal. An important breakthrough in the effort to trap atoms was provided by the invention of the magneto-optical trap

[1] Note that the technology for trapping charged ions using electromagnetic fields [10] was easier to develop than for neutral atoms.

(MOT) [14], where a magnetic field is used to create a position dependent force via the Zeeman shift of the atomic levels in conjunction with a three dimensional optical molasses trap. Moreover, the sensitivity of atomic internal level shifts to the spatially varying polarisation of the light field in a MOT can be cleverly arranged to ensure that the atom continually climbs potential hills (the 'Sisyphus' cooling mechanism [15]). Atoms trapped and cooled in a MOT have temperatures of the order of hundreds of microkelvin which is the limit set by the recoil energy of the atoms from the absorption and spontaneous emission of a single photon. In total the process of laser cooling reduces the temperature of atoms from the hot source temperature of 1000 Kelvin by a remarkable nine orders of magnitude! For a more detailed overview of the development of laser cooling the Nobel lectures of C. Cohen Tannoudji [16], P. Chu [17] and W. D. Phillips [18] can be consulted.

To produce a BEC one needs to go to even lower temperatures than the microkelvin regime achieved with the MOT. The final step is provided by evaporative cooling where the cold atoms from the MOT are loaded into a harmonic trap created using magnetic fields. Following this the most energetic atoms are allowed to leave the trap leaving the remaining atoms with lower average energy to thermalise to a lower temperature. This technique finally resulted in the production of a Rubidium BEC in Colorado [1] and a Sodium BEC at MIT [2]. A comprehensive account of the work leading up to the creation of the first BECs is described in the Nobel lectures of E. A. Cornell, C. Wieman [20] and W. Ketterle [21]. The creation of the first BEC proved to be a watershed event and currently many groups around the world have succeeded in creating atomic traps and/or BEC set-ups [22]. One of the major research themes pursued in ultracold atoms involves the creation of analogues of solid state systems by loading BECs (and quantum degenerate cold fermionic neutral atoms) into periodic laser potentials (the so called optical lattices). Such analogue systems have the ability to provide idealised and controllable versions of the many body hamiltonians that are used to describe interesting co-operative phenomena in solid state systems, which are often not as clean or controllable. This field has come into its own in the last decade and a review of major developments is provided in [23, 24].

1.1.1 Bloch oscillations

When a quantum particle in periodic potential with period d is subject to an additional constant force F, it undergoes Bloch oscillations at a frequency $\omega_B = Fd/\hbar$. This phenomenon was theoretically predicted for the motion of electrons in solids under the influence of an electric field by C. Zener in 1934 [25] following the earlier work of F. Bloch on transport in periodic systems [26]. In solid state systems Bloch oscillations were hard to observe since the presence of lattice defects and impurities causes quick dephasing of Bloch oscillations. In fact, without such relaxation events that destroy Bloch oscillations there would be very little DC conductivity in metals. The first experiments on Bloch oscillations were undertaken in epitaxially grown semiconductor superlattices where direct electric fields were used to generate electronic Bloch oscillations in the THz frequency range [27].

However, the oscillations in these systems are not long lived and typically dephase within a few periods [28]. With the development of laser cooling and trapping it became clear that atoms could be made to behave as highly coherent matter waves. Moreover, the coherent interaction between a two level atom and a laser standing wave with frequency far removed from the atomic level separation sets up, via the AC Stark effect, a periodic potential, a so called optical lattice, for the atomic external degrees of freedom (see Chapter 2 of this thesis for more details), thereby opening the door to study Bloch oscillations with cold atoms.

The typical procedure for studying Bloch oscillations using cold atoms [29]-[36] involves the preparation of a cloud of ultracold atoms in a trapping potential (in some cases a BEC is used but it is not necessary). An optical lattice is then turned on and the temperature of the atoms should be cold enough that they are coherent over at least several lattice sites. The constant force that causes Bloch oscillations can, for example, be provided by the local acceleration due to gravity or by accelerating the optical lattice using a time varying frequency difference between the counterpropogating laser beams. Once the atoms are loaded into the optical lattice, the trap holding the atoms is turned off and the atoms execute Bloch oscillations. After a holding time (which is varied), the optical lattice is switched off and the atom cloud ballistically expands. After some ballistic expansion the atomic position space distribution is *destructively* imaged using a weak resonant probe beam. This time of flight imaging technique is used to reconstruct the atomic momentum space distribution as a function of the holding time. Although in the first reported experiment [29] using cold Rubidium atoms the number of Bloch oscillations that were seen was small, the unique measurement technique provided, for the first time, a direct measurement of the periodically varying momentum distribution during Bloch oscillations.

The initial experiments using cold atoms for Bloch oscillations [29, 30] highlighted the unique advantages of cold atoms systems vis-a-vis solid state systems. Since the Bloch frequency is directly proportional to the force, this sparked a lot of interest in the use of Bloch oscillations for metrology [32, 35]. Since the wavelength of the optical lattice is known to great accuracy, a measurement of the Bloch frequency can be used to get a precise value for the force and for known forces it could be used to measure fundamental physical constants such as the fine structure constant [33, 34]. One important requirement for the use of Bloch oscillations for metrology is to ensure that one can have long lived oscillations with very little dephasing. The main source of dephasing in the initial atomic Bloch oscillation experiments was the collisional interaction between the background thermal cloud and the quantum degenerate component [31]. A second important source of dephasing is the inter-atomic interaction within the quantum degenerate cloud [2]. In [32] degenerate fermions were used to suppress two body collisions by Pauli repulsion. In the group of G. M. Tino [36] collisional dephasing was suppressed using Strontium atoms, which have very small interatomic interactions, and long-lived Bloch oscillations (up to 7000 cycles lasting a few seconds) were obtained. The resulting Bloch

[2] In fact the dephasing rate of Bloch oscillations in an interacting atomic BEC can be used as a probe of the interaction strength [31].

frequency measurement was used to determine the acceleration due to gravity at a sensitivity of parts per million. In recent work by the group of H.-C. Nägerl [39], Feshbach resonances have been used to minimise the atomic interactions and hence control and lower the interaction induced dephasing of Bloch oscillations. With this method they were able to observe about 20,000 Bloch oscillation cycles (lasting about 10 seconds) before dephasing sets in. Furthermore, newer techniques that combine Bloch oscillations with a modulation of the lattice potential have been implemented [37, 38] and provide even better sensitivity in the measurement of forces. A more detailed account of the various cold atom Bloch oscillation experiments are provided in my masters thesis [40].

A common feature of the experiments presented above is the destructive imaging technique, where the cloud has to be prepared in the same initial state after every measurement event. One of the motivations that led to work presented in Chapter 3 is to design an experimental protocol that allows a continuous in-situ measurement of Bloch oscillations.

1.2 Cavity quantum electrodynamics

Cavity quantum electrodynamics (cQED) has its historical origins in an observation [42] by E. M. Purcell regarding the change in the spontaneous emission rate of a nuclear magnetic moment when coupled to the field of a resonant electrical circuit. The so called Purcell enhancement of the spontaneous emission rate occurs because the mode density of electromagnetic field within a cavity, with resonance frequency close to the transition, is different from the free space mode density. The first observation of the Purcell effect in atomic systems was made by S. Haroche in 1983 [43] using sodium atoms in Rydberg states [3] coupled to high quality factor superconducting niobium cavities with frequencies in the higher microwave range. This was followed by demonstrations of the modification of the spontaneous emission rate in cavities operating in the optical frequency regimes [44, 45]. In these early experiments the spontaneous emission rate was changed by a few percent from the free space value. With the atom-cavity field interaction in the perturbative regime the cavity field only slightly modifies the mode density of the electromagnetic vacuum in free space. The important frequencies in a simple model of a two-level atom in a cavity are the single photon Rabi frequency g_0 (see Eq. (2.21) for the exact definition) that characterizes the strength of coherent light-atom interactions [46], γ the spontaneous emission rate and κ the cavity field amplitude damping rate. When the coherent coupling exceeds the dissipation rates the $g_0 \gg \{\gamma, \kappa\}$, one reaches the so called strong coupling regime of cQED. In this regime the coherent dynamics takes place at a much faster rate than the dissipative processes, thereby allowing many coherent absorption and emission cycles of the photon by the atom before the photon is lost from the cavity. As a result, in the strong coupling regime, it is in fact possible to have bound states of a single atom and single photon, an atom-photon molecule [47]. Experimentally, the strong coupling regime was first reached

[3] An atom in a Rydberg state has a valence electron in an excited electronic state with very large principle quantum number

in the experiments of S. Haroche in 1996 [48, 49] in the microwave regime using niobium cavities and Rydberg atoms. In [48], working in the strong coupling limit for a single atom in a weak coherent cavity field, the functional dependence of the Rabi frequency [4] on the photon numbers of the different states that constitute the coherent state was experimentally verified. This provided a direct test of the electric field quantisation in a cavity. In [49] the decoherence of a photon state made from the mesoscopic quantum superposition of states with classically distinct phases, the so called CAT state was observed. A comprehensive summary of the different fundamental experiments performed with microwave cavity systems in the strong coupling cQED regime is described in [4].

In the optical frequency domain, the small wavelength of light means one needs small cavity volumes in order to reach large light field intensities [111]. Since at such small cavity lengths photon losses via the mirrors can be dominant, the development of high quality dielectric mirrors was a decisive step in reaching strong coupling. In the first experiment to reach the strong coupling regime [50], Cesium atoms trapped in a MOT above the cavity were allowed to fall through the cavity. Individual atom transits produced perceptible changes in the transmitted photon current. Since the coherent atom-light coupling in the cavity inherits the position dependence of the cavity mode profile, the transmitted photon current has real time information about atomic dynamics as it passes the cavity. The first experiments to irrefutably show strong coupling behaviour were from H. J. Kimble's group at Caltech in [51] followed closely by G. Rempe's results [52] at Garching. In [51], the modification of the cavity transmission spectrum due to the presence of atoms (the 'Rabi' doublet) was observed. In [52] mechanical forces on cold atoms dropped from a MOT into an optical cavity containing less than one photon on average were inferred using the transmitted photon current through the cavity. At the turn of the century two remarkable experiments [54, 55] illustrated the full development of strong coupling cQED. Improving upon [50], in the Kimble group atoms were trapped within the optical potential of a high finesse cavity with fields containing of order of one photon. From the observed dynamics of the transmitted photon current, real time trajectories of the atoms inside the cavity were reconstructed. This brings into focus an important feature of light-atom interaction in a cavity in the strong coupling regime, namely, the backaction of atoms on the light field is significant. This has to be contrasted with atomic motion in a free-space laser field which acts as a *passive* external potential. Another intuitive way to think about strong coupling in the optical domain is to picture the atom-cavity system as a microscope [54, 55] where the reconstruction of atomic trajectories provides a position measurement of a quantum particle at a resolution of micrometers. These experiments were followed by the development of methods to deterministically deliver atoms from the MOT into a cavity [56, 57]. The idea was to move atoms from the MOT using a translating optical lattice (dubbed the "optical conveyor belt") in a direction transverse to the cavity axis. This enabled the position of atoms in a cavity to be determined with a resolution of less than a micron [58].

[4] Rabi frequency denotes the rate of the coherent population oscillations between the excited and ground state of a two level atom irradiated by an electric field.

Following the demonstration of various facets of strong coupling cQED attention moved on to understanding some unique features of mechanical effects of light on atom dynamics inside the cavity. The same physical phenomena that lead to laser cooling in free space are present for single trapped atoms in a cavity. Moreover the modification of the spontaneous emission rate inside a cavity had already inspired some work examining laser cooling within a cavity [59, 60]. In the strong coupling regime of cQED, a novel cooling mechanism for the motional degrees of freedom of the atoms was uncovered in the theory group of H. Ritsch [61, 62, 63, 64]. Consider a single atom moving in the standing wave potential inside a cavity mode that is far off-resonance from the atomic level difference. In the strong coupling regime, the atomic back action on the light field implies the intracavity light field is dynamically controlled by the atomic position along the axis. Since the cavity field has a finite relaxation rate (set by κ) the atom experiences a velocity dependent retarded potential which can be chosen to damp the atomic motion. Thus, the atomic energy gets entirely drained via the dissipation channel of the cavity mode. Atomic spontaneous emission plays no role in the cooling mechanism since the intracavity field is far off-resonance from the atom. Since this cavity cooling mechanism relies on the dipole force in the far off-resonance limit, there is no exchange of real excitations and hence provides prospects for extension to other polarizable objects with complicated level structures such as molecules [67]. Cavity cooling was experimentally observed by the Rempe group in 2004 [65].

In the recent past, interest in cQED has shifted to understanding and observing many body effects for a collection of atoms placed inside the cavity. In the strong coupling regime one can anticipate co-operative effects, for the back action on the cavity field by one atom will be felt by all the other atoms in the ensemble. Collective light forces were first experimentally observed by the Rempe group in [68]. Interestingly, because in this early experiment it was difficult to place more than one atom in the small cavity volume, the cavity mirror separation was increased to place multiple atoms inside. Even though this decreased the single atom-light coupling, the collective coupling was shown to be enhanced by the number of atoms. Theoretical studies on the different phenomena that can arise with many atom cavity QED was pioneered by the group of H. Ritsch [71, 72, 73]. Collective dynamics of atoms was also observed around the same time in ring cavity set ups in the group of A. Hemmerich [69, 70]. The most interesting effect discovered during this period was the self-organisation phenomenon, where a collection of atoms placed in a cavity are driven in the transverse direction by a laser standing wave potential. The cavity mode is excited by scattering light from the atom by a transverse laser. For transverse driving with low intensity the atomic cloud is homogeneously distributed in space but above a critical intensity [73, 75] the atoms spontaneously arrange themselves into a periodic pattern maximising the scattering of light into the cavity mode. This super-radiant phase transition was observed in the group of Vuletić in 2003 [74]. Closely related to the self-organisation transition is the idea of Collective Atomic Recoil Lasing (CARL) in a ring cavity. There, one of the two degenerate counterpropogating photonic modes of a ring cavity is

driven. In the presence of atoms in the cavity, this leads to a large spontaneous transfer of photons from the driven to the undriven light mode above a threshold [76, 77] accompanied by the formation of a regular spatial pattern of the atomic density.

In experiments on atomic cQED prior to 2007, the quantum degeneracy of the atoms did not play an important role in the dynamics. This changed with the experiments by the Esslinger group [79] where a BEC of Rubidium atoms was successfully placed inside an standing wave optical cavity. A single collective (momentum) excitation mode about the homogeneous BEC state couples strongly with the light field and provides a mapping of the dynamics onto a cavity optomechanical system [80]- a mechanical oscillator coupled to the cavity light field. The nonlinear oscillator-light interaction can lead to optical bistability with even less than a single photon in the cavity. This is remarkable since conventional dispersive optical bistability results from placing crystals with nonlinear polarizability inside cavities driven intensely with laser fields [81]. In more recent work from the Esslinger group the self-organisation transition was observed with a BEC [84, 85, 86] in a transversely pumped optical cavity (as opposed to a thermal ensemble of atoms in Vuletic's work [74]). The subsequent study of the excitation spectrum of the BEC near the self-organisation transition also revealed a mode softening indicative of the long-range interactions in the system [87].

In the Esslinger experiment the BEC was held in a trap along the directions transverse to the cavity axis and there was no additional trapping along the axial direction. In similar experiments performed at Berkeley in the group of D. M. Stamper-Kurn, cold atoms were trapped along the axis of a cavity with a deep external optical lattice (with a different wave number compared to the cavity mode). The atoms were localised at the nodes of the optical lattice and a single collective position co-ordinate provided a coherent quantum mechanical oscillator that interacts strongly with the cavity light field. The resulting nonlinear dynamics, including bistable response, was studied in [82]. An important difference between quantum and classical mechanics is the special role measurement plays in the former. In classical mechanics the act of measurement disturbs the system only in a quantitative manner that can in principle be removed by a refinement of the measuring device. Hence, there is no physical principle which sets limits to the accuracy with which a given physical parameter can be measured without disturbing the state of a classical system. This is not the case in quantum mechanics. The Heisenberg uncertainty principle [101] requires that a measurement that determines a system variable simultaneously causes the system to evolve to a state that makes the uncertainty in the conjugate variable larger. This principle was at the heart of the experiment presented in [83] from Berkeley, where the quantum measurement backaction due to the continuous measurement of the atomic collective position via the monitoring of cavity light transmission was quantified and measured. Quantum measurement backaction manifests itself via the force fluctuations induced by the "noisy" cavity [5] field on the atomic collective co-ordinate. The resulting broadening of the collective momentum leads to a heating of the atoms out of the trapping potential which is measured to

[5]The photon number fluctuations in the damped cavity can also be justified using the Fluctuation-Dissipation theorem

quantify the backaction. The experiments from the Esslinger group in Zurich and the Stamper-Kurn group in Berkeley have provided important inspiration for the subject matter in this thesis.

The experiments at Berkeley and Zurich have also generated a lot of interest amongst theory groups working on ultracold atoms in cavities in recent times. It is known [88] that the ground state of a dilute gas of ultracold atoms in an optical lattice is either an extended coherent superfluid (SF) state or a localized Mott-insulator (MI) state. The system chooses one of these states depending upon the depth of the optical lattice wells which controls the relative strength of the atomic repulsion in a given well to the tunnelling energy between the wells. The phase transition between the SF-MI states was experimentally observed in [89]. In [90], J. Larson and co-workers, considered the MI-SF transition when the standing wave potential inside an optical cavity plays the role of the optical lattice. Since the light field inside the optical cavity which sets the lattice depth is dependent on the atomic density distribution, this can lead to novel MI states in this system. A related work from the group of P. Meystre [91] demonstrated the possibility of certain parameter regimes where the cavity light field is bistable and the corresponding atomic configurations can be a Mott-insulator or superfluid. In another work from the Meystre group [92], a BEC placed inside a ring cavity with two degenerate travelling wave light modes is considered. Interestingly even when the two travelling modes are equally pumped, the strong atom-light interaction can lead to bistable steady states with unequal photon numbers in the two modes. In work from H. Pu's group multistable solutions [93] were shown to be possible at a few photon level for a two-component spinor BEC in an optical cavity. In a subsequent paper [94] the effects of measurement backaction corresponding to a homodyne measurement of the cavity light field carrying information about the atomic spin dynamics was analysed. In the paper [95], L. Zhou and co-workers consider a proposal for cavity induced switching between localized and extended atomic states (similar to [91]) in the experimental set up used in Berkeley. The rich non-equilibrium many body phenomena that can emerge from situations similar to the one considered in the self-organisation experiment from the Esslinger group [84] was the subject matter of [96, 97, 98, 99]. In the self-organisation experiment [84] the collective interaction between the atomic cloud and the cavity light field can be mapped on to the well known Dicke model describing a collection of two-level systems uniformly coupled to a single mode light field. In [96, 97] different dynamical phases that can occur in the non-equilibrium Dicke model realised in the experiment [84] were explored. In [98] BECs coupled to multimode cavities were examined and found to lead to interesting many body states with dislocations, frustration, glassiness and supersolidity. In a related work [99] a quantum spin glass phase was proposed for the Dicke model in a multimode optical cavity. The theory papers we have summarized in the above paragraph are a representative sample of the large and growing body of work in this topic. For a comprehensive overview of the current state of the art and future prospects in the exciting field of many atom cQED, the review article [100] can be consulted.

1.3 Thesis Outline

The main topic of this thesis is a theoretical study of Bloch oscillations of ultracold atoms confined within an optical cavity. This thesis will be a compilation of three publications that have been completed during my graduate studies. In the second chapter of the thesis we introduce the basic theoretical description for ultracold atoms interacting with a single mode light field inside an optical cavity.

When a cloud of cold atoms is placed in an optical cavity driven by a coherent laser field with frequency quasi resonant with, but still significantly detuned from, an atomic transition the atoms effectively feel a periodic potential along the cavity axis. The strength of the lattice potential is controlled by the number of photons within the cavity. From the point of view of the cavity, the atomic cloud acts like a dispersive medium changing the effective length and hence effectively detuning the cavity resonance mode further from the driving laser's frequency. The intracavity light intensity is not a static quantity but is self-consistently set by the strength of the coupling provided by the atomic density distribution and so becomes time-dependent if the atoms are undergoing dynamics. On the addition of a linear potential, the atomic cloud undergoes Bloch oscillations leading to a periodic change in the atom-light coupling. The intracavity light intensity varies periodically as a result and a measurement of the transmitted photon current provides a sensitive measurement of the Bloch frequency and hence the force. Remarkably, the Bloch frequency is unaffected by the backaction which provides a dynamical lattice depth whose periodicity is unchanged. Chapter 3 provides the publication concerned with this problem. The atoms are described by a single coherent quantum degenerate wavefunction (mean field theory) and the light field is given by a coherent classical field.

In Chapter 4, we change gears slightly and examine some interesting properties that arise from the nonlinearity inherent in the atom-cavity field interaction. When the frequencies relevant to atomic dynamics such as the strength of the average intracavity lattice depth and the atomic recoil energy are much less than the cavity relaxation time scale, the intracavity light field dynamics can be adiabatically eliminated. This leads to a non-local, nonlinear eigenvalue problem in a closed form for the atomic steady state wavefunction alone. We work out an energy functional that describes the problem and evaluate it using a Bloch ansatz. The resulting energies can be arranged into bands. For large enough collective coupling strengths, the band structure can develop interesting swallow tail loops as a function of quasimomentum analogous to behaviour seen for self-interacting BECs in optical lattices [102, 103]. For the light field these interesting atomic solutions translate to optical multistability, where, at a given value of system parameters, there is more than one steady state intracavity intensity possible.

Chapter 5 is devoted to the study of the effects of quantum noise on the Bloch oscillation dynamics discussed within mean field theory in Chapter 3. This is done by examining the time evolution of linearised fluctuations of the atomic and light fields. The photonic fluctuations in the cavity are driven

by the vacuum noise of the electromagnetic field and communicated to the atoms via the atom-light coupling. The correlated dynamics of the atom-light fluctuations about the *time-dependent* (due to the Bloch oscillations) meanfields are numerically solved. We also examine how the signal to noise ratio for the Bloch frequency measurement is affected by the inclusion of the fluctuations. The atomic depletion out of the meanfield can also be viewed as a manifestation of quantum measurement backaction [104, 105]. Chapter 6 discusses the conclusions of the thesis summarizing the different results presented. We set our work in the context of current research in cQED and indicate some directions which will be explored in future research.

Chapter 2

Ultracold atoms in a cavity - theoretical background

In this chapter we provide the basic theoretical description of ultracold atoms confined within an optical cavity. We begin by considering the dynamics of a single mode light field in a driven damped cavity. The following section considers the combined dynamics of a single two level atom moving along the axis of the cavity. The final section will extend the single atom scenario to a dilute cloud of cold atoms inside the cavity.

2.1 Single cavity mode damped by Markovian reservoir

For the purposes of this thesis, an optical cavity is an arrangement of two partially transmissive mirrors facing each other in space separated by a given distance L. When driven with an external source of electromagnetic waves, standing waves are set up in the space between the mirrors. Due to interference, waves with frequencies that are integer multiples of the fundamental (angular) frequency given by $\omega_c = \pi c/L$ are sustained within the resonator. The partial transmittivity of the mirrors ensures that the resonances have a finite linewidth denoted by 2κ. The ratio of the spacing between the resonances (the free spectral range) and the linewidth is called the finesse of the cavity and is given by $F = \frac{c\pi}{2\kappa L}$[1]. In this thesis we are interested in cavities with a high finesse, which have been realised [46] by the use of high quality mirrors (which lowers κ) and small cavity volumes (which lowers L). In such high finesse cavities, the resonances are well separated. This allows a theoretical description focusing on a single light mode (with frequency centered on ω_c) of the cavity modelled as a simple harmonic oscillator. In the quantised picture of such a mode [107], the effect of partially

[1]The finesse has both physical and practical significance. It is related to the mirror power reflectivity $\mathcal{R}$ by $F = \frac{\pi\sqrt{\mathcal{R}}}{1-\mathcal{R}}$ [46]. Physically the number of round trips made in the cavity by a single photon is related to the number of reflections, which is approximately given by F/π

transmissive mirrors that gives the finite linewidth is modelled through interaction of the single mode with a reservoir of harmonic oscillators. We will describe the properties and specific assumptions regarding the reservoir below but as of now it is sufficient to know that in general the reservoir has many degrees of freedom and the cavity mode's coupling does not significantly change the state of the reservoir. Hence we will aim to describe the effects of the reservoir on the dynamics of the system of interest i.e. the single mode field. As indicated, the eventual result will ignore the explicit consideration of reservoir dynamics, which is why this system is amongst the simplest examples of an open quantum system. In the rest of this section we follow [107] and derive the dynamical equations governing such an open quantum mode.

We begin by writing down the hamiltonian [107] for the single mode of interest (denoted $\hat{a}$) and the reservoir modes (denoted $\hat{b}_{\mathbf{k}}$):

$$H_c = \hbar\omega_c \hat{a}^\dagger \hat{a} + \sum_{\mathbf{k}} \hbar\omega_{\mathbf{k}} \hat{b}_{\mathbf{k}}^\dagger \hat{b}_{\mathbf{k}} + \hbar \sum_{\mathbf{k}} g_{\mathbf{k}} \left(\hat{b}_{\mathbf{k}}^\dagger \hat{a} + \hat{a}^\dagger \hat{b}_{\mathbf{k}} \right). \tag{2.1}$$

The first two terms are the free field terms for the cavity and reservoir modes respectively. The third term describes the coherent interaction between the cavity mode and the reservoir mode. The Heisenberg equations of motion for the operators are given by:

$$\dot{\hat{a}} = -i\omega \hat{a}(t) - i \sum_{\mathbf{k}} g_{\mathbf{k}} \hat{b}_{\mathbf{k}}(t) \tag{2.2}$$

$$\dot{\hat{b}}_{\mathbf{k}} = -i\omega_k \hat{b}_{\mathbf{k}}(t) - i g_{\mathbf{k}} \hat{a}(t). \tag{2.3}$$

Since we are interested in a closed form equation for the cavity mode, we formally integrate the reservoir equation of motion Eq. (2.3) as:

$$\hat{b}_{\mathbf{k}}(t) = \hat{b}_{\mathbf{k}}(0) e^{-i\omega_k t} - i g_{\mathbf{k}} \int_0^t dt' \hat{a}(t') e^{-i\omega_k (t-t')}$$

The first term here arises from the free evolution of the reservoir operators and the second term comes from the interaction with the cavity mode. We can substitute the above equation in Eq. (2.2) to remove $\hat{b}_{\mathbf{k}}(t)$ dependence:

$$\dot{\hat{a}} = -i\omega_c \hat{a} - \sum_{\mathbf{k}} g_{\mathbf{k}}^2 \int_0^t dt' \hat{a}(t') e^{-i\omega_k (t-t')} - i \sum_{\mathbf{k}} g_{\mathbf{k}} \hat{b}_{\mathbf{k}}(0) e^{-i\omega_k t}. \tag{2.4}$$

The second term on the right hand side leads to decay and the third term, which is independent of $\hat{a}(t)$, can be identified as a noise operator and is determined by the initial state of the reservoir. Due to the free field evolution the noise operator has all the reservoir mode frequencies in it and varies rapidly. We can pick out the frequencies that are most relevant to the cavity mode evolution

by transforming:

$$\tilde{\hat{a}}(t) = \hat{a}(t)e^{i\omega_c t} \tag{2.5}$$

and Eq. (2.4) reduces to:

$$\dot{\tilde{\hat{a}}} = -\sum_{\mathbf{k}} g_{\mathbf{k}}^2 \int_0^t dt^{'} \tilde{\hat{a}}(t')e^{-i(\omega_k-\omega_c)(t-t')} + \tilde{\hat{F}}(t) \tag{2.6}$$

$$\tilde{\hat{F}}(t) = -i\sum_{\mathbf{k}} g_{\mathbf{k}}\hat{b}_{\mathbf{k}}(0)e^{-i(\omega_k-\omega_c)t} \tag{2.7}$$

We focus now on the first term on the right hand side of Eq. (2.6) and rewrite the sum over reservoir modes ($\mathbf{k}$) as follows:

$$\sum_{\mathbf{k}} g_{\mathbf{k}}^2 e^{-i(\omega_k-\omega_c)(t-t')} = \int_0^\infty \frac{d\omega}{2\pi}\kappa(\omega)e^{-i(\omega-\omega_c)(t-t')} \tag{2.8}$$

$$\kappa(\omega) = 2\pi\sum_{\mathbf{k}} g_{\mathbf{k}}^2\delta(\omega-\omega_k) \tag{2.9}$$

We have simply rewritten the system-reservoir coupling in frequency space. To proceed further we assume the frequency dependence of the coupling is flat i.e. $\kappa(\omega) \equiv \kappa$. This is known as the Markov approximation [108]. The physical content of this approximation can be found by taking the time integral in Eq. (2.6) into consideration. This time integral is appreciable only for $\omega_k \sim \omega_c$ and hence we mostly require that the frequency dependence of the coupling is flat near ω_c. This essentially means that at the time scales relevant to the system dynamics the reservoir responds to the system as though it had no intrinsic time scale i.e. instantaneously. Having made this approximation, we can simplify Eq. (2.8) as:

$$\sum_{\mathbf{k}} g_{\mathbf{k}}^2 e^{-i(\omega_k-\omega_c)(t-t')} = \kappa\delta(t-t').$$

This leads to the following equation of motion:

$$\dot{\tilde{\hat{a}}} = -\kappa\tilde{\hat{a}}(t) + \hat{F}(t). \tag{2.10}$$

At this stage it may seem as though we have achieved our objective of getting a closed equation for the system operators, but unless we can specify the correlation properties of the noise operator $\hat{F}(t)$, we will not be able to use Eq. (2.10) in an actual calculation. Before we calculate we note that one can already see the importance of the noise term for preservation of commutation relations of $\tilde{\hat{a}}(t)$.

Without the noise term, $\tilde{\hat{a}}(t) = \tilde{\hat{a}}(0)e^{-\kappa t}$ and as a result:

$$\left[\tilde{\hat{a}}(t), \tilde{\hat{a}}^\dagger(t)\right] = e^{-2\kappa t}.$$

The Markovian approximation in conjunction with the commutator relations for $\hat{b}_{\mathbf{k}}(0)$, can be used to show that the commutator of the noise operators provides a contribution that is $1-e^{-2\kappa t}$, precisely cancelling the decay of the field commutator.

We assume the reservoir is at thermal equilibrium which leads to the following identities for the expectation values of the initial time reservoir operators:

$$\langle \hat{b}_{\mathbf{k}}(0)\rangle = \langle \hat{b}^\dagger_{\mathbf{k}}\rangle = 0 \tag{2.11}$$

$$\langle \hat{b}^\dagger_{\mathbf{k}}(0)\hat{b}_{\mathbf{k}'}(0)\rangle = \delta_{\mathbf{k},\mathbf{k}'}\bar{n}_{\mathbf{k}} \tag{2.12}$$

$$\langle \hat{b}_{\mathbf{k}}(0)\hat{b}^\dagger_{\mathbf{k}'}(0)\rangle = \delta_{\mathbf{k},\mathbf{k}'}(\bar{n}_{\mathbf{k}}+1) \tag{2.13}$$

$$\langle \hat{b}_{\mathbf{k}}(0)\hat{b}_{\mathbf{k}'}(0)\rangle = \langle \hat{b}^\dagger_{\mathbf{k}}(0)\hat{b}^\dagger_{\mathbf{k}'}(0)\rangle = 0 \tag{2.14}$$

From Eq. (2.11), it is simple to see that $\langle \hat{F}(t)\rangle = \langle \hat{F}^\dagger(t)\rangle = 0$. We can then use the Markov approximation and Eq. (2.12) − Eq. (2.14) to show that:

$$\langle \hat{F}^\dagger(t)\hat{F}(t')\rangle = 2\kappa\bar{n}_{th}(\omega_c)\delta(t-t') \tag{2.15}$$

$$\langle \hat{F}(t)\hat{F}^\dagger(t')\rangle = 2\kappa(\bar{n}_{th}(\omega_c)+1)\delta(t-t') \tag{2.16}$$

These are the only non-zero correlations of the noise operator. Knowing the above we can calculate system operator correlations and also the correlations between the noise operator and the system operators at later times. Finally, throughout this thesis we will be interested in situations where the reservoir is approximately at $T = 0$, as a result of which the correlation Eq. (2.15) vanishes. Thus the dynamical equation for a cavity mode in contact with a zero temperature reservoir (i.e. an example of a Heisenberg-Langevin equation) is given by:

$$\dot{\hat{a}}(t) = -i\omega_c\hat{a}(t) - \kappa\hat{a}(t) + \sqrt{2\kappa}\hat{\xi}(t) \tag{2.17}$$

where the only non-zero correlation of the rescaled noise operator (referred to henceforth as the Langevin operator) is:

$$\langle \hat{\xi}(t)\hat{\xi}(t')\rangle = \delta(t-t^{'}), \tag{2.18}$$

$$\hat{\xi}(t) = -\frac{i}{\sqrt{2\kappa}}\sum_{\mathbf{k}} g_{\mathbf{k}}\hat{b}_{\mathbf{k}}(0)e^{-i\omega_k t}. \tag{2.19}$$

From the above equation it is clear that in the long time limit the field $\hat{a}$(t) will have the same correlation properties as the Langevin noise operator $\hat{\xi}(t)$. The presence of atoms in the cavity

changes this picture and the light field correlations are not just set by the Langevin noise but also depend on the atomic degrees of freedom. This is taken into account in the treatment of quantum noise presented in Chapter 5.

In the next section we consider a single atom moving within a cavity that is driven by a coherent laser source and establish the equations that describe its dynamics.

2.2 Single two-level atom in a cavity

Let us now consider a single two level atom moving inside an optical cavity that is pumped by a coherent laser source. Our treatment will closely follow the work in [64]. The hamiltonian for such a system is given by:

$$H_{\rm b} = \frac{\hat{p}^2}{2m} + \hbar\omega_a \left|2\right\rangle\left\langle 2\right| + \hbar\omega_c \hat{a}^\dagger \hat{a} - i\hbar g(\mathbf{r})\left(\left|2\right\rangle\left\langle 1\right| \hat{a} - \left|1\right\rangle\left\langle 2\right| \hat{a}^\dagger\right) - i\hbar\eta(\hat{a}e^{i\omega_p t} - \hat{a}^\dagger e^{-i\omega_p t}). \quad (2.20)$$

Here the excited (ground) internal levels of the atomic electron are denoted by $|2\rangle$ ($|1\rangle$) and the separation between the two relevant atomic levels is given by ω_a. The cavity resonance frequency is denoted by ω_c. The atom-single mode interaction [fourth term in Eq. (2.20)] is written in the Jaynes-Cummings form [109], within the dipole and rotating wave approximations. The rate of cavity pumping is given by η and ω_p denotes the frequency of the pumping laser. The dipole coupling $g(\mathbf{r})$ depends on the atomic center of mass position $\mathbf{r}$ within the cavity mode and is given by:

$$\begin{aligned} g(\mathbf{r}) &= g_0 f(\mathbf{r}) = d\sqrt{\frac{\hbar\omega_c}{\epsilon_0 V}} f(\mathbf{r}) \\ d &= \left\langle 2\right| e\mathbf{x}.\hat{\epsilon} \left|1\right\rangle \end{aligned} \quad (2.21)$$

with the electron position operator $\mathbf{x}$, field polarization $\hat{\epsilon}$, cavity mode volume V and mode function $f(\mathbf{r})$. We will henceforth use a pseudo spin-1/2 notation for the two level atom, with $\hat{\sigma}_z = \left(\left|2\right\rangle\left\langle 2\right| - \left|1\right\rangle\left\langle 1\right|\right)/2, \hat{\sigma} = \left|1\right\rangle\left\langle 2\right|$. The optical frequencies occurring in Eq. (2.20) are large and in general can be tuned. Thus it is advantageous to work in a frame where only the relative frequencies are important. To that we apply the following unitary rotation with respect to the pump frequency:

$$U_f(t) = \exp(-i\omega_p \hat{a}^\dagger \hat{a}) \exp(-i\omega_p \hat{\sigma}^\dagger \hat{\sigma})$$

and upon using the transformation rule:

$$H_{\rm sp} \rightarrow U_f^\dagger H_{\rm b} U_f + i\hbar \dot{U^\dagger}_f U_f,$$

we obtain the transformed hamiltonian:

$$H_{\rm sp} = \frac{\hat{p}^2}{2m} - \hbar\Delta_a\hat{\sigma}_z - \hbar\Delta_c\hat{a}^\dagger\hat{a} - i\hbar g(\mathbf{r})\left(\hat{\sigma}^\dagger\hat{a} - \hat{\sigma}\hat{a}^\dagger\right) - i\hbar\eta(\hat{a} - \hat{a}^\dagger), \tag{2.22}$$

with the pump-atom detuning $\Delta_a = \omega_p - \omega_a$ and the pump-cavity detuning $\Delta_c = \omega_p - \omega_a$. With this we can write down the coupled Heisenberg-Langevin equations for the atom and the cavity light field operators [110]:

$$\dot{\hat{a}} = (i\Delta_c - \kappa)\,\hat{a}(t) + g(\mathbf{r})\hat{\sigma} + \eta + \hat{\xi}(t) \tag{2.23}$$

$$\dot{\hat{\sigma}} = (i\Delta_a - \gamma)\hat{\sigma} + 2g(\mathbf{r})\hat{\sigma}_z\hat{a} + \hat{\zeta}(t) \tag{2.24}$$

$$\dot{\hat{\sigma}}_z = -g(\mathbf{r})\left(\hat{\sigma}^\dagger\hat{a} + \hat{a}^\dagger\hat{\sigma}\right) - \gamma(\hat{\sigma}_z + 1/2) + \hat{\zeta}_z(t) \tag{2.25}$$

where we use $\hat{\xi}(t)$ to denote the Langevin operators arising from the open nature of the cavity mode [see Eq. (2.17)]. The operators $\hat{\zeta}$ and $\hat{\zeta}_z$ denote the Langevin operators that arise from the interaction of the atom with the reservoir of vacuum electromagnetic modes. The dissipation process corresponding to this is nothing but spontaneous emission at the rate γ [2]. As mentioned in Chapter 1, the coupled dynamics of the atomic internal levels and the cavity light field is interesting in its own right and has been examined in great detail by many researchers [4].

In this thesis we are interested in the regime where the internal levels of the atom play only a minor role. Specifically this is the situation when the atom-pump laser detuning Δ_a is very large. There are two key simplifications to the above dynamics as a result. Firstly, the atomic population remains confined mainly to the ground state and the two level dynamics is in the so called low saturation limit. This means we can simply replace the population difference operator by its expectation value in the ground atomic state i.e. $\hat{\sigma}_z \to \langle\hat{\sigma}_z\rangle = -1/2$. Within this approximation the dynamics of $\hat{\sigma}_z$ is completely neglected [including the noise in Eq. (2.25)]. Since the replacement implies the commutator $\left[\hat{\sigma}, \hat{\sigma}^\dagger\right] = -2\hat{\sigma}_z = 1$, this approximation has been called the bosonization of the atomic dipole [64, 111]. Moreover this leads to the factorization of the atomic internal state and light field ($\hat{\sigma}_z\hat{a} \to -\hat{a}/2$) linearising Eq. (2.24).

The second modification comes about by adiabatically slaving the atomic *internal* level dynamics to the light field dynamics. This is again justified when the detuning Δ_a is much greater in magnitude than other relevant frequencies such as $g_0\langle\hat{a}\rangle$, γ and atomic centre of mass energies which are of the order of the recoil frequency $\omega_R = \frac{\hbar k_p^2}{2m}$ [64, 111]. This modification can be implemented by setting

[2] This can be derived [110] in a manner similar to Sec. 2.1 by replacing the harmonic oscillator mode with a two level system. Also, the Purcell enhancement [46] of atomic spontaneous emission into the cavity mode is not important in our situation since typically the frequency of the driving field is far detuned from the atomic level separation.

the time derivative $\dot{\hat{\sigma}} = 0$ in Eq. (2.24) leading to:

$$\hat{\sigma} \approx \frac{1}{g_0}\left(-iU_0 + \Gamma_0\right) f(\mathbf{r})\hat{a} \tag{2.26}$$

$$U_0 = \frac{g_0^2 \Delta_a}{\Delta_a^2 + \gamma^2},\ \Gamma_0 = \frac{g_0^2 \gamma}{\Delta_a^2 + \gamma^2}. \tag{2.27}$$

The parameters U_0 and Γ_0 can also be viewed as the real and complex parts respectively of the susceptibility of the atom to the cavity light field. They simply describe the linear relation between the atomic polarization and applied field. The ratio of the complex to real part scales as $\Gamma_0/U_0 = \gamma/\Delta_a$. In the dispersive limit of the atom-light interaction the spontaneous emission frequency is much less than the detuning Δ_a. This will be the regime of choice for our considerations. As a result we completely neglect spontaneous emission in our calculations and set $U_0 = g_0^2/\Delta_a$. We note that this regime is readily experimentally accessible and is also used in the context of atom trapping in the FORT schemes [112] (Far Off-Resonance Trap). Substituting the adiabatically eliminated form Eq. (2.26) in Eq. (2.23) we find in the dispersive limit:

$$\dot{\hat{a}} = \left(i\Delta_c - \kappa\right)\hat{a}(t) - iU_0 f(\mathbf{r})^2 \hat{a} + \eta + \hat{\xi}(t). \tag{2.28}$$

Thus, in the dispersive limit, the single atom-cavity hamiltonian Eq. (2.22) can be replaced by the effective hamiltonian:

$$H_{\mathrm{sp}}^{\mathrm{eff}} = \frac{\hat{p}^2}{2m} - \hbar\Delta_c \hat{a}^\dagger \hat{a} + \hbar U_0 f(\mathbf{r})^2 \hat{a}^\dagger \hat{a} - i\hbar\eta(\hat{a} - \hat{a}^\dagger) \tag{2.29}$$

Usually, the mode function $f(\mathbf{r})$ in a Fabry-Perot cavity has a periodic standing wave profile along the axis with a gaussian envelope in the transverse directions. Thus, in the dispersive limit the light field in the cavity provides a periodic potential for the atomic center of mass dynamics [third term in Eq. (2.29)]. In the next section we will present the second quantised version of the above hamiltonian which is necessary for the description of a cloud of cold atoms confined in an optical cavity.

2.3 Many cold atoms in a cavity

The hamiltonian Eq. (2.29) serves as the starting point to consider the center of mass dynamics of moving atoms inside an optical resonator in the dispersive regime. A range of theoretical and experimental research has taken place in this regime over the last two decades and is summarized in [100]. Some highlights include the phenomenon of cavity cooling, where the damping of the center of mass motion of the atom is due to the finite response time (set by κ^{-1}) of the cavity light fields as they adapt to the change in the atomic configuration (theory in [61] and experimentally verified in [65]). When a collection of classical atoms, say in a thermal state, are confined in a cavity the collective interaction with the light field can again manifest itself in spatial self-organisation of the

atoms. This was theoretically studied in [73],[75] and experiments are described in [74]. Although there is a wealth of physics that can be studied even while treating the atoms as classical particles, the problems taken up in this thesis are all set in a regime where the cloud of bosonic atoms in the cavity is cold enough that the quantum degeneracy is important. This is interesting for a variety of reasons, chief amongst which (for our interests) it allows for situations where genuine quantum phenomena of particles in a periodic potential such as Bloch oscillations can be included. A simple first approach in such problems, as described in [78], is to assume all the atoms in a cloud occupy the same single particle state. In other words, we consider a dilute Bose-Einstein condensate of atoms in a cavity [79]. Experimentally, such regimes have become accessible in the last few years. In [82] the collective heating due to the cavity photon number fluctuations of a cloud of (non-BEC) bosonic atoms was experimentally measured. In [79] a BEC of Rubidium atoms was confined inside a cavity and the interesting phenomena of optical bistability in the transmission spectrum of light through the cavity containing a BEC was experimentally studied. In the many atom works described in this section so far, the contact interactions between atoms due to collisions is accounted for when comparing quantitatively to experiments. But, the novelty and to a large extent, the qualitative behaviour, lies in the correlated dynamics of the atoms and the light field. Thus, in our theoretical investigations we will ignore direct atom-atom interactions completely. Moreover these contact interactions can be tuned experimentally using Feshbach resonances as well. In Chapter 5, we make this consideration quantitative and show that for experimentally relevant parameter regimes our approximation is justified.

We can now write down the basic many-atom hamiltonian that will serve as the starting point for all our discussions in the different works presented in the rest of this thesis. This is an extension of the single particle hamiltonian Eq. (2.29) to describe a collection of bosonic atoms. Moreover, we also include an external potential for the atoms which will account for the force that causes Bloch oscillations [3]. We will also specialise to considering dynamics in 1-dimension along the axis of the cavity. The transverse profile of the atomic cloud is assumed to not vary significantly during the axial dynamics. Correspondingly the dispersive shift U_0 will now be assumed to have been scaled by factors that depend on the overlap of the atomic cloud with the transverse cavity mode profile. Denoting the bosonic field annihilation operator for the atoms as $\hat{\Psi}(x,t)$ we have:

$$H_{\rm mb} = \int dx \hat{\Psi}^\dagger(x,t) \left(\frac{\hat{p}_x^2}{2m} + \hbar U_0 \hat{a}^\dagger \hat{a} \cos^2(k_p x) + V_{\rm ext} \right) \hat{\Psi}(x,t) - \hbar \Delta_c \hat{a}^\dagger \hat{a} - i\hbar\eta(\hat{a} - \hat{a}^\dagger).. \qquad (2.30)$$

[3] In experiments from the Esslinger group [79] an additional external harmonic trapping potential was used to confine the atoms in a cavity but we envisage our theoretical problems without this trap. This is not too restrictive since in many current Bloch oscillation experiments all external potentials except for the periodic lattice are switched off during the experiment.

Chapter 3

Atomic Bloch-Zener oscillations for sensitive force measurements in a cavity

Preface

When a particle in a periodic potential is subject to a constant force, it undergoes Bloch oscillations. This phenomenon was originally predicted for electrons in a metal accelerated by an electric field [26, 25]. Due to the presence of defects and impurities the relaxation time scale for electronic motion is typically much shorter than the Bloch period. Consequently, long-lived Bloch oscillations have been hard to observe in solid state systems. In the work presented in this chapter we propose a scheme for the measurement of the Bloch frequency of ultracold atoms moving in the standing wave potential inside an optical cavity which is oriented vertically, i.e., the local acceleration due to gravity provides the force. As the atoms execute Bloch oscillations the intensity and phase of the cavity light field is modulated at the Bloch frequency due to the strong backaction of the atoms on the light field. The light transmitted through the cavity can be measured to extract the Bloch frequency. This provides a continuous, non-destructive measurement method compared to the usual techniques used in earlier experiments on Bloch oscillations of cold atoms in optical lattices (see Chapter 1). In the present work the atoms are assumed to be cold enough to be described by a single coherent wavefunction and the light field is assumed to be in a coherent state. The ground work for this chapter was done during my masters [40] and completed during my doctoral research period. [1]

[1] Note we have used the term 'Bloch-Zener oscillation' in the paper reproduced below to refer to Bloch oscillations. We used this term since the first paper making explicit reference to the phenomenon of Bloch oscillations was authored by Clarence Zener [25]. We have discontinued this usage in the rest of this thesis to avoid confusion with current literature where inter-band oscillations of the atomic probability density are known as Bloch-Zener oscillations [41].

Abstract

Cold atoms in an optical lattice execute Bloch-Zener oscillations when they are accelerated. We have performed a theoretical investigation into the case when the optical lattice is the intra-cavity field of a driven Fabry-Perot resonator. When the atoms oscillate inside the resonator, we find that their back-action modulates the phase and intensity of the light transmitted through the cavity. We solve the coupled atom-light equations self-consistently and show that, remarkably, the Bloch period is unaffected by this back-action. The transmitted light provides a way to observe the oscillation continuously, allowing high precision measurements to be made with a small cloud of atoms.

When quantum particles in a potential lattice are subjected to a constant force F, they execute Bloch-Zener oscillations (BZOs) [1] with a frequency

$$\omega_{\mathrm{B}} = Fd/\hbar\,, \tag{3.1}$$

where d is the period of the lattice. This behavior was first demonstrated [2] with electrons in semiconductor superlattices, where a DC electric field provided the force. However, rapid dephasing due to impurities [3] has prevented BZOs from becoming useful in solid state devices.

Cold atoms in optical lattices have recently provided an alternative realization of BZOs [5, 6, 7, 8, 9, 4, 10] in which long coherence times are possible. Initially, acceleration of the lattice induced the oscillations, but in subsequent experiments [7, 9, 10], gravity provided the required force. In [10], the BZO damping time was 12s, allowing some 4000 cycles to be measured over 7s. With such long coherence times, cold atom BZOs become suitable for high precision measurements, for example to determine the fine structure constant α [4], to measure gravity [10], or to explore Casimir-Polder forces [11]. In the experiments to date, it has been necessary to reconstruct the oscillations by making destructive measurements at a large number of different times, each measurement requiring a new cloud of atoms to be trapped, cooled, and loaded into the lattice. The process is laborious and suffers from shot-to-shot variations in the initial cloud conditions. In this paper, we discuss how the measurement could be substantially improved by using an optical cavity to enhance the interaction of the atoms with the light. We show how the light transmitted through the cavity can provide an *in vivo* observation of the BZOs and we assess the extent to which this perturbs the motion of the atoms. Finally we consider the statistical sensitivity of the method and show that it can yield high precision in a single shot.

Let us take the cavity to be a vertical Fabry-Perot resonator illuminated by a laser, which makes a standing-wave light field inside, shown in Fig. 3.1(a). Cold atoms in this lattice execute BZOs under the influence of gravity, as illustrated in Fig. 3.1(b). The optical dipole interaction between one cavity photon and an atom placed at an antinode of the field is given by $\hbar g_0 = \mu\sqrt{\hbar\omega_{\mathrm{c}}/(\epsilon_0 V)}$, where ω_c and V are the frequency and volume of the relevant cavity mode and μ is the atomic transition dipole moment. The effect of one atom on the cavity field is characterised by the cooperativity $C = g_0^2/(2\kappa\gamma)$, where 2γ is the atomic spontaneous emission rate in free space and 2κ is the cavity energy damping rate. When $C \gtrsim 1$, the cavity field is strongly perturbed by the atom, as illustrated in Fig. 3.1(c). Thus the light transmitted or reflected by such a cavity can detect the presence of a single atom [12], and can be sensitive to the motion of atoms trapped within the cavity [13], as in Fig. 3.1(d). Although we shall not discuss Bose-Einstein condensates (BECs) in this paper, we note in passing that several experiments have succeeded in placing BECs inside optical cavities [14].

Consider a cavity mode, whose frequency in the absence of any atoms is ω_c, pumped by an external laser of the same frequency. A cloud of N atoms, each of mass m, is placed inside the cavity and is sufficiently dilute that the atoms do not interact directly with each other. The coupled

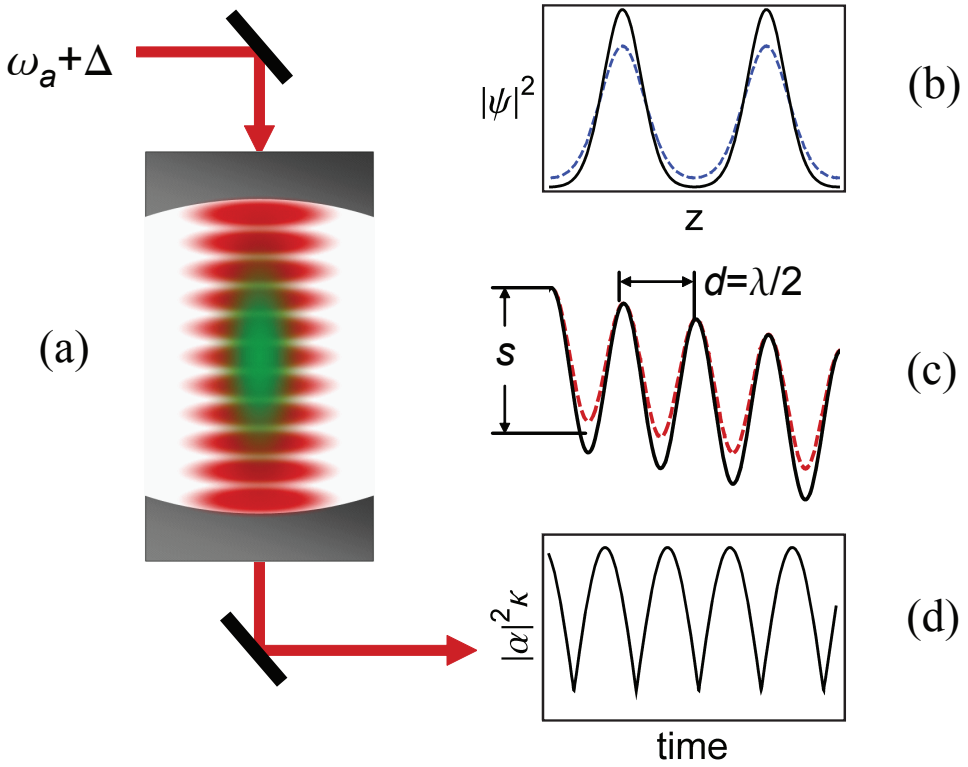

Figure 3.1. Schematic of the proposed experiment. (a) A cloud of cold atoms is held in a standing-wave optical trap inside a vertical Fabry-Perot cavity. (b) The atoms execute Bloch-Zener oscillations, leading to a periodic modification of their wave function. (c) This modulates the intra-cavity power and hence the lattice depth s. (d) The power modulation is seen in the light transmitted by the cavity.

atom-cavity hamiltonian becomes [15]

$$\hat{H} = \frac{\hbar^2}{2m}\int |\nabla_z \hat{\psi}|^2 \mathrm{d}z + \frac{\hbar g_0^2}{\Delta}\hat{a}^\dagger \hat{a}\int \hat{\psi}^\dagger\hat{\psi}\,\cos^2(k_\mathrm{c} z)\mathrm{d}z + F\int \hat{\psi}^\dagger\hat{\psi}\,z\;\mathrm{d}z - \mathrm{i}\hbar(\eta^*\hat{a} - \eta\hat{a}^\dagger) \tag{3.2}$$

where the operator $\hat{a}(t)$ annihilates a photon in the cavity mode and the operator $\hat{\psi}(z,t)$ annihilates an atom at the point z. The first term gives the kinetic energy of the atom. The second describes the quadratic Stark interaction in the rotating-wave approximation. Here, $\Delta = \omega_\mathrm{c} - \omega_a$ is the detuning between the cavity mode and the atomic transition frequency ω_a, and $k_c = \omega_c/c$. This is an approximate form, that is valid when $\Delta \gg \gamma$ and $\eta^2 \ll (\kappa\Delta/g_0)^2$. Under these conditions the atom has negligible population in the excited state. The third term accounts for the external force, and the last term describes the coherent excitation of the cavity by the external laser. For a cavity with equal mirror reflectivities, the pumping rate is $\eta = \sqrt{\kappa I}$, where I is the rate of incident photons matching the cavity mode. The cavity field is a driven and damped quantum harmonic oscillator for which it is known that exact solutions of the Fokker-Planck equation are coherent states [16]. Furthermore, since there is negligible spontaneous emission by the atoms, the cavity field remains in a coherent state in the presence of atoms. Taking the expectation value of the Heisenberg equations of motion for $\hat{a}$ and $\hat{\psi}$ in the coherent state $|\alpha\rangle$ yields the equations of motion [17]:

$$\dot{\alpha} = -\mathrm{i}\frac{\alpha N g_0^2}{\Delta}\int |\Psi|^2\cos^2(k_\mathrm{c} z)\mathrm{d}z + \eta - \kappa\alpha\,, \tag{3.3}$$

$$\mathrm{i}\hbar\dot{\Psi} = \left(\frac{-\hbar^2}{2m}\partial_z^2 + \frac{\hbar g_0^2|\alpha|^2}{\Delta}\cos^2(k_\mathrm{c} z) + Fz\right)\Psi \tag{3.4}$$

where $\Psi(z,t) = \langle\Psi_{N-1}|\hat{\psi}(z,t)|\Psi_N\rangle/\sqrt{N}$ is the wave function occupied by all N atoms and $|\Psi_N\rangle$ is the corresponding state vector in Fock space. We have added a damping term proportional to κ in Eq. (3.3) to account for leakage of light through the mirrors [18]. These equations neglect quantum fluctuations of the light field which can heat the atoms: we return to this effect later. Equations (3.3) and (3.4) must be solved self-consistently: the coupling

$$g^2(t) = g_0^2\int |\Psi(z,t)|^2\cos^2(k_\mathrm{c} z)\mathrm{d}z \tag{3.5}$$

changes α, which changes the depth of the lattice. This alters the atomic wave function and therefore changes g, etc. In static equilibrium, $\dot{\alpha} = 0$ and then

$$\alpha = \frac{\eta}{\kappa}\;\frac{1}{1 + \mathrm{i}Ng^2(t)/(\kappa\Delta)}. \tag{3.6}$$

Even if the atoms are in motion, (3.6) remains a very good approximation since κ is generally much greater than the highest frequency in the atom dynamics, so that the field 'instantaneously' adapts

to the atomic distribution. Frequencies that feature in the atomic motion are the BZO frequency, the band splitting, and the harmonic frequency $\omega_{\rm ho} = 2g_0|\alpha|\sqrt{E_{\rm R}/(\hbar\Delta)}$ at the bottom of each potential well, $E_{\rm R} = \hbar^2 k_{\rm c}^2/(2m)$ being the atomic recoil energy. For the experiments we consider here $\omega_{\rm B}$ and $\omega_{\rm ho}$ are much smaller than κ, so we assume in our analytic calculations, though not in our numerical simulations, that Eq. (3.6) holds.

Let us recall the standard theory of BZOs without a cavity [19, 21, 22, 23, 20, 24, 25]. The Schrödinger Eq. (3.4) can be written as $\mathrm{i}\hbar\dot{\Psi} = (\hat{H}_0 + Fz)\Psi$, where $\hat{H}_0 = \hat{p}^2/(2m) + s\cos^2 k_{\rm c} z$. The eigenfunctions $\chi_{q,s,n}(z)$ of $\hat{H}_0$ are Mathieu functions (Bloch waves) that in general depend on position z, lattice depth s, band index n and quasimomentum q, restricted to the first Brillouin zone $-\pi/d \leq q \leq \pi/d$ [26]. We assume in our analytic calculations that the atoms are in the lowest band, whose energy is $E_{q,s}$, and dispense with the band index so that $\hat{H}_0\chi_{q,s} = E_{q,s}\chi_{q,s}$. The Bloch theorem allows us to write $\chi_{q,s}(z) = U_{q,s}(z)\exp[\mathrm{i}qz]$, where $U_{q,s}(z) = U_{q,s}(z+d)$ obeys

$$\frac{(\hat{p}+\hbar q)^2}{2m}U_{q,s}(z) + s\cos^2(k_{\rm c}z)U_{q,s}(z) = E_{q,s}U_{q,s}(z). \tag{3.7}$$

To tackle the full hamiltonian $\hat{H}_0 + Fz$ we make the gauge transformation $\Psi(z,t) = \exp[-\mathrm{i}Ftz/\hbar]\tilde{\Psi}(z,t)$, yielding the Schrödinger equation $\mathrm{i}\hbar\dot{\tilde{\Psi}} = \tilde{\hat{H}}\tilde{\Psi}$, where $\tilde{\hat{H}} = (\hat{p} - Ft)^2/(2m) + s\cos^2 k_{\rm c} z$. Comparing this with (3.7) we see that the effect of the force is to evolve the quasi-momentum according to Bloch's acceleration theorem [1]

$$q \to q(t) = q_0 - Ft/\hbar\,, \tag{3.8}$$

where q_0 is the quasimomentum at $t = 0$. When $q(t)$ reaches the edge of the Brillouin zone at $-\pi/d$ it is mapped to the identical point $q = +\pi/d$, giving rise to oscillatory behaviour - the BZO. The corresponding Bloch wave has the approximate form [27] (setting $q_0 = 0$)

$$\tilde{\Psi}(z,t) \approx U_{q(t),s}(z)\exp[-\mathrm{i}/\hbar\int^t \mathrm{d}t'\ E_{q(t'),s}]\,, \tag{3.9}$$

within the adiabatic approximation that the rate of change $\dot{U}/U$ is too small to excite higher bands. Here $U_{q(t),s}(z)$ is the instantaneous solution of Eq. (3.7). During a BZO the spatial distribution $U_{q(t),s}(z)$ oscillates with a breathing motion, as shown schematically in Fig. 1(b).

Consider now the effect of the BZOs on the field inside the cavity. The coupling g (Eq. (3.5)) depends on $|\Psi(z,t)|^2$ which equals $|\tilde{\Psi}(z,t)|^2$. Its breathing motion changes g, which in turn modulates the cavity field through Eq. (3.6). Inserting (3.6) into (3.4), and replacing η by $\sqrt{\kappa I}$, we obtain the Schrödinger equation for atoms in a periodic potential $\mathrm{i}\hbar\dot{\Psi} = (\hat{p}^2/2m + s(t)\cos^2(k_{\rm c}z) + Fz)\Psi$, with the time-dependent potential depth

$$s(t) = \hbar I\left(\frac{g_0^2}{\Delta\kappa}\right)\frac{1}{1+\left(Ng^2(t)/(\Delta\kappa)\right)^2}. \tag{3.10}$$

When $Ng_0^2/(\kappa\Delta) \ll 1$, s is approximately constant in time and α becomes $(\eta/\kappa)[1-iNg(t)^2/(\Delta\kappa)]$, i.e. the light exhibits a small phase modulation and has negligible intensity variation. In this case, the atoms oscillate in a lattice that is essentially static. With stronger coupling, where $Ng_0^2/(\kappa\Delta) \simeq 1$, $s(t)$ is changed significantly during an oscillation. The fundamental period is nevertheless unchanged and is still given by Eq. (3.1). Physically, this is because BZOs arise from an interference of waves in a lattice akin to Bragg scattering and lattice depth plays no role in determining the phase-matching condition. Rather, this is determined by the symmetry of the hamiltonian which is precisely maintained at all times. To examine the effect of lattice depth modulation in more detail, let us begin with the adiabatic case where the frequency spectrum of $s(t)$ remains largely at low frequencies unable to excite higher Bloch bands. An example is shown in Fig. 3.2(a). In that case, the lowest band energy $E_{q,s(t)}$ is still determined by the instantaneous value of $s(t)$, with $H_0(t)\chi_{q,s(t)} = E_{q,s(t)}\chi_{q,s(t)}$, and q_0 remains a constant of the motion generated by $H_0(t)$ despite the time-dependent potential ([19] reaches a similar conclusion for electrons in an ac field). Consequently, the Bloch wave in the presence of an external force can still be calculated using Eq. (3.9), provided we use the instantaneous values of $s(t)$ and $s(t')$. It only remains to find the self-consistent solution for $s(t)$ by solving Eq. (3.10) at each instant of time. Here $s(t)$ appears explicitly on the left and also implicitly on the right as a parameter determining the Bloch wave function that is required to calculate the coupling $\sqrt{N}g(t)$ using Eq. (3.5). We conclude that despite the lattice depth modulation, the Bloch acceleration theorem (3.8) still holds for atoms in the lowest band and therefore the fundamental oscillation frequency remains identical to the $\omega_{\rm B}$ of an atom in a static lattice. Furthermore, because $\omega_{\rm B}$ is the same for all bands, there is no frequency shift even when higher bands are excited, as we have verified numerically for a wide range of $Ng_0^2/(\Delta\kappa)$.

Fig. 3.2(a) compares the lattice depths obtained by numerical solution of Eqs. (3.3) and (3.4) (lines) and by the adiabatic approximation of Eqs. (3.9) and (3.10) (dots). The two are in good agreement. Figure 3.2(b), shows a case of stronger coupling, where one can see fast oscillations superimposed on the main motion. The Fourier transform of this reveals two effects, illustrated in Fig. 3.2(c). (i) There are higher harmonics of $\omega_{\rm B}$ because the oscillations at the Bloch periodicity are not exactly sinusoidal. In the adiabatic solution, the first four are accurately reproduced and the higher harmonics are very small. (ii) The exact solution of Eqs. (3.3) and (3.4) predicts non-adiabatic components at higher frequencies, shown inset in Fig. 3.2(c). These are predominantly harmonics of $\omega_{\rm B}$ (the sharp lines), but in addition, there are other frequency components that can be seen as broad lines. These are only found in the full numerical solution and are due to a small amount of excitation to higher Bloch bands. These non-adiabatic effects become stronger as the parameter $Ng_0^2/(\kappa\Delta)$ is increased.

The atoms are driven not only by the mean-field potential $s(t)\cos^2(k_c z)$, but also by random forces due to i) spontaneous emission, and ii) fluctuations in the photon number, that are associated with the decay rates γ and κ, respectively. In particular, in the strong coupling regime photon number

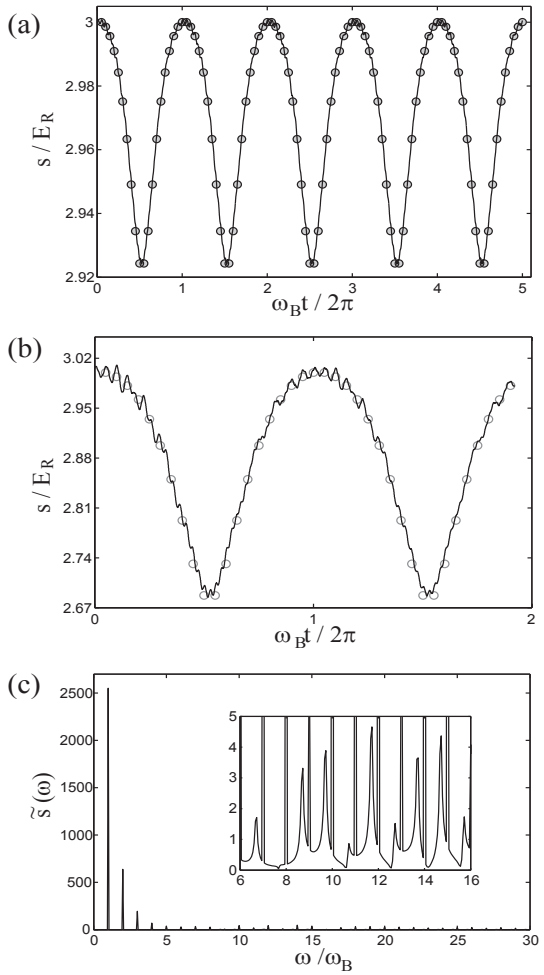

Figure 3.2. Calculated evolution of lattice depth $s(t)$ normalized to the recoil energy for ^{87}Rb atoms undergoing 840 Hz Bloch-Zener oscillations in a 780 nm lattice with $s \approx 3E_R$. Lines: numerical solution to Eqs. (3.3) and (3.4). Dots: self-consistent adiabatic approximation of Eqs. (3.9) and (3.10). (a) $Ng_0^2/(\kappa\Delta) = 0.4$. (b) Close-up of lattice depth oscillations with stronger coupling, $Ng_0^2/(\kappa\Delta) = 1$. Non-adiabatic effects are seen in the line. (c) Fourier transform $\tilde{s}(\omega)$ of result in (b), showing harmonics of fundamental frequency $\omega_{\rm B}$. Inset: Close-up of $\tilde{s}(\omega)$ at higher frequencies. Harmonics of $\omega_{\rm B}$ appear as sharp vertical lines. In addition, one sees much weaker, broad, Fourier components due to band excitation, corresponding to the rapid oscillations in (b). The actual individual values of the parameters used (or assumed in the case where only ratios enter) in the calculations were (see text): $N = 5 \times 10^4$, $g_0 = 2\pi \times 2.8$ MHz, $\kappa = 2\pi \times 1.0$ MHz. In (a) $\Delta = 2\pi \times 1.0$ THz, $\eta = 2\pi \times 39$ MHz; in (b) and (c) $\Delta = 2\pi \times 0.39$ THz, $\eta = 2\pi \times 28$ MHz.

fluctuations can significantly heat atoms inside an optical cavity [13]. We quantify the heating effect via the increase in the width σ_p of the atom's momentum distribution according to $\mathrm{d}\,\sigma_p^2/\,\mathrm{d}\,t = 2D$. The diffusion constant $D = \int_0^\infty dt'[\langle F_{\rm dip}(t)F_{\rm dip}(t+t')\rangle - \langle F_{\rm dip}\rangle^2]$ [28] involves two-time correlations of the dipole force $F_{\rm dip}$, and hence of the intracavity electric field. It has been calculated for atoms in cavities in [29] and has two terms. The first occurs in any standing-wave light field and at low saturation is given by $D_{\rm sw} = \hbar^2k^2/2\tau_{\rm sp}$ [28], where $\tau_{\rm sp}^{-1} = 2\gamma|\alpha|^2 g_0^2/\Delta^2$ is the spontaneous emission rate at an antinode. The second term, specific to cavities, is $D_{\rm cav} = 2D_{\rm sw}\,C\sin^2(2k_cz)$. This diffusion limits the coherent measurement time, which we take to be the time τ when the momentum distribution has a width equal to one half of the first Brillouin zone, i.e. $\sigma_p = \hbar k_c$. Then $\tau = \tau_{\rm sp}/(1+C)$, where we have replaced $\sin^2(2k_cz)$ by 1/2 - a good approximation in the ground band for a lattice of depth $s = 3E_{\rm R}$.

The BZOs can be observed by detecting the photon current $|\alpha(t)|^2\kappa$ transmitted through the cavity which is directly proportional to the depth $s(t)$ of the lattice ($s = \hbar g_0^2|\alpha|^2/\Delta$, see Eq. (3.4)), whose evolution is shown in Fig. 3.2. For an estimate of the measurement precision, let us write the detection rate as $R[1+\epsilon\cos(\omega t)]$. After measuring this for a time τ with detectors having an efficiency ξ, the shot noise gives an uncertainty in the oscillation frequency of $\sigma_\omega \approx 2\pi\tau^{-3/2}/(\epsilon\sqrt{\xi R})$, in which τ^{-1} comes from the linewidth due to the finite duration of the measurement, and $\tau^{-1/2}$ comes from the shot noise in this bandwidth. This simple estimate is close to the Cramér-Rao lower bound [30], the limit given by the information content of the signal. For small ϵ, $R \approx |\alpha|^2\kappa$, then the frequency uncertainty can be written as $\sigma_\omega \approx 2\pi\frac{s}{\hbar}\frac{1}{\epsilon\sqrt{\xi}}(\frac{g_0^2}{\kappa\Delta})^2(\frac{1}{C}+1)^{3/2}$. In order to bring out the implicit dependence on the number of atoms N contained in this result, we define the parameter $x = Ng_0^2/(\kappa\Delta)$. Referring to Eq. (3.10), if the number of atoms is increased then proportional increases in the laser detuning and intensity maintain constant values of s, x and ϵ, while the measurement time τ and the intra-cavity power both increase by the factor N. With this scaling, the measurement time, detuning and frequency uncertainty are given by

$$\tau = \frac{\hbar}{sx}\frac{NC}{1+C} \tag{3.11}$$

$$\Delta = \frac{2\gamma}{x}NC \tag{3.12}$$

$$\sigma_\omega \approx \frac{2\pi s x^2}{\sqrt{\xi}\hbar\epsilon}\frac{1}{N^2}\left(\frac{1}{C}+1\right)^{3/2}. \tag{3.13}$$

The uncertainty σ_ω therefore decreases rapidly with a dramatic $1/N^2$ dependence which ultimately derives from the continuous observation of the oscillations (via the enhanced measurement time τ).

Small s reduces σ_ω, but the lattice must support the atoms against gravity. We find that $s = 3E_R$ is a reasonable compromise. In the example of Fig. 3.2(a) we have chosen $x = 0.4$, which gives $\epsilon = 1.3\%$ in this lattice. Taking a reasonable number of atoms, let us say 5×10^4, a readily achieved cooperativity of $C = 1.3$, and a photon detector with 60% efficiency, brings σ_ω/ω_B to 1ppm. From

the definitions of x and C this requires a detuning of $\Delta = 2\pi \times 1$ THz and from Eq. (3.11) a measurement time of only $\tau = 1\,\mathrm{s}$. These numbers fix the ratio $g_0^2/\kappa = 2\pi \times 7.8$ MHz. If we choose $\kappa = 2\pi \times 1$ MHz, then using $s = \hbar g_0^2 |\alpha|^2/\Delta$, this means there are on average > 1400 photons in the cavity.

We have not included direct atom-atom interactions in the model discussed here. These can lead to quasimomentum-changing transitions (non-vertical transitions in the language of [31]) which dephase the BZOs. However, as summarized in the opening paragraphs of this paper, long-lived BZOs have already been successfully demonstrated in cold gases containing many atoms, and so it is a question of degree, i.e. at what atom density and interaction strengths do the interactions become important? An experiment investigating the control of interaction-induced dephasing of BZOs in a Bose-Einstein condensate has recently been reported [32]. Using a Feshbach resonance they were able to increase their dephasing time from a few to more than 20 thousand BZO periods. From the details of their measurements we estimate that, for our example given immediately above involving 5×10^4 atoms, the dephasing due to collisions is negligible for reasonable cavity geometries. The effect becomes significant on increasing the number of atoms to several million, but can be suppressed by tuning to a Feshbach resonance [32]. Large detuning and laser power impose a practical limit on the useful atom number at about this level anyway.

For atoms being continuously measured, an important source of dephasing is quantum measurement back-action. This effect is included in the estimate above in a quasi-classical way through the diffusive heating of the atoms by fluctuations of the cavity light field. The cavity field suffers fluctuations because it is dissipatively coupled to the outside world and it is precisely the light escaping from the cavity (at rate κ) that contains the information about the state of the atoms. In other words, it is the cavity decay that is doing the measuring. For our parameters, $\tau < \frac{1}{2}\tau_{\mathrm{sp}}$ because $C > 1$, and therefore it is the fluctuations due to cavity decay that limit the measurement time, rather than the spontaneous emission. We plan to perform a more microscopic study of the measurement back-action in the future.

In conclusion, we predict that the force on a small cold atom cloud can be measured very accurately by a new method based on BZO oscillations in an optical cavity. The BZO oscillations are measured continuously by monitoring the light that leaks out of the cavity. This enables a relatively fast and high precision measurement of the oscillation frequency, the error being given by Eq. (3.13). Our treatment of the problem is based upon solving the coupled equations of motion for the atoms and light. This gives a detailed picture of the dynamics, including the adiabatic and non-adiabatic aspects.

We note that since the submission of this paper a related proposal on monitoring of Bloch oscillations using an optical cavity has appeared [33].

Acknowledgements

We thank Pavel Abumov, Donald Sprung and Wytse van Dijk for discussions. Funding was provided by NSERC (Canada), EPSRC, QIPIRC and the Royal Society (UK). Part of this work was done during D.O.'s stay at the Institut Henri Poincare - Centre Emile Borel. He thanks this institution for hospitality and support.

Bibliography

[1] F. Bloch, Z. Phys. **52**, 555 (1928); C. Zener, Proc. R. Soc. A **145**, 523 (1934).

[2] J. Feldmann, K. Leo, J. Shah, D. A. B. Miller, J. E. Cunningham, T. Meier, G. von Plessen, A. Schulze, P. Thomas, and S. Schmitt-Rink, Phys. Rev. B **46**, 7252 (1992); C. Waschke, H. G. Roskos, R. Schwedler, K. Leo, and H. Kurz, K. Köhler, Phys. Rev. Lett. **70**, 3319 (1993).

[3] J.P. Reynolds and M. Luban, Phys. Rev. B **54**, R14301 (1996).

[4] R. Battesti, P. Cladé, S. Guellati-Khélifa, C. Schwob, B. Grémaud, F. Nez, L. Julien, and F. Biraben, Phys. Rev. Lett. **92**, 253001 (2004); P. Cladé, E. de Mirandes, M. Cadoret, S. Guellati-Khélifa, C. Schwob, F. Nez, L. Julien, and F. Biraben, Phys. Rev. Lett. **96**, 033001 (2006).

[5] M. Ben Dahan, E. Peik, J. Reichel, Y. Castin, and C. Salomon, Phys. Rev. Lett. **76**, 4508 (1996); E. Peik, M. Ben Dahan, I. Bouchoule, Y. Castin, and C. Salomon, Phys. Rev. A **55**, 2989 (1997).

[6] S.R. Wilkinson, C. F. Bharucha, K. W. Madison, Q. Niu, and M. G. Raizen, Phys. Rev. Lett. **76**, 4512 (1996).

[7] B.P. Anderson and M.A. Kasevich, Science **282**, 1686 (1998).

[8] O. Morsch, J. H. Müller, M. Cristiani, D. Ciampini, and E. Arimondo, Phys. Rev. Lett. **87**, 140402 (2001).

[9] G. Roati, E. de Mirandes, F. Ferlaino, H. Ott, G. Modugno, and M. Inguscio, Phys. Rev. Lett. **92**, 230402 (2004).

[10] G. Ferrari, N. Poli, F. Sorrentino, and G. M. Tino, Phys. Rev. Lett. **97**, 060402 (2006).

[11] I. Carusotto, L. P. Pitaevskii, S. Stringari, G. Modugno, and M. Inguscio, Phys. Rev. Lett. **95**, 093202 (2005).

[12] C.J. Hood, M. S. Chapman, T. W. Lynn, and H. J. Kimble, Phys. Rev. Lett. **80**, 4157 (1998); P. Münstermann, T. Fischer, P. W. H. Pinkse, and G. Rempe, Opt. Comm. **159**, 63 (1999); M.

Trupke, J. Goldwin, B. Darquié, G. Dutier, S. Eriksson, J. Ashmore, and E. A. Hinds, Phys. Rev. Lett. **99**, 063601 (2007).

[13] J. Ye, D. W. Vernooy, and H. J. Kimble, Phys. Rev. Lett. **83**, 4987 (1999); C. J. Hood, T. W. Lynn, A. C. Doherty, A. S. Parkins, and H. J. Kimble, Science **287**, 1447 (2000); P. W. H. Pinkse, T. Fischer, P. Maunz, G. Rempe, Nature **404**, 365 (2000); S. Gupta, K. L. Moore, K. W. Murch, and D. M. Stamper-Kurn, Phys. Rev. Lett **99**, 213601 (2007).

[14] S. Slama, C. von Cube, B. Deh, A. Ludewig, C. Zimmermann, and P. W. Courteille, Phys. Rev. Lett. **94**, 193901 (2005); P. Treutlein, D. Hunger, S. Camerer, T. W. Hänsch, and J. Reichel, Phys. Rev. Lett. **99**, 140403 (2007); Y. Colombe, T. Steinmetz, G. Dubois, F. Linke, D. Hunger, and J. Reichel, Nature **450**, 272 (2007); F. Brennecke, S. Ritter, T. Donner, T. Esslinger , Science **322**, 235 (2008).

[15] C. Maschler and H. Ritsch, Phys. Rev. Lett. **95**, 260401 (2005); I. B. Mekhov, C. Maschler and H. Ritsch, Nat. Phys. **3**, 319 (2007).

[16] W. H. Louisell and J. H. Marburger, IEEE J. Quantum Electron. **QE-3**, 348 (1967).

[17] P. Horak and H. Ritsch, Phys. Rev. A **63**, 023603 (2001).

[18] Langevin fluctuation terms do not appear in (3.3) if the bath is at thermal equilibrium. See p 343 of C. Cohen-Tannoudji, J. Dupont-Roc and G. Grynberg, *Atom-Photon Interactions* (Wiley, New York, 1992).

[19] M. Holthaus and D. W. Hone, Phil. Mag. B **74**, 105 (1996).

[20] Q. Thommen, J. C. Garreau and V. Zehnlé, Phys. Rev. A **65**, 053406 (2002).

[21] M. Glück, A. R. Kolovsky, H. J. Korsch and N. Moiseyev, Eur. Phys. J. D **4**, 239 (1998).

[22] M. Holthaus, J. Opt. B: Q. Semiclass. Opt. **2**, 589 (2000).

[23] J. Zapata, A. M. Guzmán, M. G. Moore, and P. Meystre, Phys. Rev. A **63**, 023607 (2001).

[24] T. Hartmann, F. Keck, H. J. Korsch and S. Mossmann, N. J. Phys. **6**, 2 (2004).

[25] J. Larson, Phys. Rev. A **73**, 013823 (2006).

[26] M. Abramowitz and I. Stegun, *Handbook of Mathematical Functions* (National Bureau of Standards, Washington, 1964).

[27] W. V. Houston, Phys. Rev. **57**, 184 (1940).

[28] J. P. Gordon and A. Ashkin, Phys. Rev. A **21**, 1606 (1980).

[29] G. Hechenblaikner, M. Gangl, P. Horak, and H. Ritsch, Phys. Rev. A **58**, 3030 (1998).

[30] S. M. Kay, *Fundamentals of Statistical Signal Processing: Estimation theory* (Prentice Hall International Editions, London, 1993).

[31] E. J. Mueller, Phys. Rev. A **66**, 063603 (2002).

[32] M. Gustavsson *et al.*, Phys. Rev. Lett. **100**, 080404 (2008).

[33] B. M. Peden, D. Meiser, M. L. Chiofalo and M. J. Holland, Phys. Rev. A **80**, 043803 (2009).

Chapter 4

Band-structure loops and multistability in cavity QED

Preface

Bloch oscillations, as explained in the introductory section in Chapter 3, can be understood as a consequence of adiabatic dynamics in a periodic potential. The quasimomentum evolves linearly as a function of time but the atoms are predominantly confined to a single band leading to a repeated sampling of the same band. For a Bose Einstein condensate (BEC) in an optical lattice, collisional inter-atomic interactions can be taken into account at the meanfield level using the Gross-Pitaevskii equation, a type of nonlinear Schrodinger equation. The resulting band structure has previously been shown to develop loop shapes when the interaction strength exceeds a certain threshold, in [102, 103]. The presence of loops in the band can have a profound effect on Bloch oscillations since the system will have to make non-adiabatic jumps once the 'edge' of a loop is reached and this non-adiabaticity is independent of the size of the force [102, 103]. In our system of interest we do not include direct atom-atom interactions, but nonetheless, since the atoms are all interacting with the cavity light field an effective mutual interaction is set up. In this chapter we work out the nonlinear eigenvalue equation and associated energy functional that govern this effective atom-atom interaction and show that they lead to loops in the dispersion relation, similar to the case of an interacting BEC in an optical lattice. Note that in Chapter 5 our choice of parameters for the Bloch oscillation proposal is designed to avoid such looped solutions.

To each solution for the atomic wavefunction there is a corresponding light field in the cavity. The presence of loops in the band structure therefore manifests itself as multistability in the cavity photon number. For an unaccelerated BEC (quasimomentum $q = 0$ in our language) in an optical cavity, the hysteresis derived from such a bistability was experimentally observed in [79]. In the

work presented in this chapter we include the quasimomentum degree of freedom and it leads to a richer situation including tristability. A convenient mathematical framework to study problems where the number of solutions suddenly changes as a parameter is smoothly varied, i.e., the study of bifurcations, is catastrophe theory [114]. We have analysed our problem in the framework of catastrophe theory and show that the system under consideration can be described by a swallowtail catastrophe.

Abstract

We calculate the band structure of ultracold atoms located inside a laser-driven optical cavity. For parameters where the atom-cavity system exhibits bistability, the atomic band structure develops loop structures akin to the ones predicted for Bose-Einstein condensates in ordinary (non-cavity) optical lattices. However, in our case the nonlinearity derives from the cavity back-action rather than from direct interatomic interactions. We find both bi- and tri-stable regimes associated with the lowest band, and show that the multistability we observe can be analyzed in terms of swallowtail catastrophes. Dynamic and energetic stability of the mean-field solutions is also discussed, and we show that the bistable solutions have, as expected, one unstable and two stable branches. The presence of loops in the atomic band structure has important implications for proposals concerning Bloch oscillations of atoms inside optical cavities [Peden *et al.*, Phys. Rev. A **80**, 043803 (2009), Prasanna Venkatesh *et al.*, Phys. Rev. A **80**, 063834 (2009)].

4.1 Introduction

Optical bistability is a manifestation of nonlinearity in optical systems which is well known in the laser physics community [1, 2] (see also [3] and [4] and references therein). It describes a situation in which there are two possible stable output light intensities for a single input intensity, and occurs when an optical medium with a nonlinear refractive index is placed inside an optical cavity formed from two mirrors. The bistable behaviour results from the combination of the nonlinearity of the medium with the action of the feedback provided by the mirrors.

A new addition to the family of systems displaying optical bistability has recently been demonstrated in experiments performed by the ultracold atom groups at Berkeley [5] and the ETH [6] who found optical bistability in systems comprising of vapors of ultracold atoms trapped inside optical cavities which are driven by laser light. The atomic vapor acts as a dielectric medium and, despite being tenuous, can significantly perturb the light in a cavity with a small mode volume and high finesse if the cooperativity $\mathcal{C}_N$ is in the regime $\mathcal{C}_N \equiv Ng_0^2/2\kappa\gamma > 1$, where N is the number of atoms, g_0 is the single photon Rabi frequency, 2γ is the atomic spontaneous emission rate in free space, and 2κ is the cavity energy damping rate. The perturbation of the light by the atoms is nonlinear and distorts the cavity lineshape away from being a lorentzian which is symmetric about the resonance frequency into one with an asymmetric shape. For large enough cooperativity the lineshape becomes folded over (see Fig. 4.2 below), so that for a certain range of frequencies there are three possible output light intensities (two stable, one unstable) from the cavity for a single input intensity. The experiments [5] and [6] exhibited this optical bistability as a hysteresis effect seen by chirping the laser frequency through the cavity resonance from above and below the resonance: a sudden jump in the intensity of light transmitted through the cavity was observed which occurred at two different frequencies, depending upon the direction of the chirp.

An important difference between traditional laser systems and the ultracold atom experiments [5, 6] is the origin of the nonlinearity. In the former case the nonlinearity of the medium occurs in its polarization response, i.e. it arises from the internal degrees of freedom of the atoms. By contrast, in the ultracold atom experiments the detuning of the cavity from atomic resonance was large enough that the polarization response was in the linear regime. The nonlinearity was instead due to the response of the centre-of-mass wave function of the atoms: the atoms re-arrange their position distribution according to the balance between the dipole force applied by the intracavity light field (which forms a periodic lattice) and their zero-point energy. As a consequence, the depth of the optical lattice that forms inside the cavity in experiments like [5] and [6] is not fixed purely by the drive laser intensity, as is the case in standard optical lattices made by interfering laser beams in free space. Rather, when $\mathcal{C}_N > 1$ the depth of the lattice is sensitive to the spatial distribution of the atoms trapped in the cavity, and, in turn, the atoms' center-of-mass wave function is sensitive to the lattice depth. This feedback nonlinearity, which leads to different amounts of transmitted/reflected light for a given input intensity depending on the spatial distribution of the

atoms, has been previously employed to detect the presence of a single atom in a cavity [7], as well as to monitor the motion of atoms trapped in cavities [8]. More recently, there has also been considerable theoretical interest in the effect of the feedback nonlinearity upon the many-body quantum state of ultracold atoms in cavities [9, 10, 11, 12, 13]. We note, in particular, the theoretical work on self-organisation and related phenomena [14], culminating in the experimental observation of the Dicke quantum phase transition [15].

Striking nonlinear phenomena also occur when ultracold atoms are trapped in standard "fixed" free-space lattices [16]. Of special interest to us here are the curious swallowtail loops that occur in the band structure (energy versus quasi-momentum) of atomic Bose-Einstein condensates (BECs) in one-dimensional optical lattices. These loops have been studied theoretically by a number of groups [17, 18, 19, 20, 21] in order to explain the breakdown in superfluidity observed in experiments where a BEC flows through a lattice [22, 23]. The loops correspond to multiple solutions for the atomic wave function within a single band for a certain range of quasi-momenta. They can occur either around the boundaries of the Brillouin zone or the center, depending upon the band and the sign of the interactions. They manifest themselves physically via a dynamical instability that destroys the superflow. However, the nonlinearity responsible for the swallowtail loops in the free-space lattices is provided by the interatomic interactions, which become important at the densities required for Bose-Einstein condensation. The loops occur when the strength of the interactions is above a critical value [17, 18], and therefore non-interacting atoms in an optical lattice do not display these instabilities. Our purpose in this paper is to investigate whether the cavity feedback nonlinearity associated with optical bistability in ultracold atoms can also lead to loops in the atomic band structure. As we shall see, the answer to this question is in general affirmative, and so band structure loops appear to be a robust phenomenon which appear whatever the source nonlinearity, although the structure and location of the loops does depend on the details of the nonlinearity.

One consequence of loops in the atomic band structure is a hysteresis effect [19] if the quasi-momentum is swept through the band, and a consequent loss of adiabaticity even if the quasi-momentum is swept infinitely slowly [24]. Recent experiments on a two-site lattice have confirmed this scenario [25]. These effects have implications for experiments that use Bloch oscillations of cold atoms in optical lattices for high precision measurements, for example to determine the fine structure constant α [26], to measure gravity [27, 28], or to investigate Casimir-Polder forces [29]. The band structure hysteresis is reminiscent of the hysteresis described above in the context of the optical bistability experiments [5] and [6]. Indeed, as we shall show in this paper, for atoms in an optical cavity the two effects are different sides of the same coin, one being seen in the light and the other in the atoms. Of particular relevance, therefore, are two recent proposals [30, 31] concerning Bloch oscillations of atoms inside optical cavities that rely upon the modification of the transmitted/reflected light arising from the feedback nonlinearity as a non-destructive measurement of the Bloch oscillations. The presence of loops will severely disrupt the Bloch oscillations. In the

case where the nonlinearity has its origin in atom-atom interactions the loops can be eliminated by, e.g., using spin polarized fermions [29] or by reducing the interactions via a Feshbach resonance [32]. However, when the nonlinearity is due to the feedback nonlinearity these methods do not apply, and one of our aims here is see if there are regimes where the feedback nonlinearity is present and leads to a modification of the light, but remains below a critical value needed to form loops in the atomic band structure. In order to allow the origin of the nonlinearity to be clearly identified, we shall only consider non-interacting atoms in this paper, but our calculations can be easily extended to include interactions.

The plan for the rest of the paper is as follows. In Section 4.2 we give a brief description of the system and introduce the mean-field hamiltonian describing cold atoms dispersively interacting with the single mode of a cavity. In Section 4.3 we derive a reduced hamiltonian describing the nonlinear evolution for the atomic field after the adiabatic elimination of the light field. In Section 4.4 we calculate the band structure by two different methods that solve for the spatially extended eigenstates (Bloch states) of the reduced hamiltonian, and show that the two methods give the same results. We find that for certain parameter regimes, the energy as a function of quasi-momentum develops loop structures. In Section 4.5 we recall the optical bistability in atom-cavity systems discussed by [5, 6] and make the connection between the loop dispersions and bistability. In Section 4.6 we develop an analytical estimate for the critical pump strength necessary to generate loops and in Section 4.7 we test this result by illustrating how the band structure depends on laser detuning and laser intensity, i.e. the birth and death of loops as these parameters are varied. In Section 4.8, we show that for quasi-momentum $q \neq 0$ the system can exhibit tristability (five solutions for the steady state cavity photon number).

A convenient mathematical framework for describing bifurcations of a system whereby there is a sudden change in the number of solutions as a parameter is smoothly changed is catastrophe theory [33, 34, 35, 36, 37]. Catastrophe theory was applied to the problem of optical bistability in the late 1970s by a number of authors including Gilmore and Narducci [38] and Agrawal and Carmichael [39]. In Section 4.9 we relate the problem of atom-cavity multistability to catastrophe theory and show that the system under consideration can be described by swallowtail catastrophes organized by an (unobserved) butterfly catastrophe and use this to understand multistability. This is followed in Section 4.10 by a discussion of the stability of these solutions and finally we conclude in Section 4.11. There is also an appendix which summarizes some concepts of catastrophe theory.

4.2 The hamiltonian

Consider a gas of N ultracold atoms inside a Fabry-Perot optical cavity. The atoms interact quasi-resonantly with a single cavity mode of the electromagnetic field of frequency ω_c, and it varies along the cavity axis as $\cos(k_c z)$, where $k_c = \omega_c/c$. This cavity mode is externally pumped by a laser of

frequency ω_p. The relevant frequency relations can be characterized with the two detunings

$$\Delta_c \equiv \omega_p - \omega_c, \tag{4.1}$$

$$\Delta_a \equiv \omega_p - \omega_a, \tag{4.2}$$

where ω_a is the atomic transition frequency. In the dispersive regime, the occupation of the excited atomic state is vanishingly small and it can be adiabatically eliminated. A one-dimensional hamiltonian for the atom-cavity system in the dispersive regime can then be written as [9, 10]

$$H = -\hbar\Delta_c \hat{a}^\dagger \hat{a} + i\hbar\eta\left(\hat{a}^\dagger - \hat{a}\right) + \int \mathrm{d}z\ \hat{\Psi}^\dagger \left[-\frac{\hbar^2}{2M}\frac{\partial^2}{\partial z^2} + \frac{\hbar g_0^2}{\Delta_a}\ \hat{a}^\dagger\hat{a}\cos^2(k_c z)\right]\hat{\Psi}, \tag{4.3}$$

where $\hat{\Psi}(z,t)$ and $\hat{a}(t)$ are the field operators for the atoms and the cavity photons, respectively. We have written the hamiltonian in a frame rotating with the pump laser frequency ω_p, which leads to the appearance of the two detunings. The first term is just the free field evolution of the cavity mode. The second term represents the laser coherently pumping the cavity at rate η, and the third term describes the atomic part of the hamiltonian. It consists of a kinetic energy part and a potential energy part. The potential energy term can either be understood as the atom moving in a periodic potential with amplitude $(\hbar g_0^2/\Delta_a)\langle\hat{a}^\dagger\hat{a}\rangle$, or, if combined with the first term in the hamiltonian, as a shift in the resonance frequency of the cavity due to the coupling between the atom and the field (see also Eq. (4.5) below).

The Heisenberg equations of motion for the atom and photon field operators can be obtained from the above hamiltonian. In this paper we are interested in properties at a mean-field level, where operators are replaced by their expectation values and correlations between products of operators are neglected. In other words, the light is assumed to be in a coherent state with amplitude $\alpha(t) = \langle\hat{a}\rangle$, and the atoms are assumed to all share the same single-particle wave function $\psi(x,t) = \langle\hat{\Psi}\rangle/\sqrt{N}$. From the Heisenberg equations these amplitudes obey the following coupled equations of motion [40]

$$i\frac{\partial\psi}{\partial t} = \left(-\frac{\partial^2}{\partial x^2} + U_0\, n_\mathrm{ph}\cos^2(x)\right)\psi, \tag{4.4}$$

$$\frac{\mathrm{d}\alpha}{\mathrm{d}t} = \left(i\Delta_c - iNU_0\int \mathrm{d}x\cos^2(x)|\psi(x)|^2 - \kappa\right)\alpha + \eta, \tag{4.5}$$

where we have scaled energies by the recoil energy $E_\mathrm{R} = \hbar^2 k_\mathrm{c}^2/2M$, and time by $\hbar/E_R$. The depth of the periodic potential seen by the atoms is then given by $U_0\, n_\mathrm{ph}$, where $n_\mathrm{ph} \equiv |\alpha|^2$ is the mean number of photons in the cavity, and U_0 is defined as

$$U_0 \equiv \hbar g_0^2/(\Delta_a E_\mathrm{R})\ . \tag{4.6}$$

The damping rate κ (in units of E_R) of the amplitude of the light field in the cavity has been added

into the equation of motion in order to account for a markovian coupling between the cavity mode and a zero temperature bath. We have also introduced the dimensionless length $x \equiv k_c z$. In the above equations, any fluctuations induced by the reservoirs have been neglected. This is justified when considering relatively large quantum numbers, for corrections see reference [12].

In this paper we are interested in the band structure and this requires the quasi-momentum to be a good quantum number. Physically, this implies that we are studying delocalized atomic wave functions which cover many lattice sites (this is closer to the situation realized in the experiment [6] than that realized in [5] where the atoms were localized to just a few sites). We shall therefore expand the wave function $\psi(x,t)$ in Bloch waves, as will be detailed in subsequent sections. It thus makes sense to normalize $\psi(x,t)$ over one period of the potential as $\int_0^\pi |\psi|^2 dx = \pi$, and also evaluate the integrals appearing in the above equations over one period. In particular, the integral in Eq. (4.5) which determines the coupling between the atoms and the light will be defined by

$$\langle \cos^2(x) \rangle \equiv \frac{1}{\pi} \int_0^\pi |\psi(x)|^2 \cos^2(x) \mathrm{d}x. \tag{4.7}$$

4.3 The reduced hamiltonian

In this Section we shall eliminate the optical degrees of freedom from the hamiltonian in order to obtain a description only in terms of the atoms. This results in a nonlinear Schrödinger equation and an energy functional we shall refer to as the reduced hamiltonian.

Setting $\mathrm{d}\alpha/\mathrm{d}t = 0$ in Eq. (4.5) gives the steady state light amplitude in the cavity,

$$\alpha = \frac{\eta}{\kappa} \frac{1}{1 + i\frac{\Delta_c - NU_0\langle \cos^2(x) \rangle}{\kappa}} \tag{4.8}$$

which leads to the following equation for the steady state photon number

$$n_{\mathrm{ph}} = \frac{\eta^2}{\kappa^2 + \left(\Delta_c - NU_0 \langle \cos^2(x) \rangle\right)^2} \ . \tag{4.9}$$

In fact, this expression also holds to high accuracy in many time-dependent situations because κ is typically far greater than any frequency associated with the evolution of the external degrees of freedom of ultracold atoms. The light field is then slaved to the atoms and "instantaneously" adjusts itself to any change in $\psi(x,t)$. The steady state solution can then be substituted back into Eq. (4.4) to give us a single, closed, nonlinear Schrödinger equation for the atomic wave function

$$i\frac{\partial \psi}{\partial t} = \left(-\frac{\partial^2}{\partial x^2} + \frac{U_0\, \eta^2 \cos^2(x)}{\kappa^2 + \left(\Delta_c - NU_0 \langle \cos^2(x) \rangle\right)^2} \right) \psi \ . \tag{4.10}$$

The stationary solution $\psi(x,t) = \psi(x) e^{-i\mu t}$ of this equation leads to an expression for the eigen-

value μ of Eq. (4.10),

$$\mu[\psi,\psi^*] = \frac{1}{\pi}\int_0^\pi dx\left(\left|\frac{d\psi}{dx}\right|^2 + U_0 n_{\rm ph}\cos^2(x)|\psi(x)|^2\right). \tag{4.11}$$

If the Schrödinger equation (4.10) were linear, then the eigenvalue μ would be the energy of the atoms in state ψ. Furthermore, the functional (4.11) would serve as the energy functional from which this Schrödinger equation could be obtained as an equation of motion using Hamilton's equation

$$i\hbar\frac{\partial\psi}{\partial t} = \frac{\delta E[\psi,\psi^*]}{\delta\psi^*}\ . \tag{4.12}$$

i.e. $E[\psi,\psi^*] = \mu[\psi,\psi^*]$ for a linear equation. However, this is not the case here. Instead, the eigenvalue μ is the chemical potential which is related to the true energy E via $\mu = \partial E/\partial N$ (a prominent example that illustrates this distinction is the Gross-Pitaevskii equation and its energy functional [21]). Using this fact, one can show that the true energy functional from which the equation of motion (4.10) can be derived is in fact [10, 13]

$$E[\psi] = \frac{N}{\pi}\int_0^\pi dx\left|\frac{d\psi}{dx}\right|^2 - \frac{\eta^2}{\kappa}\arctan\left(\frac{\Delta_c - \frac{NU_0}{\pi}\int_0^\pi \mathrm{d}x|\psi|^2\cos^2(x)}{\kappa}\right). \tag{4.13}$$

as can be verified by applying Hamilton's equation (4.12). We shall refer to this functional as the reduced hamiltonian. The first term represents the kinetic energy. The second term is an atom-light coupling dependent term that can be interpreted as follows. The phase shift of the steady state light field inside the cavity relative to the pump laser is, from Eq. (4.8),

$$\phi = \arctan\frac{\mathrm{Im}(\alpha)}{\mathrm{Re}\,(\alpha)} = \arctan\left(\frac{\Delta_c - \frac{NU_0}{\pi}\langle\cos^2(x)\rangle}{\kappa}\right)\ . \tag{4.14}$$

This allows us to rewrite the reduced hamiltonian as

$$E[\psi] = \frac{N}{\pi}\int_0^\pi \mathrm{d}x\left|\frac{\mathrm{d}\psi}{\mathrm{d}x}\right|^2 - I_{\rm ph}\phi\ , \tag{4.15}$$

where $I_{\rm ph} = \eta^2/\kappa$ is the incident photon current from the pump laser. Note that this hamiltonian looks similar in form to the effective quantum two-mode hamiltonians obtained in the optomechanical limit in [12] and [13], and also the ones describing bistability in [10].

4.4 Band structure

From now on we specialize to Bloch wave solutions. We begin by describing two methods for calculating the Bloch waves and their energies. Agreement between the two methods will be demonstrated.

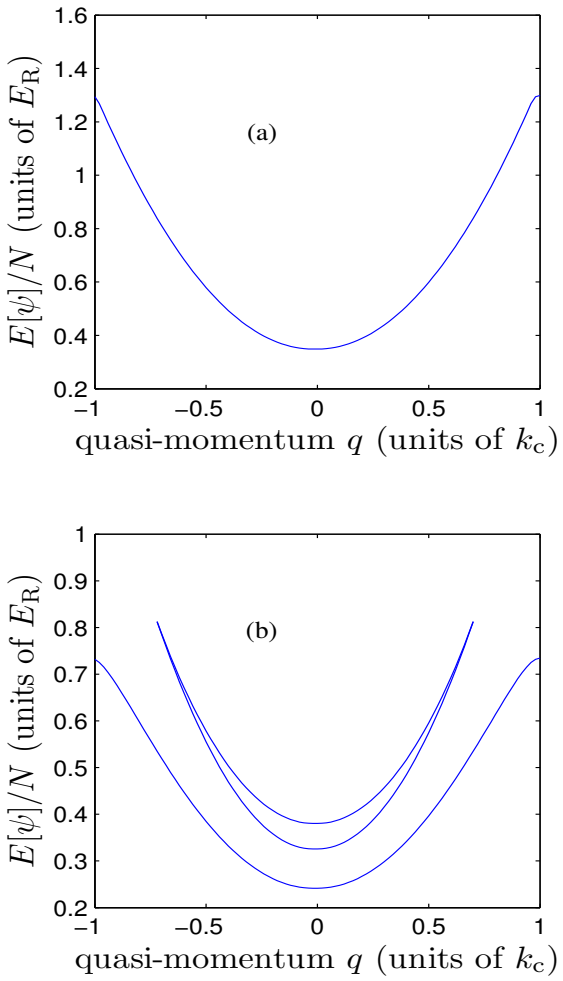

Figure 4.1. Energy loops in the first band. The curves were obtained by extremizing the reduced hamiltonian (4.13). For both (a) and (b) the laser pumping $\eta = 909.9\,\omega_{\rm R}$, the cavity decay $\kappa = 350\,\omega_{\rm R}$, the atom-light coupling $U_0 = \omega_{\rm R}$, and number of atoms $N = 10^4$. In (a) the pump-cavity detuning was $\Delta_c = 1350\,\omega_{\rm R}$, which gives no loops, and in (b) it was $\Delta_c = 3140\,\omega_{\rm R}$ which gives a loop symmetric about the band center as shown. As explained in the text, the number of photons in the cavity and hence the lattice depth change with q. For example, in (a) at $q = 0$ we have $n_{\rm ph} = 0.06$ and at $q = 1$ we have $n_{\rm ph} = 0.68$. In (b) at $q = 0$ we have for the lowest branch $n_{\rm ph} = 4.13$, for the middle branch $n_{\rm ph} = 0.28$, and for the upper branch $n_{\rm ph} = 2.4$. At $q = 1$ we have $n_{\rm ph} = 1.08$. At the point where the middle and upper branches meet we have $n_{\rm ph} = 0.58$.

4.4.1 Method 1: Energy extremization

The first method, which adapts that detailed in [18] for a static optical lattice, hinges on the observation that the potential in the Schrödinger Eq. (4.10) is periodic with period π (in dimensionless units). Despite the nonlinearity, the Bloch theorem [42, 43, 31] applies so that the eigenfunctions can be written as the product of a plane wave with wavenumber q, called the quasi-momentum, and an amplitude $U_q(x)$ which is periodic with the period of the lattice

$$\begin{aligned} \psi_q(x) &= e^{iqx} U_q(x), \\ U_q(x+\pi) &= U_q(x)\ . \end{aligned} \tag{4.16}$$

For the linear problem, the energies $E(q)$ are arranged into bands separated by gaps. In the so-called reduced zone scheme for the band structure, q lies in the first Brillouin zone $-1 \leq q < 1$, and the band energies are folded back into the first Brillouin zone.

The periodicity of $U_q(x)$ implies that it can be expanded as a Fourier series. The Bloch wave can therefore be written

$$\psi_q(x) = e^{iqx} \sum_n a_{q,n} e^{i2nx}. \tag{4.17}$$

The notation for the n^{th} expansion coefficient $a_{q,n}$ reflects the fact that it depends on the chosen value of q. This expansion can now be substituted into the reduced hamiltonian Eq. (4.13), and the resulting function numerically extremized with respect to the parameters $a_{q,n}$, maintaining the normalization of $\psi_q(x)$ throughout the procedure. We take the parameters $a_{q,n}$ to be real for the same reasoning as given in [18]. The Fourier series is terminated at some $n = R$, which is determined by the convergence of the energy eigenvalues as R is varied.

In Fig. 4.1 we plot the low lying part of energy spectrum $E[\psi_q]$ as a function of quasi-momentum resulting from the extremization. The values of κ and N are very close to the values used in the experiment with rubidium atoms described in [6], and the other parameters are chosen so as to exhibit the interesting behavior to be discussed in the rest of the paper. The two panels of Fig. 4.1 differ only in the value of the pump-cavity detuning Δ_c. Fig. 4.1a shows a result familiar from linear problems involving quantum particles in periodic potentials, but Fig. 4.1b shows a very different story: there are two other branches that together form a looped structure that is a manifestation of the nonlinearity of the reduced hamiltonian. As will be discussed more below, the loop shown in Fig. 4.1b belongs to the first band (in particular, it does not correspond to the second band because it only extends over part of the first Brillouin zone). Looped structures have been found before for BECs in static optical lattices [18, 17]. We will come back to the similarities and differences between our results and [18, 17] in the next section.

It is important to appreciate that, by virtue of the nonlinearity of the problem, the lattice depth

$n_{\rm ph}U_0$ is different at each value of the quasi-momentum shown in Fig. 4.1. Furthermore, the lattice depth is different for each of the curves even at the same values of q (except at degeneracies). In this sense, the band structure plots we display in this paper are non-standard because for static lattices the depth of the lattice is fixed for all values of q. In order to obtain the lattice depth at each point on a curve $E[\psi_{\rm q}]$ in Fig. 4.1, one should take the wave function that extremizes the energy functional (4.13) at that point and enter it into the integral $\langle\cos^2(x)\rangle$ appearing on the righthand side of Eq. (4.9) for the photon number. This change in lattice depth with detuning is reported in Fig. 4.2, but for the reader's convenience we have included some values at particular points q in the caption of Fig. 4.1.

The fact that, depending on the detuning Δ_c, there are either one or more steady state photon numbers for the cavity reminds us of the optical bistability observed in [5, 6]. There, as the cavity driving laser detuning was swept through the resonance, bistability was observed for certain pump strengths η. The bistability derives from quantum effects [41] in the sense that it is due to changes in the atomic center-of-mass wave function. It is distinct from standard semi-classical optical bistability [4]. The connection between the loops in the atomic band structure and optical bistability will be examined in detail in Section 4.5. To complete this section we look at an alternative method for determining the eigenfunctions of the effective hamiltonian which makes the connection with bistability more transparent.

4.4.2 Method 2: Self-consistency equation

In the second method, the strategy is to solve Eq. (4.9) directly for the steady-state photon number. This equation contains $n_{\rm ph}$ both explicitly on the left hand side and implicitly on the right hand side through the atomic wave function $\psi_q(x, n_{\rm ph})$ appearing in the integrand of the integral

$$\langle\cos^2(x)\rangle = \frac{1}{\pi}\int_0^\pi \cos^2(x)|\psi_q(x, n_{\rm ph})|^2{\rm d}x. \tag{4.18}$$

The photon number is not a parameter set from the outside (e.g. by the pump laser) but must be solved for self-consistently. In our notation for the wave function we have therefore included $n_{\rm ph}$ in the list of arguments rather than the list of parameters. The dependence of $\psi_q(x, n_{\rm ph})$ upon the number of photons is because the depth of the lattice in which the atoms sit is given by $U_0\, n_{\rm ph}$, as can be seen directly from the Schrödinger equation (4.4). Therefore, Eq. (4.9) must be solved self-consistently for $n_{\rm ph}$, and we will often refer to it as the "self-consistency equation". As mentioned in the introduction, the physical mechanism that gives rise to the feedback between the atoms and the light stems for the atom-light coupling, Eq. (4.7) [or Eq. (4.18)]. The atoms' spatial distribution controls the phase shift suffered by the light on traversing the cavity, and hence the cavity resonance condition, and therefore the amplitude of the light in the cavity. At the same time, the amplitude of the light determines the depth of the lattice which influences the atomic wave function.

One class of solutions to the self-consistency problem is provided by the Mathieu functions [44]. In fact, these provide *exact* solutions because the Schrödinger equation (4.4) for a particle in a sinusoidal potential is nothing but the Mathieu equation. Despite the fact that the amplitude of the sinusoidal potential in (4.4) itself depends on the solution $\psi_q(x, n_{\rm ph})$ of the equation, this amplitude evaluates to a constant because $\psi_q(x, n_{\rm ph})$ appears under the integral given by Eq. (4.7). All that is necessary is that the wave function that enters into the integral is the same as the wave function appearing in the rest of the Schrödinger equation. This is the case precisely when the self-consistency equation (4.9) is satisfied. This leads us to a very important point: by virtue of the self-consistency equation (4.9), the photon number $n_{\rm ph}$ is *completely equivalent*, in the sense of the information it carries, to the wave function ψ. Said another way, the Mathieu functions are specified by only two quantities: the value of the quasi-momentum and the depth of the potential. Thus, once we set the quasi-momentum, which is a parameter, the wave function is entirely determined by $U_0 n_{\rm ph}$, where U_0 is also a parameter. We shall frequently take advantage of the equivalence between ψ and $n_{\rm ph}$ in the rest of this paper because it allows us to replace the wave function by a single number $n_{\rm ph}$.

We shall denote the Mathieu functions by $\chi_{m,q,n_{\rm ph}}(x)$, where m is the band index. They satisfy Mathieu's equation which in our problem takes the form

$$\left(-\frac{\partial^2}{\partial x^2} + U_0 n_{\rm ph} \cos^2(x) \right) \chi_{m,q,n_{\rm ph}}(x) = \mu_{m,q,n_{\rm ph}} \chi_{m,q,n_{\rm ph}}(x) \ . \tag{4.19}$$

Our notation for the Mathieu functions indicates the full parametric dependence with the exception of the atom-light coupling strength U_0. Note that in the Mathieu functions we list $n_{\rm ph}$ as a parameter, like q, because that is the role it plays in the Mathieu equation. We therefore have that

$$\psi_{m,q}(x, n_{\rm ph}) = \chi_{m,q,n_{\rm ph}}(x). \tag{4.20}$$

Mathieu's functions can, of course, be written in Bloch form. In this paper we focus on the first band and so we shall suppress the band index from now on. We therefore have $\chi_{q,n_{\rm ph}}(x) = \exp(iqx) U_{q,n_{\rm ph}}(x)$. Substituting this Bloch form into the time-dependent Schrödinger equation (4.4) as $\psi_q(x, n_{\rm ph}, t) = \chi_{q,n_{\rm ph}}(x) \exp(-i\mu t)$ one obtains

$$\left(-\frac{\partial}{\partial x} + iq \right)^2 U_{q,n_{\rm ph}}(x) + U_0 n_{\rm ph} \cos^2(x) U_{q,n_{\rm ph}}(x) = \mu_{q,n_{\rm ph}} U_{q,n_{\rm ph}}(x). \tag{4.21}$$

This equation can either be solved numerically from scratch, or a package such as *Mathematica* can be used which gives the Mathieu functions for each value of q, and $U_0\, n_{\rm ph}$. For a particular choice of q, these Mathieu functions can now be used in (4.9) to find the value(s) of $n_{\rm ph}$ that give self-consistency.

There are two main differences between method 1 and method 2 described above. Firstly, method 1 is a variational calculation, whereas method 2 exploits the definition of the steady state photon

number to obtain a single nonlinear integral equation (4.9) which must be satisfied by the atomic wave function. Secondly, in method 2 we can explicitly set the band index whereas the variational wave function used in method 1 is rather more general. In spite of these differences, we find that the two methods are in complete agreement (to within numerical accuracy) for all the parameter ranges we were able to test (for very deep lattices method 1 becomes unworkable because a very large number of terms in the Fourier expansion are required). We have also checked that the two methods agree for higher bands.

It may at first seem surprising that two such seemingly different methods are equivalent. We emphasize that both stem from the non-linear Schrödinger equation (4.10), which is just Mathieu's equation with a potential depth which is set self-consistently. Method 1 minimizes an energy functional that is derived from this non-linear Schrödinger equation. In principle, one could minimize ansatze other than the Bloch functions we use here (e.g. localized functions), but these would not then satisfy the original non-linear Schrödinger equation (4.10) exactly. Method 2 is based upon the observation that wave functions that satisfy the self-consistency equation (4.9) are precisely the required solutions of the non-linear Schrödinger equation (4.10) providing we restrict ourselves to solutions which are Mathieu functions. Again, one could find other types of solution, but these would not satisfy Eq. (4.10).

An interesting question to ask is whether the nonlinearity of our problem mixes the linear bands, so that, for example the self-consistent first band is a superposition of Mathieu functions from different bands. This is not what we find. Instead, the solutions we have found all correspond to being from one or other band, but not a superposition. Method 2, in particular, allows us to explicitly set the band index and we are therefore able to identify all three curves shown in Fig. 4.1 as belonging to the first band (we have also checked that the Mathieu functions corresponding to all three curves are orthogonal to the Mathieu functions for the second band for the same three lattice depths). Actually, we do not find loops in higher bands for the parameter values considered in Fig. 4.1. Although in this paper we restrict our attention to the first band, we have found that we can have loops in the higher bands as well. The calculation of energy dispersions using the self-consistent method is numerically less demanding and so we will continue to use the latter for the remainder of this paper. In the next section we discuss optical bistability and its relation to loops in the band structure.

4.5 Bistability and Loops

As mentioned in the Introduction, optical bistability was discovered in the ultracold atom experiments [5] and [6] via a hysteresis effect as the detuning of the pump laser was swept from above and below the cavity resonance. This effect can be described theoretically by using the self-consistency equation to calculate the number of photons $n_{\rm ph}$ in the cavity at each value of the detuning (the

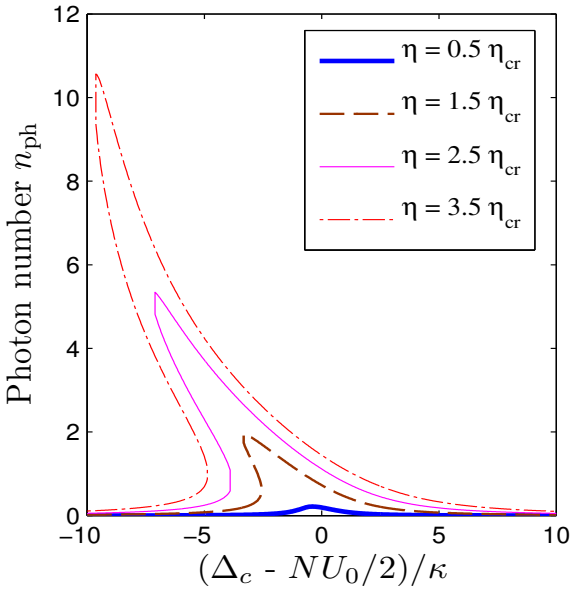

Figure 4.2. The steady state photon number inside the cavity as a function of detuning Δ_c for the parameters $\kappa = 350\,\omega_{\rm R}$, $U_0 = \omega_{\rm R}$, $N = 10^4$. Each curve is for a different value of the pump strength η: thick blue $\eta = 0.5\,\eta_{\rm cr}$, dashed brown $\eta = 1.5\,\eta_{\rm cr}$, thin magenta $\eta = 2.5\,\eta_{\rm cr}$, and dash-dotted red $\eta = 3.5\,\eta_{\rm cr}$. As can be seen, as η increases the lineshapes become more and more asymmetric and fold over at the critical pump strength $\eta_{\rm cr}(q=0) \equiv \eta_0 = 325\,\omega_{\rm R}$. The atomic wave function corresponds to the first band with $q = 0$.

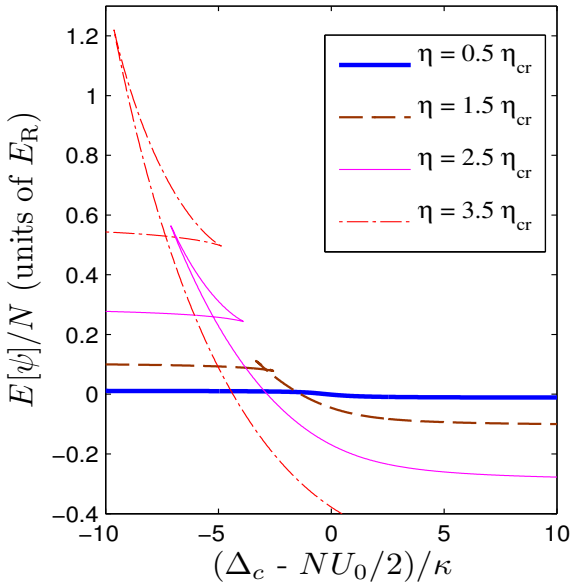

Figure 4.3. The energy given by the reduced hamiltonian (4.13) as a function of detuning Δ_c for the parameters $q = 0$, $\kappa = 350\,\omega_{\rm R}$, $U_0 = \omega_{\rm R}$, $N = 10^4$. Each curve is for a different value of the pump strength η: thick blue $\eta = 0.5\,\eta_{\rm cr}$, dashed brown $\eta = 1.5\,\eta_{\rm cr}$, thin magenta $\eta = 2.5\,\eta_{\rm cr}$, and dash-dotted red $\eta = 3.5\,\eta_{\rm cr}$. The critical pump strength is $\eta_0 = 325\,\omega_{\rm R}$. For $\eta > \eta_0$ swallowtail loops develop corresponding to bistability. The loops grow in size as η increases.

number of cavity photons can be measured directly from the photon current transmitted through the cavity which is given by $n_{\rm ph}\kappa$). The results are plotted in Fig. 4.2 for different values of the pump strength η. In the absence of atoms the cavity lineshape is a lorentzian centered at $\Delta_c = 0$ with a full width at half maximum 2κ. At small pump intensity, the presence of the atoms shifts the center of the resonance by $NU_0\langle\cos^2(x)\rangle$ while the shape is largely unaltered. But as η is increased, the lineshape curve becomes asymmetric and eventually folds over when η is above a critical value $\eta_{\rm cr}(q = 0) \equiv \eta_0$, indicating multiple solutions and hence bistability. $\eta_{\rm cr}(q)$ depends on the quasi-momentum and η_0 is defined as its value at $q = 0$.

In the folded over region, only one of the solutions (corresponding either to the highest or the lowest photon number) is seen at a time, depending upon the direction of the sweep. The middle branch cannot be accessed using this experimental protocol and is in any case unstable, as will be discussed at more length in Section 4.10.

Note that in Fig. 4.2 we have chosen the quantum state of the atoms to be the $q = 0$ Bloch state. In fact, this is the case for all the plots in this section because that is closest to the situation in the experiments that have been conducted so far. One of the main points of this paper is essentially to examine the extra degree of freedom conferred by the quasi-momentum. For atoms in ordinary optical lattices the quasi-momentum can be controlled by accelerating the lattice (rather than the atoms) via a phase chirp [45]. An accelerated lattice is hard to achieve inside a Fabry-Perot cavity, but if the atoms have a magnetic moment one can instead subject them to an inhomogeneous magnetic field so that a force is applied (or, of course, in a vertically oriented cavity the atoms will be accelerated by gravity). As is well known from the theory of Bloch oscillations, under a constant force F the quasi-momentum evolves according to the Bloch acceleration theorem [42, 43]

$$q(t) = q_0 + \frac{Ft}{k_c E_R} \tag{4.22}$$

where q and t are expressed in the dimensionless units given in Section 4.2, and q_0 is the quasi-momentum at time $t = 0$. The Bloch acceleration theorem requires that the evolution be adiabatic, and the implications of this for intra-cavity optical lattices have been discussed in [31], albeit without loops. The effect of a constant force is thus to sweep the system through the band at a constant rate and, in principle, any quasi-momentum can be achieved by switching off the magnetic field after an appropriate time delay.

Figure 4.3 depicts the energy versus detuning curves corresponding to the photon number versus detuning curves shown in Fig. 4.2. In the bistable regime, the energy curves in Fig. 4.3 develop swallowtail loops. This can be understood in terms of the familiar connection between bistability, hysteresis, and the change in the energy manifold described in detail by [19]. Consider one of the curves in Fig. 4.3 where there is bistability, e.g. the curve with $\eta = 3\eta_0$. For Δ_c values to the left and right of the swallowtail loop, the energy functional Eq. (4.13) has a single extremum corresponding to a particular wave function $\psi_q(x, n_{\rm ph})$. In the bistable region, the energy functional has the structure

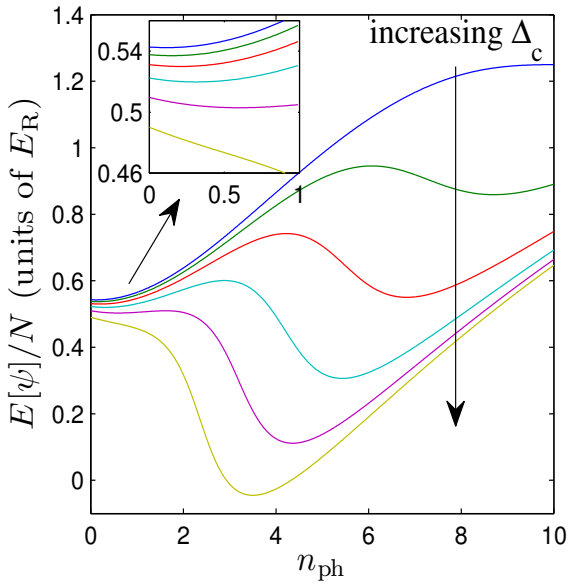

Figure 4.4. The double well structure of the energy of the reduced hamiltonian (4.13) as a function of cavity photon number $n_{\rm ph}$. Each curve is for a different value of the detuning Δ_c. The values are $\Delta_c = 1600, 2000, 2400, 2800, 3200, 3600\,\omega_{\rm R}$. The arrow indicates how the curves evolve as Δ_c increases. The top most curve (blue), and the bottom most curve (yellow), have only one minimum, whereas the rest of the curves have two minima (the inset shows a zoom-in of the curves close to $n_{\rm ph} = 0$) indicating bistability. Consequently, bistability only occurs for a certain limited range of Δ_c. The other parameters are $q = 0$, $\kappa = 350\,\omega_{\rm R}$, $U_0 = \omega_{\rm R}$, $N = 10^4$, $\eta = 3.5\,\eta_0$, where $\eta_0 = 325\,\omega_{\rm R}$.

of a double-well, furnishing three extrema: two minima and one maximum, that give the three branches of the loop corresponding to three different wave functions. This double-well structure is shown in Fig. 4.4 as a function of $n_{\rm ph}$ for different values of detuning Δ_c. Note that, as already observed above, the self-consistency equation (4.9) provides a direct mapping between the wave function and $n_{\rm ph}$.

Figures 4.2, 4.3, and 4.4 all show different aspects of hysteresis as Δ_c is swept either from above or below the cavity resonance. It is enlightening to see how it arises in Fig. 4.4. If the detuning is swept from below the resonance then initially there is a single solution for $n_{\rm ph}$, given by the minimum in the reduced energy functional which occurs at the very left hand side of Fig. 4.4, as best seen in the inset. When Δ_c is increased another solution appears at a larger value of $n_{\rm ph}$. However, this state of the system is not realized (for this direction of the detuning sweep), even when it becomes the global minimum, until the energy barrier between the two solutions vanishes and the left hand minimum disappears. The system then jumps to the new minimum at a larger value of $n_{\rm ph}$. The reverse happens when Δ_c is swept in the other direction. This hysteretic behavior is corroborated by Figs 4.2 and 4.3.

In the Section 4.6, a method for determining $\eta_{\rm cr}(q)$ is described. Generally, this requires a numerical computation, but for small values of the intracavity lattice depth an analytical expression can be worked out. It turns out that the dependence of $\eta_{\rm cr}$ on the atomic state quasi-momentum can be used to explain the loops in the energy quasi-momentum plots (Fig. 4.1).

4.6 Critical pump strength for bistability

4.6.1 Conditions for bistability

Returning to the cavity lineshape shown in Fig. 4.2, we recall that as the pump strength η is increased the steady state photon number in the cavity can exhibit bistability for a certain range of detuning Δ_c. Bistability first develops at a single value of the detuning, which we denote by $\Delta_c = \Delta_0$. The critical pump strength at which this bistability at Δ_0 occurs is $\eta_{\rm cr}(q)$, and in this section we want to calculate it. Let us first re-write the self-consistency equation (4.23) as

$$\frac{n_{\rm ph}}{n_{\rm max}} = \frac{1}{1+\left(\frac{\Delta_c - NU_0 f(U_0 n_{\rm ph}, q)}{\kappa}\right)^2}, \tag{4.23}$$

where $n_{\rm max} \equiv \eta^2/\kappa^2$ is the maximum number of the photons that can be in the cavity at steady state. In order to reinforce the idea that the wave function and the number of photons are really equivalent quantities, we have replaced the notation for the integral $\langle \cos^2(x) \rangle$ appearing in (4.23) by

$$f(U_0 n_{\rm ph}, q) \equiv \langle \cos^2(x) \rangle \ . \tag{4.24}$$

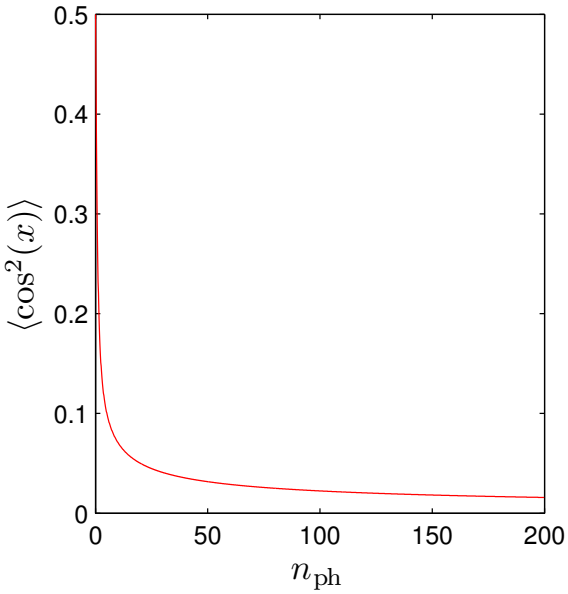

Figure 4.5. Plot of the atom-light overlap integral $f(n_{\rm ph}, q) = \langle \cos^2(x) \rangle$, first defined in Eq. (4.7), as a function of the cavity photon number $n_{\rm ph}$. The atomic wave function is taken to be the $q = 0$ Bloch wave of the first band, and the atom-light interaction is set at $U_0 = 5\,\omega_{\rm R}$. Note that the maximum value $f(n_{\rm ph}, q)$ can take is one half, irrespective of the values of U_0 and q. As $n_{\rm ph} \to \infty$ we find that $f(n_{\rm ph}, q) \to 0$.

This function is plotted in Fig. 4.5 for blue detuning ($\Delta_a > 0$) where we see that as the lattice gets deeper the atomic wave function adjusts to become more localized on the lattice nodes and reduce the overlap between the light and the atoms. Furthermore, the steep gradient at shallow lattices implies that the system is more sensitive, and so more nonlinear, at small photon numbers.

It is instructive to solve Eq. (4.23) graphically as the intersection between two functions of $n_{\rm ph}$, as shown in Fig. 4.6. The left hand side is a straight line whose gradient is $1/n_{\rm max}$. For very small $n_{\rm max}$ the gradient is very large and there is only one solution close to the origin. As $n_{\rm max}$ is increased the gradient is reduced and the straight line just grazes the curve at a critical value of $n_{\rm max}$ at which there are now two solutions. Increasing $n_{\rm max}$ further, there is then a range of values of $n_{\rm max}$ for which there are three solutions. Finally, for large $n_{\rm max}$ there is only one solution again. When three solutions exist for certain values of $n_{\rm max}$, the system becomes bistable and a plot of the input intensity (proportional to $n_{\rm max}$) versus the output intensity (proportional to $n_{\rm ph}$) has the classic s-shaped form shown in Fig. 4.7. This picture suggests a convenient way to determine the conditions for bistability because the two points where the curve turns over delimit the bistable region. These points satisfy $\partial n_{\rm max}/\partial n_{\rm ph} = 0$, giving

$$\kappa^2 + (\Delta_c - NU_0 f)^2 - 2n_{\rm ph}\,(\Delta_c - NU_0 f)\,NU_0 \frac{\partial f}{\partial n_{\rm ph}} = 0. \tag{4.25}$$

This equation can be solved numerically for $n_{\rm ph}$ for different values of Δ_c, assuming that κ, N, and

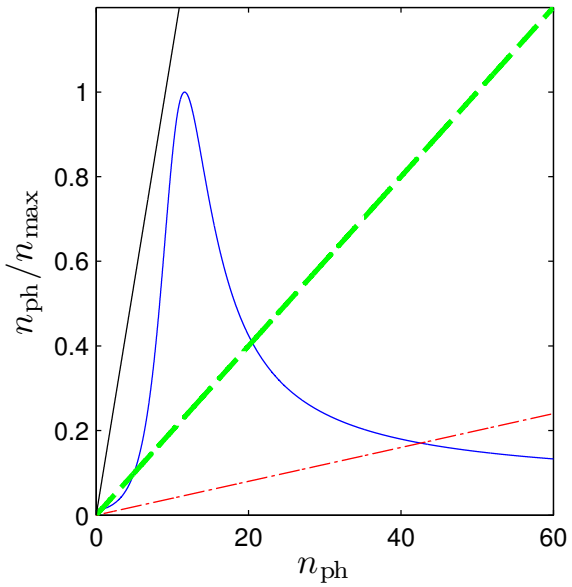

Figure 4.6. A graphical solution of the self-consistency equation in the form (4.23). The blue curve represents the right hand side of Eq. (4.23) for typical values of the cavity parameters ($q = 0$). The red dash-dotted, green dashed and black straight lines represent the left hand side of the equation plotted for different values of $n_{\rm max}$; they intersect the blue curve at one, three, and one points, respectively. The blue curve tends to a finite value at $n_{\rm ph} = 0$ which is set by the fact that for $n_{\rm ph} = 0$ we have $f = 1/2$.

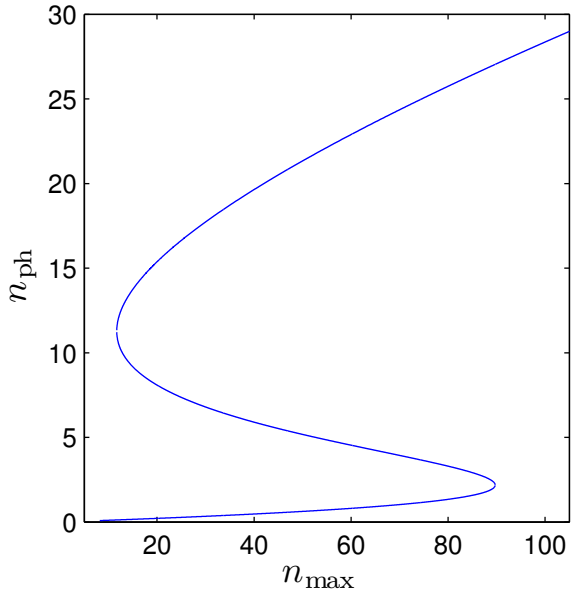

Figure 4.7. Input intensity vs output intensity for a bistable cavity system. In this example the atomic wave function in the cavity is in the $q = 0$ state and $\kappa = 350\omega_{\rm R}$, $\Delta_c = 1500\omega_{\rm R}$, and $U_0 = \omega_{\rm R}$. The points where the curve folds over are given by the solution of Eq. (4.25).

U_0 are fixed. As expected from Fig. 4.7 (see also Fig. 4.14), depending on the value of Δ_c, there are either zero, one, or two values of $n_{\rm ph}$ that satisfy Eq. (4.25). For large values of Δ_c there are no solutions. As $\Delta_{\rm c}$ is reduced, a single solution for $n_{\rm ph}$ suddenly appears at $\Delta_{\rm c} = \Delta_0$, which, by substituting this value of $n_{\rm ph}$ into the self-consistency equation (4.23), gives us $\eta_{\rm cr}(q)$. Reducing Δ_c further, this single solution immediately branches into two solutions for $n_{\rm ph}$. Referring to Fig. 4.7, we see that these two solutions for $n_{\rm ph}$ define a range of values of $n_{\rm max}$, and hence also of η, where bistability occurs. We can find this range of values of η by inserting the two solutions for $n_{\rm ph}$ into the self-consistency equation to give us η_1 and η_2. When $\eta_1 < \eta < \eta_2$ bistability occurs. Note that the values of $\eta_{\rm cr}(q)$, η_1, and η_2, all depend on the state of the atomic wave function and hence are different for different quasi-momenta. This dependence on quasi-momentum is what lies behind the existence of loops in the band structure.

4.6.2 Critical pump strength in shallow lattices

In the regime of shallow lattices, the bistability condition given by Eq. (4.25) can be solved analytically. First consider the critical pump strength of the $q = 0$ case, for which we use the notation $\eta_{\rm cr}(q = 0) \equiv \eta_0$. As described in [6], and as can be seen from Fig. 4.5, for small lattice depths we can linearize the atom-light overlap integral as

$$f(U_0 n_{\rm ph}, q = 0) = \frac{1}{2} - \frac{U_0 n_{\rm ph}}{16}. \tag{4.26}$$

Substituting this into the self-consistency equation (4.9), we obtain a cubic equation in $n_{\rm ph}$, which is reminiscent of the classical Kerr nonlinearity in a medium with an intensity dependent refractive index [4] (note that when we come to numerically solve Eq. (4.25) below in this section and in the rest of the paper, we are going beyond the classical Kerr effect). The condition (4.25) for bistability in this limit then reduces to the solution of a quadratic equation in $n_{\rm ph}$,

$$3n_{\rm ph}^2 N^2 U_0^2 - 32 n_{\rm ph} N U_0^2 (N U_0 - 2\Delta_c) + 64((N U_0 - 2\Delta_c)^2 + 4\kappa^2) = 0. \tag{4.27}$$

The vanishing of the discriminant of the above equation requires that $\Delta_0 = NU_0/2 - \sqrt{3}\kappa$, $\eta_0 = \sqrt{\frac{8\kappa^3}{3\sqrt{3}NU_0^2}}$, and $n_0 = \frac{NU_0^2\sqrt{3}}{64\kappa}$. In the last expression, n_0 is the number of photons in the cavity at the critical point $\Delta_c = \Delta_0$.

4.6.3 Critical pump strength as a function of quasi-momentum

We now extend the above analysis for shallow lattices to include non-zero quasi-momentum. Expanding the atomic Bloch state in a Fourier series, and assuming shallow lattice depths, we can

truncate the series after three terms

$$\psi_q(x, n_{\rm ph}, t) = e^{iqx}(c_0(t) + c_1(t)e^{i2x} + c_2(t)e^{-i2x}). \tag{4.28}$$

In this state one can explicitly calculate $\langle \cos^2(x) \rangle$ as

$$\langle \cos^2(x) \rangle = \frac{1}{2} + \frac{1}{2}(\mathrm{Re}\, c_0 c_2^* + \mathrm{Re}\, c_0 c_1^*) \equiv \frac{1}{2} + \frac{1}{2}(X(t) + Y(t)). \tag{4.29}$$

Rewriting the equations of motion (4.4) and (4.5) for the newly defined variables one finds

$$\begin{aligned}
\frac{\mathrm{d}^2 X}{\mathrm{d}t^2} + (4q+4)^2 X + (q+1)U_0 \alpha^* \alpha |c_0|^2 = 0, \\
\frac{\mathrm{d}^2 Y}{\mathrm{d}t^2} + (4q-4)^2 Y - (q-1)U_0 \alpha^* \alpha |c_0|^2 = 0, \\
\frac{\mathrm{d}\alpha}{\mathrm{d}t} = \left(i\Delta_c - i\frac{NU_0}{2} - i\frac{NU_0}{2}(X+Y) - \kappa \right) \alpha + \eta.
\end{aligned}$$

The atomic state has therefore been mapped onto two coupled oscillators X and Y. The oscillators are not coupled to each other directly, but do interact through the light field α which acts as a driving term for both of them. The above equations resemble Eqns (3) and (4) of [6], and introduce an analogy to optomechanics [46]. Solving these equations at steady state gives

$$\begin{aligned}
\alpha = \frac{\eta}{\kappa - i(\tilde{\Delta}_{\rm c} - NU_0/2(X+Y))}, \\
(4q+4)^2 X + \frac{(q+1)U_0\eta^2}{\kappa^2 + \left(\tilde{\Delta}_{\rm c} - NU_0/2(X+Y)\right)^2}|c_0|^2 = 0, \\
(4q-4)^2 Y - \frac{(q-1)U_0\eta^2}{\kappa^2 + \left(\tilde{\Delta}_{\rm c} - NU_0/2(X+Y)\right)^2}|c_0|^2 = 0,
\end{aligned}$$

where $\tilde{\Delta}_{\rm c} = \Delta_c - NU_0/2$. Combining the steady state solutions into a single equation for the variable $p = X + Y$, and assuming $|c_0|^2 \approx 1$ gives

$$p = \frac{\bar{n}_{\rm max}}{1 + \left(\frac{\Delta_{\rm c}}{\kappa} - \frac{NU_0}{2\kappa} - \frac{NU_0 p}{2\kappa} \right)^2}, \tag{4.30}$$

where $\bar{n}_{\rm max} = \frac{U_0\eta^2}{8(q^2-1)\kappa^2}$. Comparing Eqns (4.30) and (4.23) in the limit when $f = 1/2 - U_0 n_{\rm ph}/16$, we finally obtain an expression for the critical pump strength above which bistability occurs as a function of q

$$\eta_{\rm cr}(q) = \sqrt{\frac{8\kappa^3(1-q^2)}{3\sqrt{3}NU_0^2}} \tag{4.31}$$

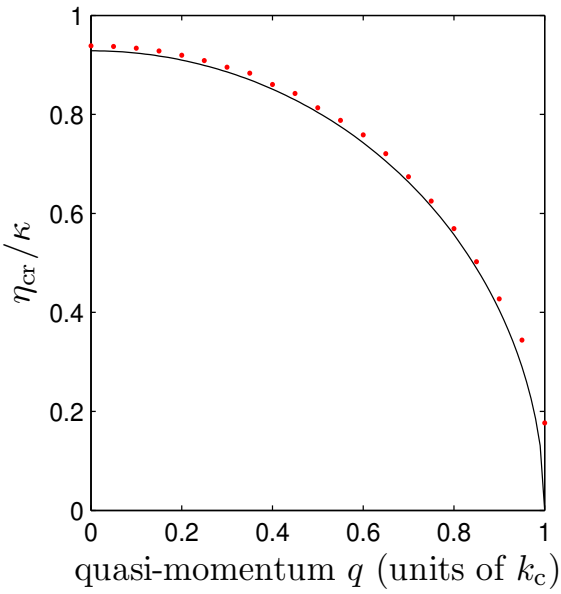

Figure 4.8. Comparison between exact numerical calculation (dots) and analytical estimate (line) for the critical pump strength $\eta_{\rm cr}$ at which loops appear as a function of the quasi-momentum. The values of the parameters are $U_0 = \omega_R$, $N = 10^4$, and $\kappa = 350\,\omega_R$. The analytical estimate is from Eq. (4.31) which is accurate for small lattice depths. Note that the agreement is good for quasi-momentum close to $q = 0$.

where we remind the reader that the frequencies in this expression are in units of the recoil frequency ω_R. This estimate for $\eta_{\rm cr}(q)$ is compared to the full numerical solution of Eq. (4.25) in Fig. 4.8. The parameters are such that the maximum intracavity depth is only of the order of one atomic recoil energy $E_{\rm R}$, and hence the approximation agrees well with the numerical calculation. The agreement deteriorates as $q \to 1$. This is due to the fact that the above two mode approximation fails at $q = 1$ because the coefficient c_0 in Eq. (4.28) is equal to zero at the edge of the Brillouin zone. [1]

Let us now connect the above results to the phenomenon of loops in the band structure. Because $\eta_{\rm cr}$, and also η_1, and η_2 depend on the value of q, as we vary q we expect that the conditions required to have bistability won't necessarily be met over the entire Brillouin zone. That is, as q is varied, η may no longer lie in the range $\eta_1(q) < \eta < \eta_2(q)$. In that case, we expect any additional solutions to form closed loops extending only over part of the Brillouin zone, rather than entire bands covering the whole Brillouin zone. The dependence of $\eta_{\rm cr}$ upon q given by Eq. (4.31) suggests that for shallow lattices the loops will form first at the edge of the Brillouin zone and then propagate inwards as η is increased. Looking back at Fig. 4.1, which shows the energy plotted as a function of quasi-momentum at a fixed value of η and Δ_c, we see a loop centered at $q = 0$, but which does not extend out to $q = 1$, in apparent contradiction to what is predicted by Eq. (4.31). This is because the lattice in Fig. 4.1 is too deep for Eq. (4.31) to apply. In the next section we shall examine how loops appear

[1] This line was erroneously published and should read- *This is due to the fact that the above two mode approximation fails at $q = 1$ because the coefficient $c_0 \approx c_2$ in Eq. (4.28) is equal to $1/2$ at the edge of the Brillouin zone.*

and disappear and, in particular, we will see that loops are indeed born at the edges of the Brillouin zone.

4.7 The birth and death of loops

In this Section we examine how loops appear and disappear in the band structure as the detuning and pumping are varied. We have already seen in Sections 4.4 and 4.5 how multiple solutions and swallowtail loops develop as the detuning from the cavity resonance is varied, but this was for fixed quasi-momentum q. Here we include the quasi-momentum dependence. In Fig. 4.9 we plot the evolution of the loop structures that appear in the band structure as Δ_c is varied. The detuning increases from the top to the bottom panel. In the plots, the pump strength is fixed at $\eta = 2.8\eta_0$ and we see that for small detunings, when bistability initially sets in, swallowtail shaped loops appear at the outer edges of the Brillouin zone. As the detuning is increased the swallowtail loops from the two edges move closer and merge. Initially, the merged loop lies partly below the lowest band, but as the detuning is further increased it moves up and separates from the lowest band. The loop then shrinks in size and vanishes.

One important point to notice is that the swallowtail loop in plot (b) of Fig. 4.9 is qualitatively different from the ones obtained in [18, 17] for an interacting BEC in an optical lattice because in our case the energy dispersion continues to have zero slope at the band edge even when the loops have been formed. The nonlinearity in [18, 17], which is due to interatomic interactions, has quite a different form to that considered here. For example, the nonlinearity arising from interactions is spatially dependent due to the variation in density of a BEC in an optical lattice, whereas the nonlinearity considered here does not have a spatial dependence because it appears under an integral over space, see Eq. (4.7).

In Fig. 4.10 we plot the same thing as Fig. 4.9, except that we have reversed the sign of the atom-light coupling U_0 so that it is negative. Experimentally, this is the case when $\Delta_a < 0$, i.e. the pump laser is red detuned from the atomic resonance. Note that the effect of the sign flip upon the potential term $U_0 n_{\rm ph} \cos^2(x)$ occuring in the atomic Schrödinger equation is equivalent to a spatial translation of $\pi/2$. This transforms the atom-light overlap integral (4.7) as

$$\langle \cos^2(x) \rangle \to 1 - \langle \cos^2(x) \rangle \tag{4.32}$$

where the left hand side refers to the $U_0 < 0$ case, and the right hand side to the $U_0 > 0$ case. The self-consistency equation therefore becomes

$$n_{\rm ph} = \frac{\eta^2}{\kappa^2 + \left(\Delta_c + N|U_0| - N|U_0| f(|U_0| n_{\rm ph}, q)\right)^2} \ . \tag{4.33}$$

Figure 4.11 plots the evolution of the band structure as the external laser pumping η is varied,

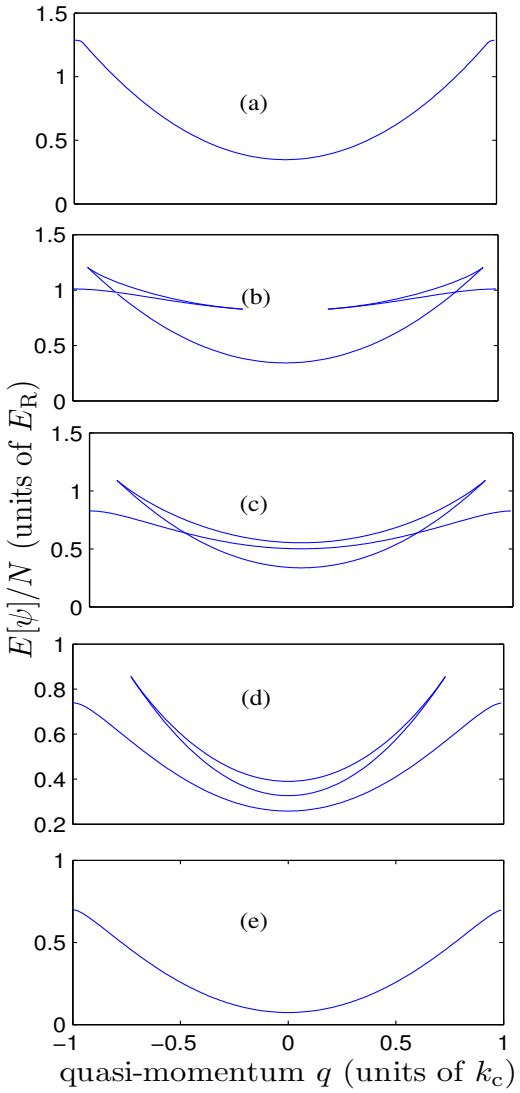

Figure 4.9. The birth and death of band structure loops as the laser-cavity detuning Δ_c is varied, for the case when the laser is blue-detuned from atomic resonance ($\Delta_a > 0$). Δ_c increases as one goes from (a) to (e) as follows: $1500\,\omega_{\rm R}$, $2100\,\omega_{\rm R}$, $2600\,\omega_{\rm R}$, $3100\,\omega_{\rm R}$ and $3600\,\omega_{\rm R}$. The rest of the parameters are $\kappa = 350\,\omega_{\rm R}$, $U_0 = \omega_{\rm R}$, $N = 10^4$, $\eta = 2.8\,\eta_0$ and $\eta_0 = 325\,\omega_{\rm R}$.

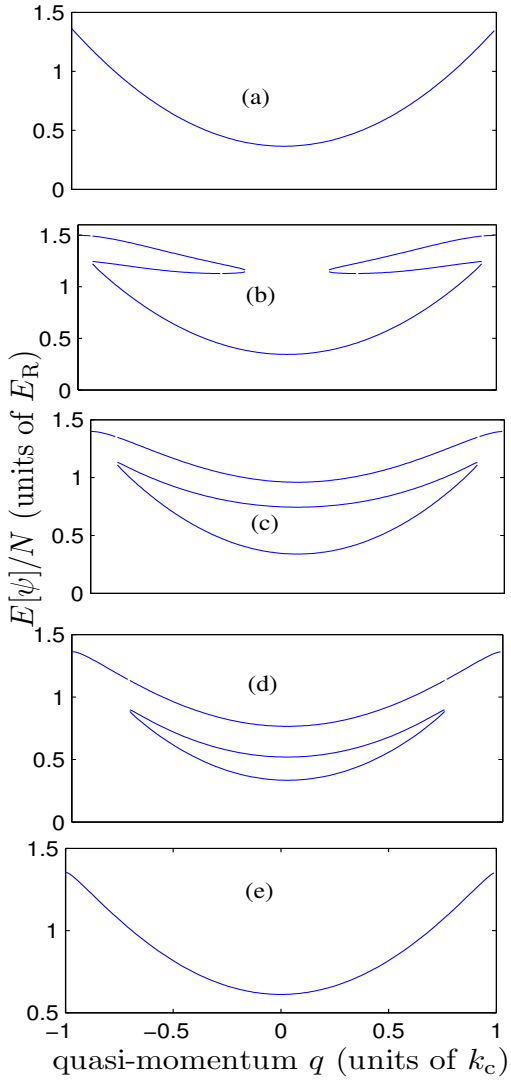

Figure 4.10. The birth and death of band structure loops as the laser-cavity detuning Δ_c is varied, for the case when the laser is red-detuned from atomic resonance ($\Delta_a < 0$). Δ_c increases as one goes from (a) to (e) as follows: $-8500\,\omega_{\rm R}$, $-7900\,\omega_{\rm R}$, $-7400\,\omega_{\rm R}$, $-6900\,\omega_{\rm R}$ and $-6400\,\omega_{\rm R}$. The rest of the parameters are $\kappa = 350\,\omega_{\rm R}$, $U_0 = -\omega_{\rm R}$, $N = 10^4$, $\eta = 2.8\,\eta_0$ and $\eta_0 = 325\,\omega_{\rm R}$.

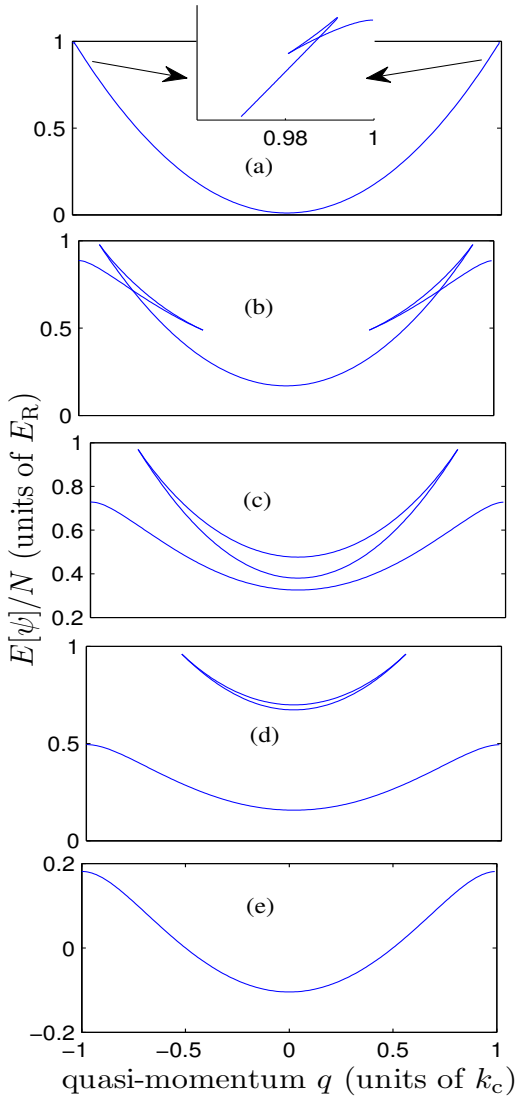

Figure 4.11. The birth and death of band structure loops as the pumping rate η is varied. In this figure the detuning is held constant at $\Delta_c = 2900\,\omega_R$. The value of η increases from (a) to (e) as follows: $0.5\eta_0, 2\eta_0, 3\eta_0, 4\eta_0, 5\eta_0$, where $\eta_0 = 325\,\omega_R$ as usual. The inset shows a zoom-in for $\eta = 0.5\,\eta_0$, illustrating that as η is increased, the loops are born at the edges of the Brillouin zone.

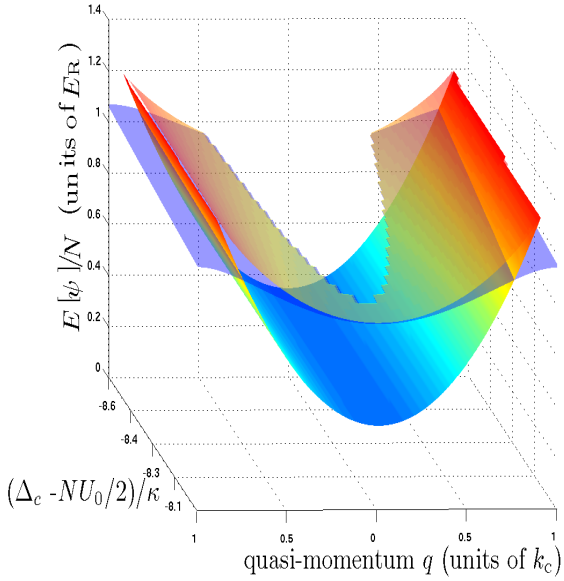

Figure 4.12. Energy as a function of quasi-momentum q and detuning Δ_c. At smaller values of Δ_c, the swallowtail loops occur in pairs close to the edges of the Brillouin zone at $q = \pm 1$, and as the detuning is increased they propagate inwards and merge as shown in this plot. Δ_c increases out of the page. Parameters are $\kappa = 350\,\omega_R$, $U_0 = \omega_R$, $N = 10^4$, $\eta = 2.8\,\eta_0$, and $\eta_0 = 325\,\omega_R$.

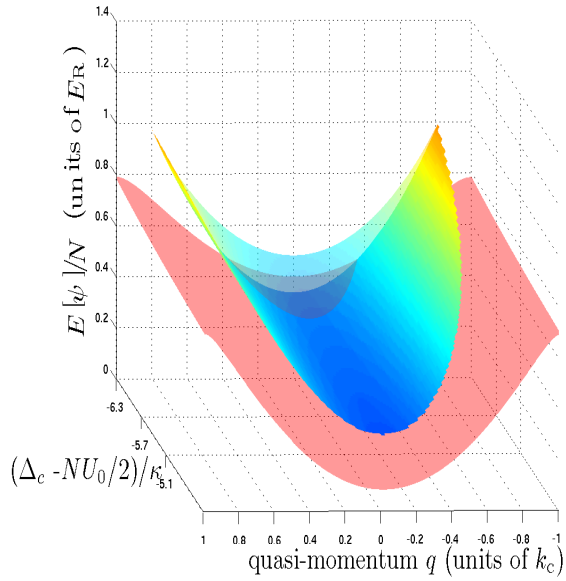

Figure 4.13. Energy as a function of quasi-momentum q and detuning Δ_c. Δ_c increases out of the page. For larger values of Δ_c, the band center loops move up in energy and do not touch the lower band (shaded red in the plot). Eventually, for still higher values of detuning, they shrink and disappear as shown in this plot. Parameters are $\kappa = 350\,\omega_R$, $U_0 = \omega_R$, $N = 10^4$, $\eta = 2.8\,\eta_0$, and $\eta_0 = 325\,\omega_R$.

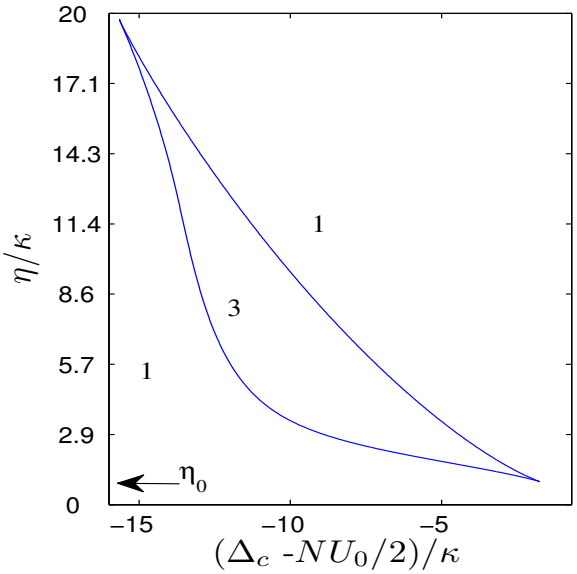

Figure 4.14. Bifurcation structure of the solutions to the self-consistency equation Eq. (4.9) in the $\{\eta, \Delta_c\}$ plane with $q = 0$, $U_0 = \omega_{\rm R}$, $\kappa = 350\,\omega_{\rm R}$, $N = 10^4$. The numbers on the plot indicate the number of solutions that exist for the steady state photon number in the cavity. The critical value of the pumping $\eta_0 = \eta_{\rm cr}(q = 0)$ for bistability for these parameters is indicated by the arrow. Inside the crescent shaped region the system supports three solutions (one unstable), i.e. it is bistable.

for fixed detuning Δ_c. We see that as η increased the loops first appear as swallowtails at the edges of the Brillouin zone (see inset in Fig. 4.11a), in agreement with the predictions of Eq. (4.31).

Figures 4.12 and 4.13 are both 3D plots of the loops as functions of Δ_c and q, but each one covers a different range of Δ_c. In the first plot the merging of the swallowtail loops into the band center loops is shown. In the second plot, as Δ_c increases the band center loops move upwards in energy and separate from the ground band, shrink in size and eventually disappear.

As will be demonstrated in the next section, in certain parameter regimes the spectrum may qualitatively change compared to the above. In particular, we show that for some $q \neq 0$, and for sufficiently larger pump strength η, we can achieve tristability. Moreover, we show how this multistable behaviour can be understood in terms of catastrophe theory.

4.8 Tristability

Thus far we have seen that there are regions of the parameter space $\{\Delta_c, \eta, q, U_0\}$ where the self-consistency equation (4.9) applied to the first band admits either one or three solutions. In the latter case we have bistability. It is natural to ask whether there are other regions of parameter space where even more simultaneous solutions can occur? A recent paper discussing two-component BECs in a cavity has found regions of parameter space that support tristability [47] and in this section we want

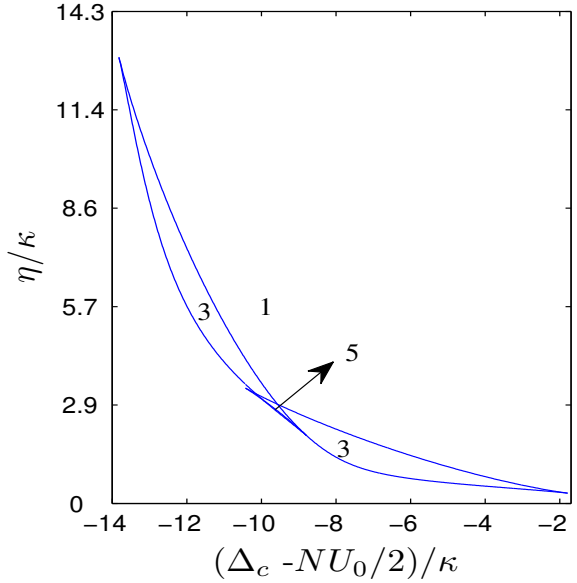

Figure 4.15. Bifurcation structure of the solutions to the self-consistency equation Eq. (4.9) in the $\{\eta, \Delta_c\}$ plane with $q = 0.95$, $U_0 = \omega_{\rm R}$, $\kappa = 350\,\omega_{\rm R}, N = 10^4$. The numbers on the plot indicate the number of solutions that exist for the steady state photon number in the cavity. Inside the swallowtail shaped curve there are five solutions and hence multistability, see Fig. 4.16.

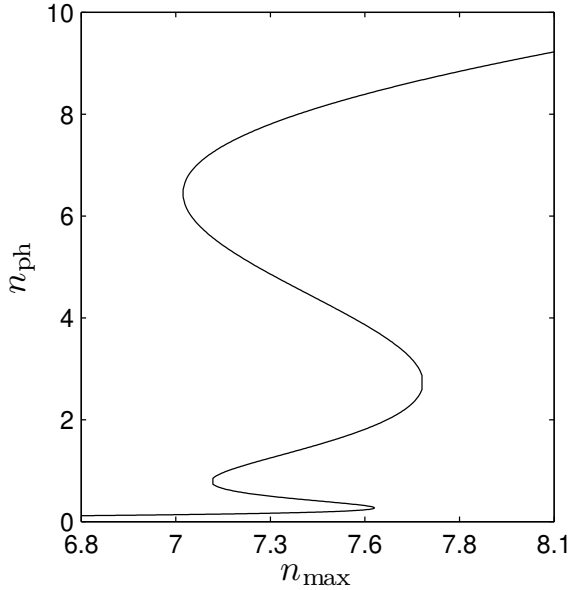

Figure 4.16. Plot of multistable steady state photon number $n_{\rm ph}$ versus $n_{\rm max}$ (equal to η^2/κ^2) for $\Delta_c = 1630\,\omega_{\rm R}$ and $q = 0.95$, $U_0 = \omega_{\rm R}$, $\kappa = 350\,\omega_{\rm R}, N = 10^4$. The Δ_c value is chosen from the region which supports five solutions in Fig. 4.15.

to examine whether tristability is possible in the ordinary one-component case but with finite values of the quasi-momentum.

In Fig. 4.14 we show the region of $\{\Delta_c, \eta\}$ space where bistability occurs. This plot is for fixed values of U_0 and q. In particular, for $q = 0$ we at most find bistability. The crescent shape in Fig. 4.14 demarks the region with three solutions: the number of solutions changes by two as one crosses its boundary. The location of η_0, the smallest pump strength for which bistability occurs when $q = 0$, is indicated by an arrow on the vertical axis in order to make contact with the discussion of Sec. 4.5. However, when we allow non-zero values of q we find that we can indeed have regions of tristability, due to the presence of five solutions, which occur inside the swallowtail shaped region in Fig. 4.15, which is plotted for $q = 0.95$. Fig. 4.16 plots the corresponding photon number versus laser pumping curve for a fixed value of Δ_c, and illustrates how, as the laser pumping strength is changed, the system goes from one solution, to three solutions, to five solutions, back to three solutions and finally back to one solution again. This curve is calculated for a vertical slice through the parameter space shown in Fig. 4.15. We give an example of the band structure when there is tristability in Fig. 4.17.

So far we have conducted a rather ad hoc exploration of the four-dimensional parameter space given by $\{\Delta_c, \eta, q, U_0\}$. Furthermore, in the two-dimensional slices shown in Figures 4.14 and 4.15 we have glimpsed snap shots of a rather complex looking structure of solutions. We are therefore led to ask whether there is any order in this complexity? Are the geometric structures seen in the plots random, or is there in fact an underlying structure that organizes them? In order to make progress with understanding multistability it would be useful to have a more systematic framework for analyzing our solutions and just such a framework is provided by catastrophe theory, which we now discuss. As will become clear, the structures we see in parameter space are not only generic, but are organized in a very particular, and therefore predictable, way.

4.9 Catastrophe theory analysis

4.9.1 Overview of catastrophe theory

Catastrophe theory is a branch of bifurcation theory that concerns the study of singularities of gradient maps [35, 37]. Examples of gradient maps abound in physics, for example Hamilton's principle of least action in mechanics, and Fermat's principle of least time in optics. In both theories the physical paths (rays) are given by the stationary points of a generating function $\Phi(\mathbf{s}; \mathbf{C})$, which in mechanics is the action and in optics is the optical distance. In both cases the gradient map is obtained from a variational principle that takes the form

$$\frac{\partial \Phi(\mathbf{s}; \mathbf{C})}{\partial s} = 0 \ . \tag{4.34}$$

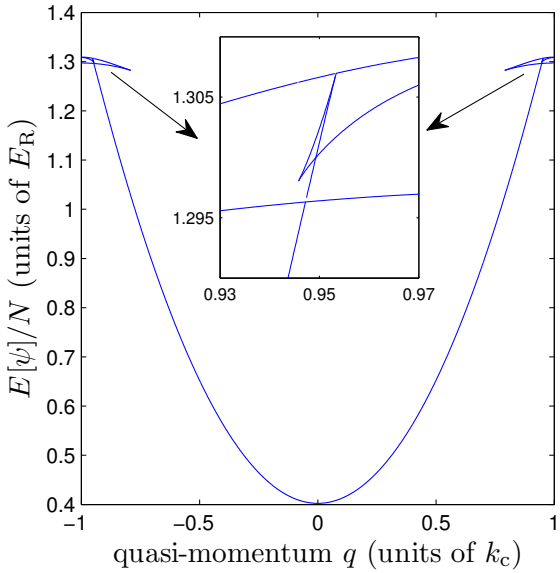

Figure 4.17. Plot of tristable band structure. The parameters are given by $\eta = 980\,\omega_R$, $\Delta_c = 1640\,\omega_R$, $\kappa = 350\,\omega_R$, $N = 10^4$, and $U_0 = \omega_R$.

In catastrophe theory, this equation is sometimes referred to as the *state equation*, the generating function $\Phi(\mathbf{s};\mathbf{C})$ is called the *potential function* and the variables appearing in the potential function are considered to be of two basic types: the *state variables* $\mathbf{s} = \{s_1, s_2, s_3 \ldots\}$ and the *control parameters* $\mathbf{C} = \{C_1, C_2, C_3 \ldots\}$. The state variables parameterize all possible paths (not just the paths corresponding to the stationary points) and the control parameters determine the conditions imposed on the paths. For example, if we are interested in the path(s) which pass through the point $\{X, Y, Z\}$ in three dimensional space, then the coordinates $\{X, Y, Z\}$ form the control parameters. For a fixed set of control parameters, the potential function defines the height of a landscape with coordinates $\mathbf{s}$. The classical paths (rays) are then the stationary points $\mathbf{s^i}$ (labelled by the index i if there are more than one) of this landscape, namely the mountain peaks, valley bottoms and saddles [35].

The gradient map becomes singular when there is more than one stationary point for a given set of control parameters. In optics this is the phenomenon of focusing, because more than one ray passes through the same physical point $\mathbf{C} = \{X, Y, Z\}$, leading to a caustic. The caustic, or catastrophe, as it is known in catastrophe theory, lives in control space, which in the standard optics case is physical 3-dimensional space. As $\mathbf{C}$ is varied one can explore the structure of the caustic. This is what was shown above in Figures 4.14 and 4.15, which are two dimensional slices through the parameter space $\{\Delta_c, \eta, q, U_0\}$. The crescent and swallowtail shapes are the catastrophes, whose full structure only becomes apparent when viewed in four-dimensional parameter space.

Catastrophes are points, lines, surfaces, and hypersurfaces in control space across which the

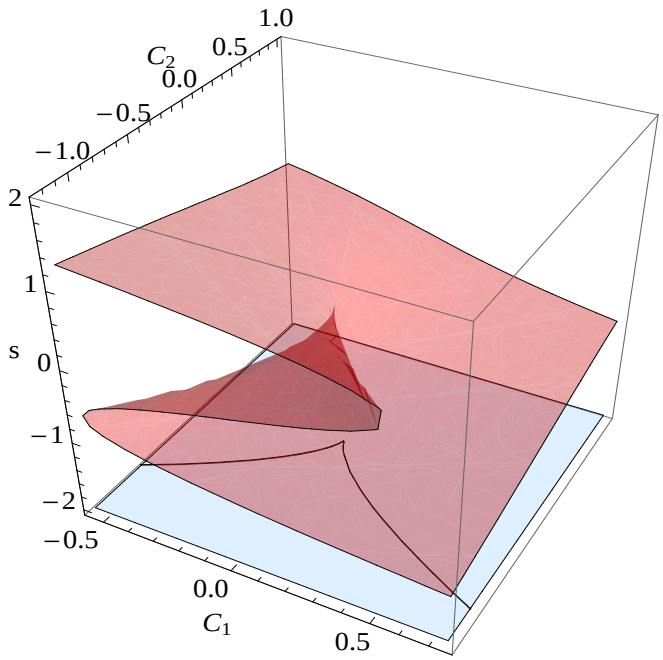

Figure 4.18. The cusp catastrophe is generated by the quartic potential function Φ given in Table 4.1, which can be viewed as representing a double-well potential. The red folded-over surface plotted in this figure obeys the cubic state equation $\partial\Phi/\partial s = s^3 + C_2 s + C_1 = 0$, which gives the stationary solutions s^i of Φ. When $C_2 < 0$ there can be up to three stationary points, s^1, s^2 and s^3, for each value of C_1 and C_2. These points are the two minima and single maximum of the double-well potential. When $C_2 > 0$ there is only one stationary point s corresponding to the minimum of a single well. A vertical slice through the figure such that $C_1 = 0$ gives a pitchfork bifurcation. The $\{C_1, C_2\}$ plane forms the two dimensional control space where the cusp catastrophe itself lives, and this is shown at the bottom of the figure. The cusp catastrophe is formed of two fold curves joined at a singular cusp point. The cusp catastrophe demarks the region of control space that sustains three solutions for s, and so it is given by the projection of the folded-over part of the state surface onto the $\{C_1, C_2\}$ plane. Crossing the fold lines from inside the cusp to outside it, two of the solutions (the maximum and one of the minima) annihilate. Mathematically, this is described by the potential function being stationary to the next higher order [35], i.e. $\partial^2\Phi/\partial s^2 = 3s^2 + C_2 = 0$. Eliminating s by combining this equation with the state equation gives the equation for the cusp catastrophe as $C_1 = \pm\sqrt{-16C_2^3/27}$. Right at the cusp point itself, which is given by the control space coordinates $C_1 = C_2 = 0$, all three stationary points coalesce simultaneously to leave a single solution.

number of solutions to the problem changes. Catastrophe theory classifies these catastrophes in terms of their codimension K, which is the difference between the dimension of the control space and the dimension of the catastrophe. For example, if we consider the two dimensional space shown in Figures 4.14 and 4.15, we find "fold" curves ($K = 1$) and "cusp" points ($K = 2$). If we add a third dimension then we would find fold surfaces ($K = 1$), cusp edges ($K = 2$), and "swallowtail" points ($K = 3$).

In order to make the foregoing discussion more concrete, consider the structure shown in Fig. 4.18 which illustrates the cusp catastrophe. The surface shown in the figure is the state surface $\partial\Phi/\partial s = 0$ plotted in a composite of control and state space. The control space is two dimensional and is given by the C_1, C_2 plane at the bottom of the figure. As listed in Table 4.1, the cusp catastrophe is described by a quartic potential function which, by varying the control parameters C_1 and C_2, can be tuned between being a double or a single well potential. A prominent physical example of such quartic potential function is the thermodynamic potential in Landau's phenomenological theory for continuous phase transitions [48]

$$\Phi(s; P, T, h) = \Phi_0 + Bs^4 + As^2 + hs. \tag{4.35}$$

The order parameter s for the phase transition can be identified as the state variable. The parameter h describes an external field, and A and B are functions of pressure P and temperature T. At first sight, it appears as though the Landau potential function contains three control parameters, and so does not correspond to the cusp catastrophe. However, it is easy to see that one of the parameters is redundant because the state equation can be written in terms of only two control parameters: $C_1 = h/B$ and $C_2 = A/B$. The Landau thermodynamic potential can therefore be seen to correspond to the cusp potential function.

In the present case of ultracold atoms in an optical cavity, the potential function is the reduced hamiltonian (4.13), the state variable is the wave function ψ, and the control parameters are $\{\Delta_c, \eta, q, U_0\}$. We assume that the cavity decay rate κ and number of atoms N are constants that are unchanged throughout the analysis. The stationary Schrödinger equation, obtained from the time-dependent Schrödinger equation (4.10), is therefore the state equation which determines the allowed classical "paths" (rays) ψ. However, because we are interested here in solutions of the Bloch wave form, our "paths" ψ are Mathieu functions labelled by the quasi-momentum and the depth of the optical lattice. The quasi-momentum q is one of the control parameters, but the depth of the optical lattice is determined uniquely, via the self-consistency equation (4.9), by the number of photons in the cavity $n_{\rm ph}$. Therefore, we can choose to work with $n_{\rm ph}$ rather than ψ as already discussed in Section 4.4.2. The state equation which determines its stationary values is the self-consistency equation (4.9).

The purpose of formulating our problem in terms of catastrophe theory is that we can now take advantage of a very powerful theorem [33]. This states that there are only a strictly limited number of

Table 4.1. Standard forms of the cuspoid catastrophes

Name	$\Phi(s;C)$	K
Fold	$s^3/3 + Cs$	1
Cusp	$s^4/4 + C_2 s^2/2 + C_1 s$	2
Swallowtail	$s^5/5 + C_3 s^3/3 + C_2 s^2/2 + C_1 s$	3
Butterfly	$s^6/6 + C_4 s^4/4 + C_3 s^3/3 + C_2 s^2/2 + C_1 s$	4

different forms which the potential function $\Phi(\mathbf{s};\mathbf{C})$ can take in the neighbourhood of a catastrophe. The first four are listed in Table 4.1. Note that each of the standard forms is a polynomial in s, but is linear in the control parameters. In fact, for control spaces of dimension four or less there are only seven distinct structurally stable potential functions. Three of these require two state variables, whereas we only require one state variable, so that leaves the four so-called *cuspoid* catastrophes, which are the ones listed in Table 4.1.

This remarkable result allows us to predict, at least qualitatively, the structures seen in Figures 4.14 and 4.15 given only very rudimentary information such as the number of control parameters. However, the sting in the tail is that it is rare for the potential function that appears in any particular problem to already be in one of the standard forms shown in Table 4.1. Rather, it is generally necessary to perform various transformations upon the variables in order to manipulate the raw potential function into one of the standard forms. We already saw this for the rather simple case of the Landau theory discussed above, and we shall see below that this is also true for the problem of multistability in atom-cavity systems.

From Table 4.1, we see that the butterfly potential function is the only one which gives up to five stationary solutions and has a four dimensional control space. We can therefore immediately say that our problem corresponds at least to a butterfly catastrophe because we have already found parameter regimes which give five solutions. This does not rule out the possibility of a higher catastrophe (the higher catastrophes contain the lower ones, as can be seen in Fig. 4.18 for the case of the cusp and the fold), but until we find regimes with a higher number of solutions (and, indeed, we have not) we shall work with the hypothesis that we are dealing with a butterfly catastrophe. We might therefore expect to find a very special point in parameter space where all five solutions merge into one (the "butterfly point"). However, this requires us to be able to maneuver through parameter space in order to find this point. The delicate issue of whether the four experimental parameters $\{\Delta_c, \eta, q, U_0\}$ can be transformed into the butterfly's four linearly independent control parameters $\{C_1, C_2, C_3, C_4\}$, and so allow us to fully explore the butterfly catastrophe, will be studied in Section 4.9.3 below. First, we begin with the simpler case of shallow lattices.

4.9.2 Application of catastrophe theory to shallow lattices

The starting point for our analysis will not be the potential function Φ, which in our case is the energy functional (4.13) that explicitly depends on the atomic wave function $\psi_q(x, n_{\rm ph})$ and implicitly on

the photon number $n_{\rm ph}$. Instead, we begin one step further along with the state equation which, as explained above, is provided by the self-consistency equation Eq. (4.9) for the photon number. This was also the approach adopted in [39] in order to tackle bistability in traditional laser systems. The photon numbers that satisfy the state equation for given values of the control parameters form the set of stationary points of the potential function. For our state variable we shall actually choose

$$v \equiv U_0 n_{\rm ph} \ . \tag{4.36}$$

In terms of v the state equation can be written

$$v + v\left(\Delta_c - NU_0 f(v,q)\right)^2 - \eta^2 U_0 = 0. \tag{4.37}$$

where $\langle \cos^2(x) \rangle = f(v,q)$ is evaluated in a Bloch state $\psi_q(x,v)$, and the choice of v as the state variable is motivated by the dependence of the Bloch state on the product $U_0 n_{\rm ph}$, which is the depth of the optical lattice, see Eq. (4.4). In the above equation we have also rescaled all frequencies by κ (i.e. we have divided throughout by κ^2 and set $\kappa = 1$).

Equation (4.37) is not straightforward to analyze because we do not have a closed-form analytical expression for $f(v,q)$. Thus, we find ourselves in the common situation, as mentioned above, that it is not obvious which standard potential function, and hence which standard state equation, corresponds to our problem. However, we have already seen in Sec. 4.5 that when the depth of the optical lattice is small, we can perform a series expansion and obtain an approximate analytical expression for $f(v,q)$. This is the approach we shall follow first and we will take up the general case in the next subsection. Specializing to the case of $q = 0$, we use Eq. (4.26) to write $f(v, q=0) = 1/2 - v/16$, and upon substitution into Eq. (4.37) this gives

$$\begin{aligned} & v^3 + b_1 v^2 + b_2 v + b_3 = 0, \\ & b_1 = \frac{32\Delta_c}{NU_0} - 16, \\ & b_2 = \frac{64\left(4 + (NU_0 - 2\Delta_c)^2\right)}{N^2 U_0^2}, \\ & b_3 = \frac{-256\eta^2}{N^2 U_0^2}. \end{aligned} \tag{4.38}$$

The leading term in the above equation is cubic in the state variable v (similar in that respect to the classical Kerr non-linearity [3, 4]). It is therefore close to, but not yet identical with, the standard form of the state equation for a cusp

$$s^3 + C_2 s + C_1 = 0. \tag{4.39}$$

Complete equivalence to the cusp can be achieved by removing the quadratic term from (4.38) via

the transformation $s = v + b_1/3$, leading to the following values for C_2 and C_1

$$C_2 = b_2 - \frac{1}{3}b_1^2, \tag{4.40}$$

$$C_1 = b_3 - \frac{1}{3}b_1 b_2 + \frac{2}{27}b_1^3. \tag{4.41}$$

Thus, we see that the canonical control parameters in the final mapping to the standard form are complicated functions of the physical control parameters η, Δ_c, and U_0.

Let us compare the above prediction to the case illustrated in Fig. 4.14. The figure shows the number of steady state solutions for the photon number in the $\{\eta, \Delta_c\}$ plane, for fixed values of U_0 and q. The figure was calculated for $q = 0$, and the part of it close to the horizontal axis corresponds to low photon number, and so the shallow lattice theory outlined above applies in that region. We indeed find that the first derivative of the state equation vanishes at all points along the curves separating regions with one and three solutions (this is how the curves were computed), which are therefore fold curves, while at the point with $\eta = \eta_0$ we find the second derivative also vanishes, identifying it as a cusp point where all three solutions coalesce into a single solution. We therefore find that catastrophe theory correctly accounts for the structure seen in Fig. 4.14.

A key point to note from the above analysis is that the underlying catastrophe that we identified had only two control parameters even though there were three "experimental" parameters that could be varied in the original statement of the physical problem (we set $q = 0$). We met a similar situation for the Landau theory of continuous phase transitions discussed above. The question then arises, how do we identify the underlying catastrophe in cases where the transformation to standard form is hard to find? One way to proceed is via the defining character of each potential function in Table 4.1, which is the highest derivative that vanishes at the most singular point. For the cusp the most singular point is $s = C_1 = C_2 = 0$ where the first, second, and third derivatives of the potential function with respect to s vanish. We shall take advantage of this defining character in order to tackle the general case of a lattice of arbitrary depth in the next subsection.

It is worth commenting on the role of the extra dimension in control space that was present in the original statement of the shallow lattice problem, as given by Eq. (4.38). It is easy to imagine that, given a basic catastrophe, we can always embed it in a control space of higher dimension without fundamentally changing the catastrophe providing we extend it into the extra dimension in a trivial way. For example, given the cusp catastrophe that has a minimal control space which is two-dimensional, as shown in Fig. 4.18, we can always add a third dimension such that the cusp becomes a structure rather like a tent, with the ridge pole being a cusp edge (a continuous line of cusps). The existence of the line of cusps can be inferred from the shift of variables $s = v + b_1/3$ that was performed: the location of the highest singularity is parameterized by the parameter b_1 which is the extra control parameter.

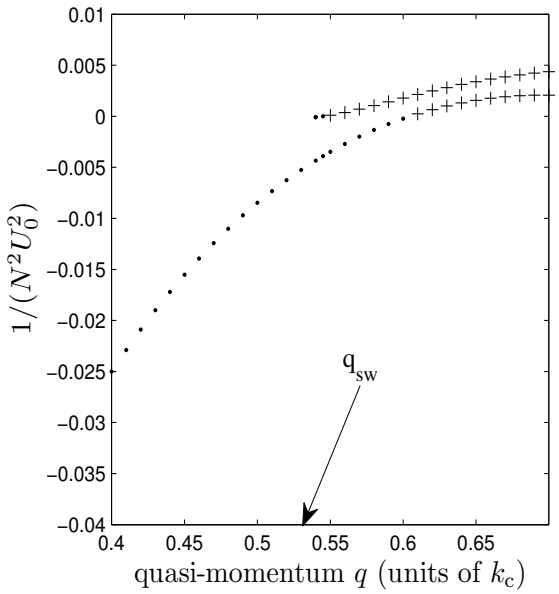

Figure 4.19. A plot showing the values of $1/(NU_0)^2$ obtained from the simultaneous solution of Eqns (4.43)–(4.45) for different values of quasi-momentum. These equations give the first three derivatives of the state equation (4.42), and hence correspond to swallowtail points. Only the crosses satisfy $1/(NU_0)^2 > 0$ and occur only for $q > q_{\rm sw}$.

4.9.3 Application of catastrophe theory to lattices of arbitrary depth

Lifting the restriction of small photon number, we define the notation $\mathcal{G}(v; \Delta_c, \eta, q, U_0)$ for the left hand side of the state equation (4.37)

$$\mathcal{G}(v; \Delta_c, \eta, q, U_0) \equiv v + v\left(\Delta_c - NU_0 f(v, q)\right)^2 - \eta^2 U_0 = 0. \tag{4.42}$$

The fact that we have four experimental parameters holds out the possibility that the above state equation is that of a butterfly catastrophe (see Table 4.1). Furthermore, because we have already discovered regimes with five solutions, we must have at least a butterfly. However, from our experience with the shallow lattice case, we know that we may not be able to fully explore the catastrophe if some of the control parameters are trivial. We shall therefore investigate whether we can find a singular point (the butterfly point) where the fifth and all lower derivatives of the potential function with respect to v simultaneously vanish (i.e. the fourth and lower order derivatives of $\mathcal{G}(v; \Delta_c, \eta, q, U_0)$ simultaneously vanish) and Eq. (4.42) is also satisfied.

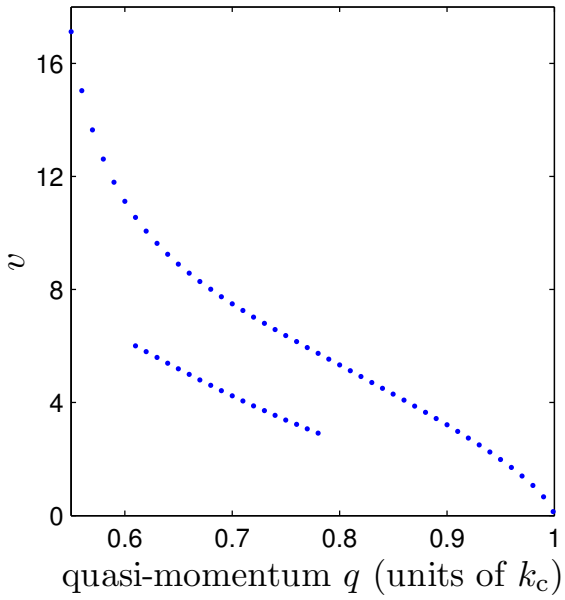

Figure 4.20. A plot showing the values of the state variable $v = U_0 n_{\rm ph}$ for which the first three derivatives of the state function $\mathcal{G}$ vanish simultaneously (swallowtail points). For approximately $0.6 < q < 0.8$ there are two such points for any given q.

Taking the derivatives of Eq. (4.42), and simplifying slightly the resulting equations, we find

$$\left(\frac{\Delta_c}{NU_0} - f\right)^2 - 2vff^i\left(\frac{\Delta_c}{NU_0} - f\right) = \frac{-1}{N^2U_0^2} \tag{4.43}$$

$$\frac{2ff^i + v\left(ff^{ii} + (f^i)^2\right)}{2f^i + vf^{ii}} = \frac{\Delta_c}{NU_0} \tag{4.44}$$

$$\frac{3ff^{ii} + 3(f^i)^2 + v\left(3f^if^{ii} + ff^{iii}\right)}{vf^{iii} + 3f^{ii}} = \frac{\Delta_c}{NU_0} \tag{4.45}$$

$$\frac{12f^if^{ii} + 4ff^{iii} + v\left(4f^if^{iii} + ff^{iv} + 3(f^{ii})^2\right)}{vf^{iv} + 4f^{iii}} = \frac{\Delta_c}{NU_0} \tag{4.46}$$

where the first, second, third, and fourth derivatives of the function $f(v, q)$ with respect to v are denoted by f^i,f^{ii},f^{iii},f^{iv}, respectively. In fact, we have seen Eq. (4.43) before, as it is the same as Eq. (4.25) that we used as a condition for bistability. Our strategy will be to find solutions to Eqns (4.43–4.46) numerically. In order to facilitate this, observe that Eq. (4.44) and Eq. (4.45) can be combined into a single equation:

$$\frac{2ff^i + v\left(ff^{ii} + (f^i)^2\right)}{2f^i + vf^{ii}} - \frac{3ff^{ii} + 3(f^i)^2 + v\left(3f^if^{ii} + ff^{iii}\right)}{vf^{iii} + 3f^{ii}} = 0\ . \tag{4.47}$$

We solve this equation for v at different values of q by numerically finding the zeros of the left hand side. Once we find the zeros for a particular q, we can use Eq. (4.44) to calculate Δ_c/NU_0 at these values. Next, these values of v and Δ_c/NU_0 are used in Eq. (4.43) to calculate $1/(NU_0)^2$. In this last

step we find that we obtain the unphysical result $1/(NU_0)^2 < 0$ unless $q > q_{\rm sw}$, where $q_{\rm sw} = 0.545$ is a certain critical value of the quasi-momentum. This is illustrated in Fig. 4.19 where we plot the values of $1/(NU_0)^2$ computed using the above method for different values of the quasi-momentum q in the neighborhood of $q_{\rm sw}$. Only the crosses satisfy $1/(NU_0)^2 > 0$. We drop the solutions corresponding to the dots, for which $1/(NU_0)^2 < 0$. For $q > q_{\rm sw}$ there are always values of q at which $1/(NU_0)^2 > 0$. Note that $q_{\rm sw} = 0.545$ is a universal result since it does not depend on any other parameter values.

The final step is to check if Eq. (4.46) for the fifth derivative is satisfied at the values of Δ_c, NU_0, and v that we computed using the lower derivatives. We did not find any value of $q > q_{\rm sw}$ where this was the case. The important part of our numerical computation involves the calculation of the derivative of the function $f(v, q)$ for which we do not have an analytical expression. We used the MATLAB® [49] routine DERIVSUITE [50] to calculate the derivatives. This routine also provides errors on the derivatives and we can compound errors and find values for expressions like the left hand side of Eq. (4.47) with error. We use this error as the tolerance in our zero finding. Some more details of this procedure are provided in the Appendix.

The fact that we did not find a point where the four higher derivatives of the function $\mathcal{G}$ simultaneously vanish in the range $0 < q < 1$ (we do not consider negative q because $f(v, q)$ is symmetric under $q \to -q$) means that although the underlying catastrophe that organizes the solutions is at least a butterfly (because we find five solutions), the four experimental parameters at our disposal $\{\Delta_c, \eta, q, U_0\}$ do not translate into four linearly independent coordinates in control space $\{C_1, C_2, C_3, C_4\}$ [51]. We are therefore not able to navigate freely through the four-dimensional control space and locate the butterfly point at $C_1 = C_2 = C_3 = C_4 = 0$. This is the extension into four dimensions of the situation we already found in Section 4.9.2 for shallow lattices.

The identification of places where three derivatives of $\mathcal{G}$ simultaneously vanish means that the highest singularities we have in the parameter space $\{\Delta_c, \eta, q, U_0\}$ are swallowtail points (swallowtails are contained within a greater butterfly catastrophe). In the Appendix we outline a proof that in the neighbourhood of a point where three derivatives of the state equation vanish the potential function must be equivalent to that of a swallowtail catastrophe. Note that these swallowtails occur entirely in control space and are thus true swallow tail catastrophes in the sense of Table 4.1. The swallowtails shown previously in Figures 4.3, 4.9, 4.10, 4.11, 4.12 and 4.13 are not swallowtail catastrophes because these figures show a combination of state and control spaces. By contrast, Figures 4.14, 4.15 and 4.21 are solely in control space. In particular, Fig. 4.21 shows a two- dimensional slice through the three-dimensional swallowtail catastrophe in control space. Unlike Fig. 4.15, this slice includes the swallowtail point, which is the highest singularity on the swallowtail catastrophe, and is the point where four solutions of the state equation (4.42) simultaneously coalesce so that number of solutions changes by 4 (i.e. the point where three derivatives of $\mathcal{G}$ simultaneously vanish). We emphasize that this can only occur when $q > q_{\rm sw}$. We also note from Fig. 4.20 that between $0.6 < q < 0.8$ we find more than one swallowtail point for a given q, which is again an indication of the presence of

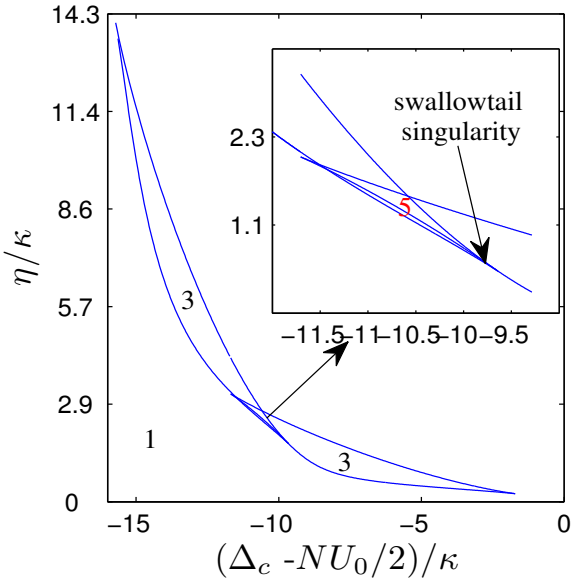

Figure 4.21. Bifurcation structure of the solutions to the self-consistency equation Eq. (4.9) in the $\{\eta, \Delta_c\}$ plane with $q = 0.96$, $U_0 = 1.13\,\omega_{\rm R}$, $\kappa = 350\,\omega_{\rm R}, N = 10^4$, and hence $NU_0/2 = 16.1\kappa$. The numbers on the plot indicate the number of solutions for $n_{\rm ph}$ in that region of the parameter space. The inset shows a swallowtail singularity point where five solutions coalesce into a single solution. The coordinates of the swallowtail point shown in this figure are $v = 0.04$, $\eta = 1.7\kappa$, $\Delta_c = 6.4\kappa$.

a higher underlying catastrophe. As described in reference [52], swallowtails contain two cusps, and butterflies contain two swallowtails.

4.10 Stability Analysis

The stability of cold atoms in an optical cavity has been treated in Refs. [12, 53]. In this case we follow an approach more in line with [18], where the energy functional, Eq. (4.13), and the nonlinear equation of motion, Eq. (4.10), for the atomic wave function serve as the starting points for an examination of energetic, and dynamic stability, respectively. Hence, we examine the stability of the Bloch states at different values of quasi-momentum at fixed values of η and Δ_c. Before going into the details of the calculation we note that it is well known from the study of bistability in classical nonlinear cavity systems, that the back-bent branch of the lineshape profile shown in Fig. 4.2 is unstable, see, for example, [3]. From the three dimensional plots Fig. 4.12 and Fig. 4.13, we see that this back-bent branch corresponds to the upper branch of the loop in energy-quasi-momentum space. Thus, we expect to find this branch unstable.

We first consider energetic stability in the spirit of [18]. The grand canonical potential per unit

length is $G[\psi] = E[\psi] - \mu N$

$$\frac{G[\psi]}{N} = \frac{1}{\pi}\int_0^\pi dx \left|\frac{d\psi}{dx}\right|^2 - \frac{\eta^2}{\kappa N}\arctan\left(\frac{\Delta_c - \frac{NU_0}{\pi}\int_0^\pi \mathrm{d}x|\psi|^2\cos^2(x)}{\kappa}\right) - \mu\int dx|\psi(x)|^2. \tag{4.48}$$

We perturb the wavefunction as $\psi(x) = \psi_0(x) + \delta\psi(x)$, where ψ_0 extremizes G, i.e. one of the solutions that we obtained in Sec. 4.5. Since ψ_0 is an extremum, the first order variation in G vanishes and the second order contribution can be written as

$$\frac{\delta G_2}{N} = \langle\delta\psi|H_0|\delta\psi\rangle + \rho\langle\delta\psi|\cos^2(z)|\psi_0\rangle^2 + \rho\langle\psi_0|\cos^2(z)|\delta\psi\rangle^2 + 2\rho\langle\delta\psi|\cos^2(z)|\psi_0\rangle\langle\psi_0|\cos^2(z)|\delta\psi\rangle, \tag{4.49}$$

where

$$H_0 = -\frac{d^2}{dz^2} + U_0 n_{\mathrm{ph}}\cos^2(z) \tag{4.50}$$

and

$$\rho = \frac{\eta^2 N^2 U_0^2}{\kappa^3}\frac{\frac{\Delta_c - NU_0\langle\psi_0|\cos^2(z)|\psi_0\rangle}{\kappa}}{1+\left(\frac{\Delta_c - NU_0\langle\psi_0|\cos^2(z)|\psi_0\rangle}{\kappa}\right)^2}. \tag{4.51}$$

Equation (4.49) can be cast into a simple matrix form [18]

$$\frac{\delta G_2}{N} = \frac{1}{2}\int dx\Psi^\dagger(x)A\Psi(x). \tag{4.52}$$

Here

$$\Psi(x) = \begin{pmatrix}\delta\psi(x)\\ \delta\psi^*(x)\end{pmatrix}$$

and

$$A = \begin{pmatrix} H_0 + 2\rho\cos^2(x)\psi_0(x)I^*[\dots] & 2\rho\cos^2(x)\psi_0(x)I[\dots] \\ 2\rho\cos^2(x)\psi_0^*(x)I^*[\dots] & H_0 + 2\rho\cos^2(x)\psi_0^*(x)I[\dots]\end{pmatrix},$$

where $I[\dots]$ is an integral operator defined by

$$I[\delta\psi^*(x)] \equiv \int \mathrm{d}x\cos^2(x)\psi_0(x)\delta\psi^*(x). \tag{4.53}$$

The eigenvalues of the matrix A decide the energetic stability. If A is positive definite, the solution ψ_0 is energetically stable.

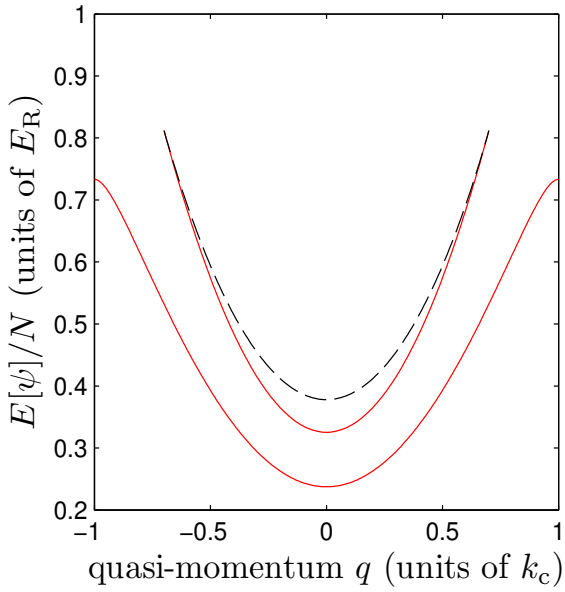

Figure 4.22. Energetic and dynamical stability of the band structure loops. The upper branch of the loop (black dashed line) is energetically and dynamically unstable. The other branches (red lines) are energetically and dynamically stable. Parameters are, $\Delta_c = 3140\,\omega_{\rm R}$, $\kappa = 350\,\omega_{\rm R}$, $U_0 = \omega_{\rm R}$, $N = 10^4$, $\eta = 2.8\,\eta_0$, and $\eta_0 = 325\,\omega_{\rm R}$.

In order to examine dynamic stability, we linearize the equation of motion Eq. (4.10) by writing $\psi(x,t) = [\psi_0(x) + \delta\psi(x,t)]e^{-i\mu t}$. This leads to

$$i\frac{{\rm d}\delta\psi}{{\rm d}t} = \left[-\frac{{\rm d}^2}{{\rm d}x^2} + U_0 \mid \alpha_0 \mid^2 \cos^2(x) - \mu\right]\delta\psi(x) + 2\rho\cos^2(x)\psi_0(x)\left(I^*[\delta\psi(x)] + I[\delta\psi^*(x)]\right). \quad (4.54)$$

One can write a similar equation for $\delta\psi^*$ and combine the two into a matrix equation similar to Eq. (4.52)

$$i\frac{{\rm d}\delta\Psi}{{\rm d}t} = \sigma_z A\delta\Psi, \quad (4.55)$$

where σ_z is the Pauli z-matrix. The solution ψ_0 is dynamically stable if all the eigenvalues of $\sigma_z A$ are real. Thus, the occurrence of complex eigenvalues of $\sigma_z A$ signals dynamical instability. Before we quote the results, a comment is in order about the form of the perturbations $\delta\psi$. The integral operator in Eq. (4.53) couples the perturbation and ψ_0. If $\psi_0 = e^{iqx}U_q(x)$, with $U_q(x) = U_q(x+\pi)$, i.e. a Bloch function with quasi-momentum q, the form of $\delta\psi$ that leads to non-zero coupling is

$$\delta\psi(x) = e^{iqz}\sum_j b_j e^{i2jx}. \quad (4.56)$$

That is, the perturbation should be a Bloch wave with the same quasi-momentum as ψ_0. In Eq. (4.49)

we consider the change in the grand canonical potential per unit length, but the above choice is made to satisfy the requirement that the integral operator I over the system size gives a non-zero answer. A physical way to motivate the above choice goes as follows: in the absence of interatomic interactions the allowed excitations of the quasi-momentum state q have to be in multiples of the crystal momentum $2k_c$ (simply 2 in dimensionless units) since the only source of perturbation is the interaction with the cavity field. The above form respects this requirement. Also, the number of terms in the Fourier expansion Eq. (4.56) has to be less than the number of terms in the original expansion for ψ_0 in Eq. (4.16) to avoid spurious instabilities [18]. Using Eq. (4.56), we find that the upper branch of the looped dispersions is both dynamically and energetically unstable as expected. The other two branches are stable. This is shown in Fig. 4.22 for one particular case. We shall not perform the stability analysis for the case when there are five solutions, but anticipate by an extension of the case for the bistability scenario, that two of the solutions will be dynamically unstable and three will be stable.

4.11 Summary and Conclusions

In this paper we have analyzed bistability in atom-cavity systems in situations where the atoms are in spatially extended states (Bloch waves) with non-zero quasi-momentum q. We find that bistability in the number of photons in the cavity goes hand-in-hand with the emergence of loops in the band structure. Both are manifestations of a bifurcation in the stationary solutions of the coupled atom-light equations of motion.

We have studied how the loops appear and disappear as the laser detuning and the laser pumping rate are changed. In particular, Eq. (4.31) provides an analytical estimate of the critical pump strength $\eta_{\rm cr}(q)$ at which bistability sets in. It depends on the quasi-momentum of the atomic state, and predicts that loops first appear at the edges of the first Brillouin zone ($q = \pm 1$) and then move inwards. This is indeed what we find upon solving the coupled atom-light equations numerically: swallowtail loops appear at the edges of the first Brillouin zone as the pump strength η is increased above $\eta_{\rm cr}(q = 1)$. As η is increased further the swallowtails extend inwards, merge, and detach from the rest of the band to form a separate loop centred at $q = 0$ which ultimately closes up and vanishes. A rather similar behaviour is observed as the pump-cavity detuning Δ_c is swept from below the cavity resonance to above it.

The loops we find are qualitatively different from those that occur for BECs in static optical lattices in the presence of repulsive interatomic interactions [17, 18, 19]. There, the loops are centered at the edge of Brillouin zone and cause the dispersion to have a finite slope at that point. By contrast, the band structure we find always has zero slope at the edge of the Brillouin zone. Nevertheless, there are also many similarities, including the stability of the various branches of the loops. We find that the upper branch of the loops are energetically and dynamically unstable, as expected from

optical bistability considerations.

The extra degree of freedom afforded by the quasi-momentum (over considering only $q = 0$) results in the possibility of tristability, namely regions of parameter space where there are five solutions, three stable and two unstable. The complexity of the solutions in parameter space led us to perform an analysis of the problem in terms of catastrophe theory which is a useful mathematical tool for understanding the organization of bifurcations of solutions. The key to our treatment was the recognition that, because exact solutions for the atomic wave functions are Mathieu functions which are specified only by the lattice depth (once one chooses a quasi-momentum), the photon number $n_{\rm ph}$ which determines the cavity depth provides a completely equivalent description to the wave function.

In the case of shallow lattices we were able to proceed analytically and found that the structure of the solutions in parameter space when $q = 0$ corresponds to a cusp catastrophe, at the most singular point of which three solutions (two stable and one unstable) form a pitchfork bifurcation, and this describes the onset of bistability as the laser pumping is increased. Interestingly, the three experimental parameters $\{\Delta_c, \eta, U_0\}$ reduced to just two effective control parameters. In the general case of arbitrary lattice depth and $0 \leq q \leq 1$, the highest singularities we found were swallowtail catastrophes where four solutions simultaneously merge. The swallowtails only exist when $q > q_{\rm sw} = 0.545$. However, there is good evidence that there is an underlying butterfly catastrophe, but, once again, the experimental parameters $\{\Delta_c, \eta, q, U_0\}$ reduced to three effective control parameters meaning that generically one is unable to locate the butterfly point (where five solutions simultaneously merge).

The band structure loops found here have important implications for Bloch oscillations of atoms in cavities [30, 31]. Bloch oscillations are essentially an adiabatic effect where, as a force is applied to the atoms they remain in the same band but their quasi-momentum evolves linearly in time, as shown in Eq. (4.22). Swallowtail loops in the band structure will have a deleterious effect on Bloch oscillations because, as the quasi-momentum evolves, the atoms will reach the edge of a loop where the branch they are following vanishes. This will lead to a sudden, non-adiabatic, disruption in the state of the atoms as they are forced to jump to another branch or even another band. For BECs in ordinary static optical lattices these non-adiabatic jumps are thought to be the cause of the destruction of superfluidity during Bloch oscillations [22, 23]. We have not included interactions in our treatment (interactions are necessary for superfluidity), but related effects will likely occur, especially considering the added heating due to the fact that the lattice depth will also abruptly change at the same point. However, when the loop detaches from the main band it will no longer affect Bloch oscillations. Furthermore, loops only occur for certain limited regions of parameter space, i.e. inside the cusp and swallowtail catastrophes shown in Figs 4.14, 4.15, and 4.21. For experiments involving Bloch oscillations we therefore recommend that parameter regimes are chosen which lie outside to these regions.

Finally, we add that although we have only considered Bloch waves in this paper, localized states (for example Wannier functions) can be formed from superpositions of Bloch waves with different values of the quasi-momentum. In this sense, localized states therefore contain all values of the quasi-momentum and so might be expected to display tristability too. However, it should be borne in mind that the nonlinearity of the system means that superpositions of Bloch states of different q but the same lattice depth will not in general obey the effective Schrödinger equation (4.10).

Acknowledgements

We gratefully acknowledge E. A. Hinds, D. Pelinovsky and M. Trupke for discussions. For funding, DHJO and BPV thank the Natural Sciences and Engineering Research Council of Canada, and the Ontario Ministry of Research and Innovation, and JL thanks VR/Vetenskapsrådet.

Appendix

We shall now sketch a proof showing that the function $\mathcal{G}$ defined in Eq. (4.42) produces swallowtail catastrophes between $0.545 \leq q \leq 1$ (in fact it produces two lines of swallowtail points, as shown in Fig. 4.20) where its derivatives up to third order vanish simultaneously [36, 54].

Consider, for example, the point in control and state space given by $C_0 = \{\Delta_c = 0.90, \eta = 14.5, q = 0.69, U_0 = 0.15\}$ and $v_0 = 7.75, n_{\rm ph} = 50.3$ (frequencies are measured in units of κ and the number of atoms is set at $N = 10^2$). The numerical package [50] we used for calculating the derivatives gives error bounds allowing us to estimate the accuracy of our calculations. For the point $\{C_0, v_0\}$ we found that the right hand side of Eq. (4.47) was equal to 8.09×10^{-15} with an error of 4.00×10^{-13}. This means that the third derivative of the state function vanishes within error, indicating a swallowtail point. However, the smallest value we found anywhere in parameter space for the difference between the left hand side and the right hand side of Eq. (4.46) was -8.64×10^{-5} with error 6.00×10^{-12}. This means that the fourth derivative of the state function does not vanish within error, suggesting there is no butterfly point. The value of the quasi-momentum at the point where we found this minimal fourth derivative was $q = q_{\rm sw} = 0.545$.

Before outlining the proof, we first give some definitions [36]. If n is the number of state variables, then consider a function p: $\mathcal{R}^n \to \mathcal{R}$

- $j^k p$ is the Taylor expansion of p to order k
- $J^k p$ is $j^k p$ minus its constant term
- p is k-deteminate at 0 if any smooth function $p + q$, where q is of order $k + 1$ (leading order term of the Taylor expansion is of order $k + 1$), can be locally expressed as $p(y(s))$ with y: $\mathcal{R}^n \to \mathcal{R}^n$ being a smooth reversible change of co-ordinates.

- E_n^k is the vector space of polynomials in $s_1, \ldots, s_n$ of degree $\leq k$.
- J_n^k is the subspace of E_n^k with zero constant term
- $\Delta_k(p)$ is the subspace of J_n^k spanned by all $\overline{Qj^k\left(\frac{\partial p}{\partial s_i}\right)}^k$, where $1 \leq i \leq n$, $Q \in E_n^k$, and the bar symbol represents the restriction to the k-th order of the expansion.
- The codimension of a function p is the codimension of $\Delta_k(p)$ in J_n^k for any k for which p is k-determinate.
- An $r-$unfolding of p at 0 is a function:

$$P : \mathcal{R}^{n+r} \to \mathcal{R},$$
$$(s_1, \ldots, s_n, t_1, \ldots, t_r) \mapsto P(s,t) = P_t(s),$$

  such that $P_{0,\ldots 0}(s) = p(s)$.

More informally, the term "unfolding" refers to how the catastrophe unfolds as one moves away from the origin in control space. At the origin in control space the catastrophe reduces to its most singular part, known as its *germ*. For example, from Table 4.1, the germ of the swallowtail catastrophe is given by s^5. The terms in the potential function which depend on the control parameters are called the unfolding terms, and the number of them is equal to the codimension. If P is an $r-$unfolding of p, set

$$\left\{w_1^k(P), \ldots, w_r^k(P)\right\} = \left\{\frac{\partial}{\partial t_1}\left(J^k(P_{t_1,0,\ldots,0})\right), \ldots, \frac{\partial}{\partial t_r}\left(J^k(P_{0,\ldots,t_r})\right)\right\}. \tag{4.57}$$

$W^k(P)$ is the subspace of J_n^k spanned by $\{w_1^k(P), \ldots, w_r^k(P)\}$.

Referring to the standard forms given in Table 4.1, the potential function and state equation for the swallowtail are given by

$$\Phi(s;C) = \frac{1}{5}s^5 + \frac{C_3}{3}s^3 + \frac{C_2}{2}s^2 + C_1 s \tag{4.58}$$
$$\mathcal{G}(s;C) \equiv s^4 + C_3 s^2 + C_2 s + C_1 = 0\ . \tag{4.59}$$

Notice that the state equation for a swallowtail catastrophe is similar to the potential function for a cusp catastrophe up to a constant C_1. Since the state function $\mathcal{G}$ is the central object in the treatment given in Section 4.9 rather than the potential function, instead of proving that the underlying potential function is equivalent to that of a swallowtail catastrophe, we will prove that the state function $\mathcal{G}$ around the singular point v_0 and C_0 is equivalent to the potential function of a cusp catastrophe (note that this is different from the small photon number case we studied in Section 4.9.2 where we showed that the underlying potential was equivalent to the potential for a

cusp catastrophe). To that end, first notice that the role of the constant term C_1 in Eq. (4.59) is played by $-\eta^2 U_0$ in Eq. (4.42). Subtracting this function we have a modified form of $\mathcal{G}$ (where we have also dropped the dependence on q since we are focusing on a particular quasi-momentum):

$$F(v;\{\Delta_c, U_0\}) = F(v;C) = v + v(\Delta_c - NU_0 f(v,q))^2 \tag{4.60}$$

which satisfies $F^{'}(v_0;C_0) = F^{''}(v_0;C_0) = F^{'''}(v_0;C_0) = 0$. In order to have a function defined in the neighborhood of v_0 and C_0, let us set the origin of v at v_0 and the origin of C at C_0 and define

$$F_1(v;\{\Delta_c, U_0\}) \equiv F(v+v_0, C+C_0) - F(v_0, C_0). \tag{4.61}$$

Thus, we have $F_1(0,0) = 0$ and for the function $g(v) \equiv F_1(v,\{0,0,0\})$ the most singular point is at $v = 0$ where $g^{'}, g^{''}, g^{'''}$ vanish. The function g is the germ which we described above, and is the key feature which identifies the catastrophe. When g is Taylor expanded around 0 one has

$$g(v) = \frac{g^{(iv)}}{4!}v^4 + \frac{g^{(v)}}{5!}v^5 + \mathcal{O}(v^6) \tag{4.62}$$

where $g^{(iv)}(0)$ is the first non-zero Taylor coefficient. This means that g is 4-determined around 0 and we say that $g \sim v^4$ around 0. According to Table 4.1, the canonical unfolding of the 4-determined germ around 0 is the cusp catastrophe $\Phi(s;C) = s^4/4 + C_2 s^2/2 + C_1 s$, where v and s are related via a differomorphism (smooth transformation of coordinates).

Next we calculate the codimension of g. The Jacobian ideal for g is in this case $\Delta_4(g) = \{v^4, v^3 + \frac{g^v}{4g^{iv}}|_{v=0} v^4\}$. Hence, the codimension of g is $\dim(J_1^4) - \dim(\Delta_4(g)) = 4 - 2 = 2$. The function F_1 is thus a 2 parameter unfolding of the germ g. In order to prove that the function F_1 can be described by a cusp catastrophe, we need to prove that F_1 is isomorphic as an unfolding to the canonical form $\Phi(s;C) = s^4/4 + C_2 s^2/2 + C_1 s$. In order to do this we need to invoke the idea of transversality.

Transversality generalizes what we know of two intersecting lines in a two dimensional plane to multidimensional manifolds. Two subspaces of a manifold are transverse if they meet in a subspace that is as small in dimension as possible. If X_1 (dim r) and X_2 (dim t) are subspaces of X (dim n), X_1 and X_2 are transverse if their intersection is empty or if it is of the dimension $\max(0, r+t-n)$. Our first aim is to prove that the $2-$unfolding of F_1 is a versal unfolding. To do this we use a defining theorem for versality from [36] which states that: an $r-$unfolding P of p, where p is k-determinate is versal if and only if $W^k(P)$ and $\Delta_k(p)$ (defined above) are transverse subspaces of J_n^k. We have

already found $\Delta_4(g)$, the polynomial space $W^4(F_1)$ is spanned by the vectors:

$$w_1(F_1) = \frac{\partial}{\partial U_0}\left(J^4(F_1(0, U_0, 0,))\right),$$
$$w_2(F_1) = \frac{\partial}{\partial \Delta_c}\left(J^4(F_1(0, 0, \Delta_c))\right),$$

The expressions depend on the derivatives of the coupling function $f(v, q)$ and the value of the parameters at the singular point $\{v_0, C_0\}$. They are too cumbersome to state here but their general forms are given by

$$w_i(F_1) = \sum_{j=1..4} z_{ij} v^j,$$

which we determined numerically and all of the z_{ij}'s are non-zero. The polynomials w_i are linearly independent which gives the dimensionality $\dim(W^4(F_1)) = 2$. Furthermore, we have verified that the rank of the matrix formed by the polynomial coefficieints of $\Delta_4(g)$ and $W^4(F_1)$ is 4 and this combined with the fact that $\dim(\Delta_4(g)) + \dim(W^4(F_1)) = 2 + 2 = \dim(J_1^4)$ proves that $\Delta_4(g)$ and $W^4(F_1)$ are transverse. Thus, by the theorem stated above F_1 is a versal unfolding of the germ g and since it is a $2-$unfolding (codimension of $g = 2$) it is also universal [36]. This proves the equivalence of the unfolding of F_1 to the cusp catastrophe.

Bibliography

[1] H. M. Gibbs, S. M. McCall, and T. N. C. Venkatesan, Phys. Rev. Lett. **36**, 1135 (1976).

[2] R. Bonifacio and L. A. Lugiato, Phys. Rev. Lett. **40**, 1023 (1978); R. Bonifacio and L. A. Lugiato, Phys. Rev. A **18**, 1129 (1978).

[3] P. Meystre and M. Sargent, *Elements of Quantum Optics*, 3rd edition, (SpringerVerlag, Berlin, 1997).

[4] C.W. Gardiner and P. Zoller, *Quantum Noise*, (Springer, Berlin, 2004).

[5] S. Gupta, K. L. Moore, K. W. Murch, and D. M. Stamper-Kurn, Phys. Rev. Lett. **99**, 213601 (2007).

[6] F. Brennecke, S. Ritter, T. Donner, and T. Esslinger, Science **322**, 235 (2008); S. Ritter, F. Brennecke, K. Baumann, T. Donner, C. Guerlin and T. Esslinger, App. Phys. B **95**, 213 (2009).

[7] C.J. Hood, M. S. Chapman, T. W. Lynn, and H. J. Kimble, Phys. Rev. Lett. **80**, 4157 (1998); P. Münstermann, T. Fischer, P. W. H. Pinkse, and G. Rempe, Opt. Comm. **159**, 63 (1999); M. Trupke, J. Goldwin, B. Darquié, G. Dutier, S. Eriksson, J. Ashmore, and E. A. Hinds, Phys. Rev. Lett. **99**, 063601 (2007).

[8] J. Ye, D. W. Vernooy, and H. J. Kimble, Phys. Rev. Lett. **83**, 4987 (1999); C. J. Hood, T. W. Lynn, A. C. Doherty, A. S. Parkins, and H. J. Kimble, Science **287**, 1447 (2000); P. W. H. Pinkse, T. Fischer, P. Maunz, G. Rempe, Nature **404**, 365 (2000).

[9] C. Maschler and H. Ritsch, Phys. Rev. Lett. **95**, 260401 (2005); I. B. Mekhov, C. Maschler and H. Ritsch, Nat. Phys. **3**, 319 (2007); C. Maschler, I. B. Mekhov, and H. Ritsch, Euro. Phys. J. D **46**, 545 (2008).

[10] J. Larson, B. Damski, G. Morigi, and M. Lewenstein, Phys. Rev. Lett. **100**, 050401 (2008); J. Larson, S. Fernandez-Vidal, G. Morigi, and M. Lewenstein, New J. Phys **10**, 045002 (2008).

[11] J. M. Zhang, F. C. Cui, D. L. Zhou, and W. M. Liu, Phys. Rev. A **79**, 033401 (2009).

[12] D. Nagy, P. Domokos, A. Vukics, and H. Ritsch, Eur. Phys. J. D, **55**, 659 (2009).

[13] L. Zhou, H. Pu, H. Y. Ling, and W. Zhang, Phys. Rev. Lett., **103** , 160403 (2009).

[14] D. Nagy, G. Szirmai, and P. Domokos, Euro. Phys. J. D **48**, 127 (2008); S. Fernandez-Vidal, G. De Chiara, J. Larson, and G. Morigi, Phys. Rev. A **81**, 043407 (2010); D. Nagy, G. Konya, G. Szirmai, and P. Domokos, Phys. Rev. Lett **104**, 130401 (2010).

[15] K. Baumann, C. Guerlin, F. Brennecke, and T. Esslinger, Nature **464**, 1301 (2010).

[16] O. Morsch and M. Oberthaler, Rev. Mod. Phys. **78**, 179 (2006).

[17] B. Wu and Q. Niu, Phys. Rev. A **64**, 061603(R) (2001); B. Wu, R. B. Diener, and Q. Niu, Phys. Rev. A **65**, 025601 (2002); B. Wu and Q. Niu, N. J. Phys. **5**, 104 (2003).

[18] Dmitri Diakonov, L. M. Jensen, C. J. Pethick, and H. Smith, Phys. Rev. A **66**, 013604 (2002); M. Machholm, C. J. Pethick, and H. Smith, Phys. Rev. A **67**, 053613 (2003); M. Machholm, A. Nicolin, C. J. Pethick, and H. Smith, Phys. Rev A **69**, 043604 (2004).

[19] E. J. Mueller, Phys. Rev. A **66**, 063603 (2002).

[20] A. Smerzi, A. Trombettoni, P. G. Kevrekidis, and A. R. Bishop, Phys. Rev. Lett. **89**, 170402 (2002).

[21] C. J. Pethick and H. Smith, *Bose Einstein Condensation in Dilute Gases*, 2nd edition (Cambridge University Press, Cambridge, 2008).

[22] S. Burger, F. S. Cataliotti, C. Fort, F. Minardi, M. Inguscio, M.L. Chiofalo and M. P. Tosi, Phys. Rev. Lett. **86**, 4447 (2001).

[23] S. Cataliotti, L. Fallani, F. Ferlaino, C. Fort, P Maddaloni, and M. Inguscio, New J. Phys. **5**, 71 (2003).

[24] B. Wu and Q. Niu, Phys. Rev. A **61**, 023402 (2000).

[25] Y.-A. Chen, S. D. Huber, S. Trotzky, I. Bloch, and E. Altman, Nat. Phys. **7**, 61 (2011).

[26] R. Battesti, P. Cladé, S. Guellati-Khélifa, C. Schwob, B. Grémaud, F. Nez, L. Julien, and F. Biraben, Phys. Rev. Lett. **92**, 253001 (2004); P. Cladé, E. de Mirandes, M. Cadoret, S. Guellati-Khélifa, C. Schwob, F. Nez, L. Julien, and F. Biraben, Phys. Rev. Lett. **96**, 033001 (2006).

[27] G. Roati, E. de Mirandes, F. Ferlaino, H. Ott, G. Modugno, and M. Inguscio, Phys. Rev. Lett. **92**, 230402 (2004).

[28] G. Ferrari, N. Poli, F. Sorrentino, and G. M. Tino, Phys. Rev. Lett. **97**, 060402 (2006).

[29] I. Carusotto, L. P. Pitaevskii, S. Stringari, G. Modugno, and M. Inguscio, Phys. Rev. Lett. **95**, 093202 (2005).

[30] B. M. Peden, D. Meiser, M. L. Chiofalo, and M. J. Holland, Phys. Rev. A **80**, 043803 (2009).

[31] B. Prasanna Venkatesh, M. Trupke, E. A. Hinds, and D. H. J. O'Dell, Phys. Rev. A **80**, 063834 (2009).

[32] M. Gustavsson, E. Haller, M. J. Mark, J. G. Danzl, G. Rojas-Kopeinig, and H.-C. Nagerl, Phys. Rev. Lett. **100**, 080404 (2008).

[33] R. Thom, *Structural Stability and Morphogenesis*, (Benjamin, London, 1975).

[34] V. I. Arnold, Russ. Math. Surveys **30**, 1 (1975).

[35] Michael Berry *Singularities in Wave and Rays* in Les Houches, Session XXXV, 1980 *Physics of Defects*, edited by R. Balian *et al.* (North-Holland Publishing Company, Amsterdam, 1981).

[36] T. Poston and I. Stewart, *Catastrophe Theory and Its Applications*, (Dover Publications, NewYork, 1996).

[37] J. F. Nye *Natural Focusing and Fine Structure of Light*, (Institute of Physics, Bristol, 1999).

[38] R. Gilmore and L. M. Narducci, Phys. Rev. A **17**,1747 (1978).

[39] G. P. Agrawal and H. J. Carmichael, Phys. Rev. A **19**, 2074 (1979).

[40] Langevin fluctuation terms do not appear in Eq. (4.5) if the bath is at thermal equilibrium. See p 343 of C. Cohen-Tannoudji, J. Dupont-Roc and G. Grynberg, *Atom-Photon Interactions* (Wiley, New York, 1992).

[41] J. Larson, G. Morigi, and M. Lewenstein, Phys. Rev. A **78**, 023815 (2008).

[42] F. Bloch, Z. Phys. **52**, 555 (1928).

[43] C. Zener, Proc. R. Soc. London, Ser. A **145**, 523 (1934).

[44] M. Abramowitz and I. Stegun, *Handbook of Mathematical Functions* (National Bureau of Standards, Washington, 1964).

[45] M. Ben Dahan, E. Peik, J. Reichel, Y. Castin, and C. Salomon, Phys. Rev. Lett. **76**, 4508 (1996); O. Morsch, J. H. Müller, M. Cristiani, D. Ciampini, and E. Arimondo, Phys. Rev. Lett. **87**, 140402 (2001).

[46] T. J. Kippenberg and K. J. Vahala, Science **321**, 1172 (2008); F. Marquardt and S. M. Girvin, Physics **2**, 40 (2009).

[47] Y. Dong, J. Ye, and H. Pu, Phys. Rev. A **83**, 031608(R) (2011).

[48] L. D. Landau and E. M. Lifshitz, *Statistical Physics*, Part 1 3rd Edition (Butterworth-Heinemann, New York, 2003).

[49] MATLAB 2008a, MathWorks, Inc., MA, USA.

[50] http://www.mathworks.com/matlabcentral/fileexchange/13490-automatic-numerical-differentiation, J. D. Errico (2006).

[51] Another possibility is that the butterfly point is exactly located at the point $1/(NU_0)^2 = 0$, and q can take any value. This is a rather unphysical situation because, assuming a finite number of atoms, it can only occur when $U_0 \to \infty$ and this then means $v \to \infty$. From Fig. 4.5, we see that when $v \to \infty$ the function $f(v, q)$ becomes very flat and so all its derivatives vanish allowing Eqns (4.43)-(4.46) to be satisfied in a rather trivial way. Therefore, we ignore this solution.

[52] A. E. R. Woodcock and T. Poston, *A Geometrical Study of the Elementary Catastrophes*, (Springer-Verlag, Berlin, 1974).

[53] P. Horak and H. Ritsch, Phys. Rev. A **63**, 023603 (2001).

[54] J. Gaite, J. Margalef-Roig, and S. Miret-Artés, Phys. Rev. B **57**, 13527 (1998).

Chapter 5

Bloch Oscillations of Cold Atoms in a Cavity: Effects of Quantum Noise

Preface

In this chapter we return to examine Bloch oscillations in an optical cavity. In Chapter 3 the atomic and light degrees of freedom were described in the meanfield approximation. Here, we are interested in the dynamics of the quantised fluctuations about the meanfields. We assume that the cavity is in contact with a zero temperature electromagnetic bath through the partially transmissive mirrors. The fluctuations in the cavity light field are then driven by the vacuum fluctuations of the external electromagnetic field. Due to the atom-light coupling the vacuum fluctuations affect the atomic fluctuation dynamics as well. The effect of vacuum fluctuations on the atomic degree of freedom can also be understood as a manifestation of quantum measurement backaction [104, 105] arising from the continuous leaking of the light field from the cavity.

We obtain the quantised fluctuations by solving the coupled Heisenberg-Langevin equations for the atomic and light fields in the regime where the fluctuation potential provide a small correction to the meanfields. One challenging aspect of this is that the meanfields about which the fluctuations are calculated are not static but are given by the Bloch oscillating solutions that we discussed in Chapter 3. Previous studies on cavity cooling [61, 62, 63, 64], have shown that atomic fluctuations can be damped due to the finite response time of the cavity field to changes in atomic configuration. However, we find that this cooling effect vanishes when Bloch oscillations are present and we identify the mechanism underlying this modification. We also compute how the signal-to-noise ratio (SNR) for a measurement of the Bloch frequency is affected due to the inclusion of the fluctuations. Thus, the material discussed in this chapter extends and augments the main problem presented in the earlier parts of this thesis.

Abstract

We extend our theory of Bloch oscillations of cold atoms inside an optical cavity [B. P. Venkatesh *et al.*, Phys. Rev. A **80**, 063834 (2009)] to include the effects of quantum noise arising from coupling to external modes. The noise acts as a form of quantum measurement backaction by perturbing the coupled dynamics of the atoms and the light. We take it into account by solving the Heiseberg-Langevin equations for linearized fluctuations about the atomic and optical meanfields and examine how this influences the signal-to-noise ratio of a measurement of external forces using this system. In particular, we investigate the effects of changing the number of atoms, the intracavity lattice depth, and the atom-light coupling strength, and show how resonances between the Bloch oscillation dynamics and the quasiparticle spectrum have a strong influence on the signal-to-noise ratio as well as heating effects. One of the hurdles we overcome in this paper is the proper treatment of fluctuations about time-dependent meanfields in the context of cold atom cavity-QED .

5.1 Introduction

When quantum particles in a periodic potential of period d are subject to a weak additional constant force F they do not uniformly accelerate like free particles, but instead undergo Bloch oscillations [1] at an angular frequency given by:

$$\omega_{\mathrm{B}} = Fd/\hbar \; . \tag{5.1}$$

Bloch oscillations (BOs) of cold atoms in optical lattices were first observed in 1996 by uniformly accelerating the lattice [2]: in a frame co-moving with the lattice the atoms experience a constant force. At about the same time, the accelerating lattice method was used to observe Wannier-Stark ladders [3], which are a different aspect of the same "tilted lattice" physics. The method has subsequently been employed to realize beam splitters for atom optics capable of large momentum transfers, see, e.g. [4].

In gravity-driven BOs the lattice is held fixed in space but oriented vertically so that gravity provides the force $F_g = mg$ on the atoms (of mass m). From Eq. (5.1), a measurement of ω_{B} corresponds to a measurement of the applied force F if we know $d/\hbar$. This Bloch oscillator may be viewed as an interferometer in momentum space [5] and has been experimentally demonstrated by a number of groups [6, 7, 8, 9]. For example, the experiment [9] used gravity-driven BOs of strontium atoms to measure the local acceleration due to gravity at the level of $\Delta g/g = 5 \times 10^{-6}$. Like any interferometer, long coherence times are crucial for precision measurements and in [9] the BOs were coherent over 7 s, corresponding to ≈ 4000 oscillations. This remarkable degree of coherence was greatly facilitated by the choice of strontium atoms, which have very weak s-wave scattering, and thus dynamical instabilities normally associated with superflow in lattices [10, 11] were highly suppressed. Variations on this scheme that improve the visibility of the BOs, including frequency [12] and amplitude [13, 14] modulation of the lattice, have allowed for the measurement of gravity at the level of $\Delta g/g = 10^{-9}$. In these latest experiments the BOs were coherent for over 20 seconds.

The experiments referred to above all involve destructive measurements of the BOs due to the nature of the imaging process of the atoms, whether it be *in situ* or by a time-of-flight technique after the lattice has been switched off [14]. Therefore, a precision measurement of ω_{B} by the above methods requires that the experiment be re-run many times, each run being for a slightly different hold time, so that the oscillations can be accurately mapped out. This not only takes a long time, but also requires that the initial conditions be recreated as faithfully as possible for each run.

In [15] we proposed a scheme for continuous (i.e. non-destructive) measurements of BOs based upon placing the atoms inside a Fabry-Perot optical resonator which would allow for an estimate of ω_{B} from the data acquired over a single run. A related scheme has also been independently proposed for ring cavities [16]. The periodic potential is now provided by the standing wave of light which forms inside the cavity when it is pumped by a laser. Orienting the cavity vertically, the atoms

execute BOs along the cavity axis as depicted in Fig. 5.1. The enhanced atom-light coupling inside a high-Q cavity means that the oscillating atoms imprint a detectable periodic modulation on both the phase and amplitude of the light which can be seen either in transmission or reflection. Thus, the measurement is performed upon the light leaking out of the cavity rather than directly upon the atoms.

The strong atom-light coupling that can be realized in cavity-QED stands in contrast to the case of optical lattices in free space where the atoms exert only a tiny backaction upon the light. The optical dipole interaction between a single cavity photon and a single atom is characterized by the Rabi frequency $g_0 = (\mu/\hbar)\sqrt{\hbar\omega_c/(\varepsilon_0 V)}$, where ω_c and V are the frequency and volume of the relevant cavity mode and μ is the atomic transition dipole moment. Defining the cooperativity $C \equiv g_0^2/(2\gamma\kappa)$, where 2γ is the spontaneous emission rate of the atom in free space and 2κ is the energy damping rate of the cavity, $1/C$ is the number of atoms required to strongly perturb the light field. The normal mode splitting that results from strong coupling has been directly observed in a number of cold atom optical cavity experiments [17, 18, 19, 20]. In the experiment [20], which was performed with a Bose-Einstein condensate, the cooperativity was $C = 145$. Even more pertinently, these systems have been used to detect the presence of single atoms [21, 22, 23], as well as to follow their dynamics in real time [24, 25]. The collective dynamics of ultracold atomic gases have also been tracked using cavities [26, 27, 28]. The key experimental steps necessary for the continuous monitoring of BOs in a cavity have, therefore, already been demonstrated.

The drawback with any continuous measurement scheme is measurement backaction. In cavities this backaction typically takes the form of cavity photon number fluctuations which lead to random force fluctuations on the atoms, as is evident in the erratic nature of the single atom trajectories seen in the experiments [24, 25] referred to above. In the many atom context, quantum measurement backaction generally manifests itself in a heating of the atom cloud (although under some circumstances it can lead to cooling [29]). In the cavity-optomechanical regime (where the collective motion can be modelled as a harmonic oscillator of angular frequency ω) the heating rate is expected to be $R = (x_{\rm zpf}/\hbar)^2 S_{\mathcal{F}\mathcal{F}}(-\omega)$ [30], where $x_{\rm zpf}$ is the zero-point fluctuation and $S_{\mathcal{F}\mathcal{F}}$ is the spectral density of the force fluctuations (which is directly proportional to the cavity photon number fluctuations). This heating rate is in agreement with observations when convolved with technical fluctuations [31].

In the system considered in this paper (see Fig. 5.1), we can divide the backaction into two types. One type comes from the fact that the atoms sit in an optical lattice whose depth is periodically modulated in time at the frequency ω_B due to the effect of BOs. This backaction is a classical effect in the sense that it occurs even when the light field is treated classically (no photons). The nonlinearity that arises from this backaction can lead to swallowtail loops in the atomic band structure [32, 33] that mimics the effects of direct atom-atom interactions [34, 35, 36, 37]. These loops are the counterpart in the atomic wave function of optical bistability in the light [26, 27, 28, 38]. The second type of backaction arises only when the fluctuations due to the discrete photon nature of the light field are

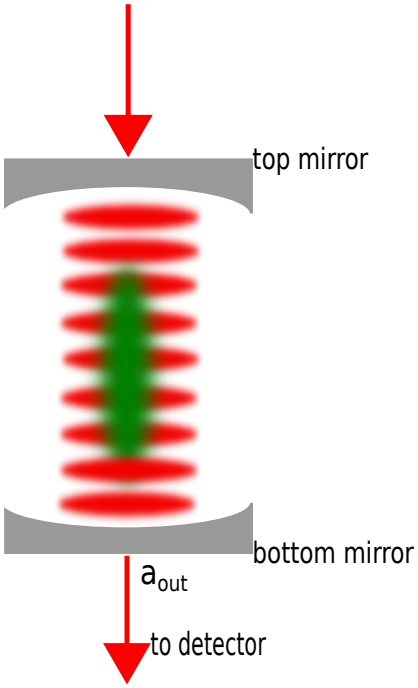

Figure 5.1. Schematic of the precision measurement proposal in [15]. A dilute cloud of cold atoms undergoes BOs in the combined intracavity lattice potential and the acceleration due to gravity. The transmitted light field's intensity and phase are modulated at the Bloch frequency. A in-situ precise measurement of the Bloch frequency (and hence the force) can be performed by detecting the transmitted light.

taken into account and is related to the heating effect mentioned above. The characteristic frequency of these latter fluctuations is κ which is much larger than $\omega_{\rm B}$.

The first type of backaction was analyzed in our previous paper [15] where our main aim was to show that, despite the self-generated time modulation of the intracavity optical lattice, the Bloch acceleration theorem still applies and the BO frequency is not modified (although harmonics can be generated). This latter result is clearly very important if the cavity BO method is to be used for precision measurements and may be viewed as a consequence of the fact that the formula (5.1) does not depend on the depth of the lattice, only its spatial period. An estimate of the effects of the second type of backaction was also given in our previous paper, but this estimate was obtained under the assumption that the photon number fluctuations were purely due to the photon shot noise found in a coherent state of light. This ignores the correlations that build up between the atoms and the light inside the cavity and our main aim in this paper is to solve the dynamics of the coupled photon and atom fluctuations systematically from first principles and thereby capture these correlations. This will allow us to properly determine the sensitivity of the measurement of the Bloch frequency to quantum fluctuations.

The plan of this paper is as follows: in Section 5.2 we introduce the physical system, the associated hamiltonian, and the equations of motion. We then review in Sections 5.3 and 5.4 the meanfield approximation and the associated numerical results which were the focus of our previous paper [15], before introducing in Section 5.5 the main model to be treated in this paper which adds quantum fluctuations. This is an elaboration of the linearization approach presented in, e.g. [39, 40, 41], to include a time-dependent meanfield component (due to the BOs). The fluctuations correspond to quasiparticles (excitations out of the meanfield), and their spectrum is analyzed in Section 5.6 and then used to help interpret the numerical results for the quantum dynamics presented in Section 5.7. We also develop a simple rate equation picture, valid in the weak coupling regime, to help us understand the rate of quasiparticle excitation. Following this we change gears slightly and apply the above results to investigate how quantum fluctuations affect a precision measurement of $\omega_{\rm B}$ by calculating the signal-to-noise ratio (SNR). We present the theory lying behind these calculations in Section 5.8 and in Section 5.9 we examine the results, paying particular attention to whether or not there is an optimal value for the atom-light coupling parameter $\beta = NU_0/\kappa$. We also present results illustrating the dependence of the SNR on other system parameters such as the number of atoms and the intracavity lattice depth. We summarize our results and provide some perspective in Section 5.10. We have also provided three appendices that give details omitted from the main text: the first derives an approximation wherein the cavity field is assumed to be in a coherent state and the atomic fluctuations about the meanfield are treated as independent oscillators, the second discusses the effects that BOs have on cavity cooling, and the third discusses our approach to calculating two-time correlation functions.

5.2 Hamiltonian and Equations of Motion

Our system consists of a gas of N bosonic atoms inside a vertically oriented Fabry-Perot optical cavity. A single cavity mode of frequency $\omega_{\rm c}$ is coherently pumped by a laser with frequency $\omega_{\rm p}$ that is detuned from both the atomic and the cavity resonance frequencies. This sets up a standing wave mode along the cavity axis of the form $\cos(k_{\rm c}z)$, where $k_{\rm c} = \omega_{\rm c}/c$. The relevant frequency relations are characterized by the two detunings

$$\Delta_{\rm c} \equiv \omega_{\rm p} - \omega_{\rm c}, \tag{5.2a}$$

$$\Delta_a \equiv \omega_{\rm p} - \omega_a, \tag{5.2b}$$

where ω_a is the atomic transition frequency. In the dispersive regime, the occupation of the excited atomic state is vanishingly small and it can be adiabatically eliminated. A one-dimensional hamiltonian for the atom-cavity system in the dispersive regime can then be written as [42, 43]

$$\hat{H} = -\hbar\Delta_{\rm c}\hat{a}^\dagger\hat{a} + i\hbar\eta\left(\hat{a}^\dagger - \hat{a}\right) + \int {\rm d}z\ \hat{\Psi}^\dagger\left[-\frac{\hbar^2}{2M}\frac{\partial^2}{\partial z^2} + \hbar U_0\hat{a}^\dagger\hat{a}\cos^2(k_{\rm c}z) - Fz\right]\hat{\Psi}, \tag{5.3}$$

where $\hat{\Psi}(z,t)$ and $\hat{a}(t)$ are the field operators for the atoms and the cavity photons which obey the equal time bosonic commutation relations $[\hat{\Psi}(x,t), \hat{\Psi}^\dagger(x',t)] = \delta(x-x')$, and $[\hat{a}(t), \hat{a}^\dagger(t)] = 1$, respectively. The single atom dispersive light shift has been denoted by $U_0 \equiv g_0^2/\Delta_a$.

The hamiltonian has been written in a frame rotating with the pump laser frequency $\omega_{\rm p}$, and this leads to the appearance of the two detunings. The first term is just the free evolution of the cavity mode. The second term represents the laser coherently pumping the cavity at rate η, and the third term describes the atomic part of the hamiltonian. The first two terms of the atomic part represent the kinetic energy and a light induced potential energy. This latter term can either be understood as the atom moving in a periodic potential with average amplitude $\hbar U_0\langle\hat{a}^\dagger\hat{a}\rangle$ or, if combined with the first term in the hamiltonian, as a shift in the resonance frequency of the cavity due to the coupling between the atom and the field. The third term in the atomic part provides the external force that drives the BOs. We assume this force arises from the vertical orientation (z increases in the downward direction) of the cavity and is given by $F = Mg$.

We have not included direct atom-atom interactions in the hamiltonian (5.3) because under realistic experimental conditions they are three orders of magnitude smaller than the recoil energy $E_{\rm R} \equiv \hbar^2k_{\rm c}^2/(2M)$ which characterizes the single-particle energy (kinetic and potential) of an atom in an optical lattice. Consider, for example, the meanfield interaction energy per particle $E_{\rm int}/N = (2\pi\hbar^2 a_s N/M)\int|\Phi(\mathbf{r})|^4 d^3r$ for a cloud of $N = 5\times10^4$ ^{87}Rb atoms trapped in a 178 μm long cavity [28]. Here $a_s = 5.3$ nm is the s-wave scattering length. We take the normalized 3D wave function $\Phi(\mathbf{r})$ to be the product of a ground band Bloch wave that extends 178 μm along z and a gaussian 25 μm wide in the transverse plane. Then, evaluating the Bloch wave for a lattice which is 3 $E_{\rm R}$ deep

and made from 780 nm light (456 wells are occupied), we find the ratio $E_{\rm int}/N : E_{\rm R} = 1.1 \times 10^{-3}$. The interactions can be tuned to smaller values still using a Feshbach resonance: the experiment [44] increased the dephasing time of BOs from a few oscillations to 20,000 using this technique. The fact that the atoms all interact with a common light field whose magnitude is modified by the sum of their individual couplings gives rise to a nonlinearity (the classical backaction referred to above) that is in some ways analogous to that due to direct interactions [32, 45], but in other ways differs and can lead to novel behavior [42, 43, 46].

Natural units for the length and energy in cavity-QED are given by $1/k_{\rm c}$ and the recoil energy $E_{\rm R}$, respectively. From here on we scale all lengths by $1/k_{\rm c}$ and consequently define $x \equiv k_{\rm c} z$. We scale frequencies by the recoil frequency $\omega_{\rm R} \equiv E_{\rm R}/\hbar$ and time by $1/\omega_{\rm R}$ and retain the same symbols for the scaled variables. The Heisenberg-Langevin equations of motion for the light and atomic field operators in the scaled variables are [42]

$$i\frac{d\hat{a}}{dt} = \Big[-\Delta_{\rm c} + \int dx\ \hat{\Psi}^\dagger(x,t)\hat{\Psi}(x,t)U_0\cos^2(x) - i\kappa\Big]\hat{a} + i\eta + i\sqrt{2\kappa}\hat{\xi}(t) \tag{5.4a}$$

$$i\frac{\partial\hat{\Psi}}{\partial t} = \Big[-\frac{\partial^2}{\partial x^2} + U_0\hat{a}^\dagger\hat{a}\cos^2(x) - fx\Big]\hat{\Psi} \tag{5.4b}$$

where $f \equiv F/(\hbar k_{\rm c}\omega_{\rm R}) = \omega_{\rm B}/(\pi\omega_{\rm R})$ is the dimensionless form for the external force. The operator $\hat{\xi}(t)$ is the Langevin term and is assumed to be Gaussian white noise with the only non-zero correlation being

$$\langle\hat{\xi}(t)\hat{\xi}^\dagger(t')\rangle = \delta(t-t'). \tag{5.4c}$$

Mathematically, the Langevin noise terms are necessary in order to preserve the commutation relation $[\hat{a}(t), \hat{a}^\dagger(t)] = 1$ in an open system. Physically, their origin is vacuum fluctuations of the electromagnetic field that are transmitted into the cavity via the mirrors and they thus only appear in the equations for the light field. Nevertheless, the noise is conveyed to the atomic dynamics by the atom-light coupling.

5.3 Meanfield dynamics: theory

The approach we follow in this paper is based upon a separation of the field operators into meanfield and quantum parts:

$$\hat{a}(t) = \alpha(t) + \delta\hat{a}(t) \tag{5.5a}$$

$$\hat{\Psi}(x,t) = \sqrt{N}\varphi(x,t) + \delta\hat{\Psi}(x,t). \tag{5.5b}$$

In the meanfield approximation the light is assumed to be in a classical state with amplitude $\alpha(t) = \langle \hat{a}(t) \rangle$, where $|\alpha(t)|^2$ corresponds to the average number of photons in the cavity, and the atoms are assumed to all share the same single-particle wave function $\varphi(x,t) = \langle \hat{\Psi}(x,t) \rangle / \sqrt{N}$. The equations of motion for the meanfield amplitudes $\alpha(t)$ and $\varphi(x,t)$ are

$$i\frac{d\alpha(t)}{dt} = \left[-\Delta_{\rm c} + NU_0\langle \cos^2(x)\rangle - i\kappa\right]\alpha(t) + i\eta \tag{5.6a}$$

$$i\frac{\partial\varphi(x,t)}{\partial t} = \left[-\frac{\partial^2}{\partial x^2} + |\alpha(t)|^2 U_0\cos^2(x) - fx\right]\varphi(x,t) \tag{5.6b}$$

where the second equation has the form of a Schrödinger equation. The expectation value

$$\langle \cos^2(x)\rangle(t) = \int dx |\varphi(x,t)|^2 \cos^2(x) \tag{5.6c}$$

that appears in the first of these equations provides the time-dependent coupling between the atomic probability density and the cavity mode function. Multiplying this integral is the collective atom-cavity coupling parameter NU_0. When measured in units of the cavity linewidth we denote this parameter by β

$$\beta \equiv NU_0/\kappa\,. \tag{5.7}$$

We illustrate the effect that β has on the meanfield dynamics in Figs. 5.2 and 5.3 below.

In reference [32] we studied the influence the classical backaction nonlinearity has upon the band structure of atom-cavity systems. The band structure is given by the steady state solutions [$\dot{\alpha} = 0$, $\varphi(x,t) = \varphi(x)\exp(-i\mu t/\hbar)$] of the coupled equations of motion (5.6a) and (5.6b) in the absence of the external force f. It is straightforward to see that, despite the nonlinearity, exact solutions of the steady state problem are given by Mathieu functions (like in the linear problem of a quantum particle in a fixed cosine potential). Mathieu functions are Bloch waves and so can be labelled by a band index b and quasimomentum q [47]

$$\varphi_{q,b}(x) = e^{iqx}\mathcal{U}_{q,b}(x) \tag{5.8}$$

where $\mathcal{U}_{q,b}(x+\pi) = \mathcal{U}_{q,b}(x)$ has the same period as the lattice. In the reduced zone picture q is restricted to lie in the first Brillouin zone $-1 < q \leq 1$. Substituting the Bloch wave solution into the equations of motion yields the steady state equations

$$\alpha_{ss} = \frac{i\eta}{\Delta_{\rm c} - NU_0\langle\cos^2(x)\rangle + i\kappa} \tag{5.9a}$$

$$\mu_{q,b}\mathcal{U}_{q,b}(x) = \left[\left(-i\frac{\partial}{\partial x} + q\right)^2 + |\alpha_{ss}|^2 U_0\cos^2(x)\right]\mathcal{U}_{q,b}(x) \tag{5.9b}$$

where the subscript ss denotes "steady state". Solving these equations one obtains a *band structure*

analogous to that in the linear case but with the striking difference that the nonlinearity can lead to swallowtail loops in the bands. It is important to appreciate that this band structure is not for the atoms alone, but for the combined atom-cavity system. For example, the eigenvalue μ is actually a chemical potential rather than the band energy (for the underlying energy functional with the light adiabatically eliminated see [32]), and another difference from the linear case is that the lattice depth $s = U_0|\alpha_{ss}|^2$ is not fixed, but instead depends on the values of $\{b, q\}$. So, for example, the lattice depth changes during a BO as q is swept along the band.

The external force f breaks the spatial periodicity and means that Bloch waves are replaced by Wannier-Stark states as the stationary solutions of the equations of motion (in fact, in finite systems the Wannier-Stark states are resonances rather than true eigenstates [48]). The spatial periodicity can be restored by applying the unitary transformation $\bar{\varphi}(x,t) = \exp(-ift x)\varphi(x,t)$ which removes the fx term appearing in the hamiltonian in the Schrödinger equation (5.6b) and introduces a shift ft into the momentum operator

$$\mathcal{H} = -\frac{\partial^2}{\partial x^2} + s(t)\cos^2(x) - fx \longrightarrow \bar{\mathcal{H}} = \left(-i\frac{\partial}{\partial x} + ft\right)^2 + s(t)\cos^2(x)\ . \tag{5.10}$$

We denote the frame resulting from this transformation as the transformed frame (TF), and the original frame as the lab frame (LF).

Let us now consider the dynamics under the influence of the force term. We take the initial atomic state $\bar{\varphi}(x, t = 0) = \varphi(x, t = 0)$ to be a Bloch state in the ground band with quasimomentum $q = q_0$. In the adiabatic approximation the atoms remain in the ground band but the force causes the quasimomentum to sweep periodically through the first Brillouin zone in accordance with the Bloch acceleration theorem

$$q(t) = q_0 + ft \tag{5.11}$$

as can be seen by comparing Eqns. (5.9b) and (5.10). In fact, a careful analysis [49] shows that Eq. (5.11) holds even when adiabaticity is broken and interband transitions are allowed providing these transitions are "vertical", i.e. they conserve q.

This standard approach to BOs remains valid even when the lattice depth is modulated in time, as takes place in cavities, because amplitude modulation does not break the spatial periodicity of the potential and so cannot change q [15]. We therefore find that at any later time t, the *exact* atomic meanfield can be expressed as

$$\varphi(x,t) = \exp\left[i(q_0 + ft)x\right]\mathcal{U}(t)\ . \tag{5.12}$$

In general $\mathcal{U}(t)$ is in a superposition of bands and so is no longer the steady state solution of Eqns. (5.9a) and (5.9b), although it does retain its Bloch form. The advantage of the TF is that the

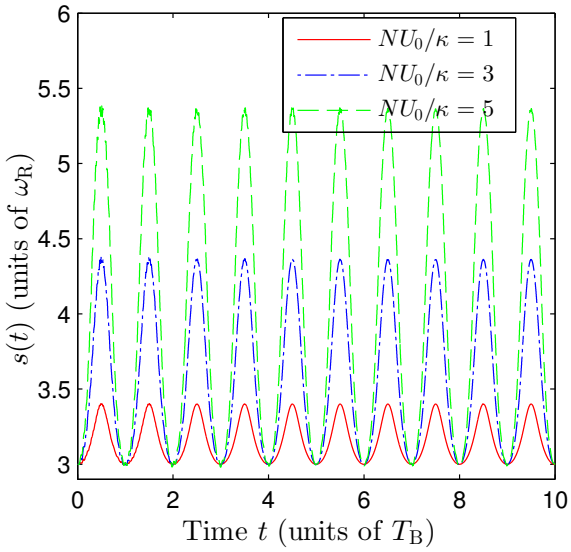

Figure 5.2. Intracavity optical lattice depth $s(t) \equiv U_0|\alpha(t)|^2$ in units of the atomic recoil frequency ω_R plotted as a function of time. The curves, which are each for a different value of the collective atom-cavity coupling parameter NU_0/κ, were obtained by solving the meanfield equations of motion Eqns. (5.6a) and (5.6b) and illustrate the fact that the change in lattice depth over one Bloch oscillation increases with NU_0/κ. In order to maintain a minimum lattice depth of $3E_R$ as NU_0/κ was increased by changing $U_0 = \{1, 3, 5\}u_0$, where $u_0 = 7 \times 10^{-3}\omega_R$, we also changed the pumping strength as $\eta = \{30.7, 24.2, 24.3\}\kappa$, giving mean photon numbers $\{458, 172, 117\}$, respectively. The other parameter values used in this plot are $\Delta_c = -0.75\,\kappa$, $\kappa = 345\,\omega_R$, and $N = 5 \times 10^4$. For all the plots in this paper the force is such that the Bloch frequency has the value $\omega_B = \omega_R/4$.

quasimomentum is frozen at its initial value and we have

$$\bar{\varphi}(x,t) = \exp\left[iq_0x\right]\mathcal{U}(t) \tag{5.13}$$

so that it is only the spatially periodic function $\mathcal{U}(t)$ that evolves in time. From the point of view of numerical computation this allows us to work with a basis of periodic functions (we normalize our wave functions over one period of the lattice). At any given time a relatively small number of basis functions can accurately describe the atomic meanfield state and this greatly reduces the numerical effort in the calculation of BOs.

By working in terms of Bloch waves, our approach is predisposed towards treating wave functions which are localized in momentum space rather than coordinate space. This choice is sensible because momentum space is a natural setting for BOs as is evident from Eq. (5.11). This is also in line with existing experiments demonstrating cold atom BOs in free space optical lattices [2, 6, 7, 8, 9, 12, 13], where the initial state is generally a fairly narrow wavepacket in momentum space. In this paper we shall therefore restrict ourselves to states that are completely localised in quasimomentum (δ-function wave packet).

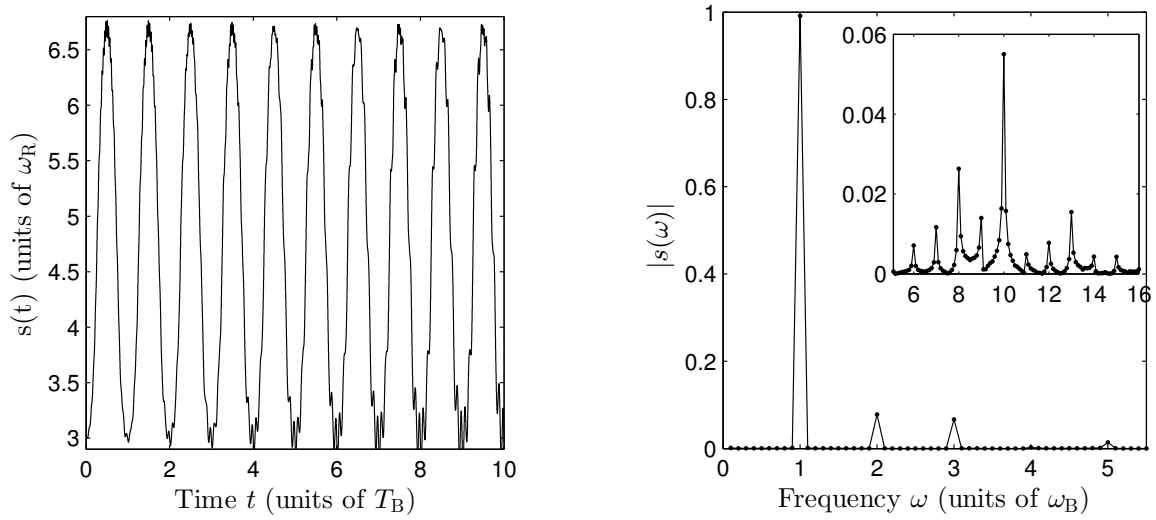

(a) Lattice depth as a function of time

(b) Fourier transform in time of lattice depth

Figure 5.3. The lattice depth $s(t)$ in units of the atomic recoil frequency ω_R is shown in (a) and its Fourier transform $s(\omega)$ is given in (b). We have increased the atom-cavity coupling from Fig. 5.2 to $NU_0/\kappa = 7.75$. At this larger value some fast fluctuations on top of the slow BO become visible. Their frequency is dominated by a harmonic at $10\,\omega_B$ as can be seen in the inset.

5.4 Meanfield dynamics: results

We now present our numerical results for the meanfield dynamics. The initial state at time $t = 0$ is taken to have quasimomentum $q = 0$, and be given by the solutions α_{ss} and $\mathcal{U}_{0,0}(x)$ of the meanfield steady state equations [Eqns. (5.9a) and (5.9b)] for atoms in the ground band. This state is propagated in time using the meanfield equations of motion [Eq. (5.6a) and Eq. (5.6b)]. The reasons for our choices for the parameter values $\{U_0, N, \eta, \Delta_c, \kappa\}$ will be explained at the end of this Section.

Under the action of the external force the atoms begin performing BOs, which for atoms in extended Bloch states gives rise to a breathing motion of the atomic density distribution on each lattice site [15]. The classical backaction imprints an oscillation on the amplitude and phase of the light field at the Bloch frequency ω_B. In Fig. 5.2 we plot the time-dependence of the intracavity lattice depth $s(t) = U_0|\alpha(t)|^2$ seen by atoms, which is proportional to the number of cavity photons $|\alpha|^2$. The experimental signature of the BOs is the photon current transmitted by the cavity, and this is given in the meanfield approximation by $\kappa|\alpha(t)|^2$, and hence is directly proportional to $s(t)$.

The size of the backaction is controlled by the collective coupling $\beta = NU_0/\kappa$, as is apparent from the different curves in Fig. 5.2. As β is increased the change in the lattice depth over a Bloch period increases and hence the visibility or *contrast* of the BOs as measured by a photon detector

outside the cavity increases also. We define the contrast ϵ as

$$\epsilon \equiv (s_{\max} - s_{\min}) / (s_{\max} + s_{\min}) . \tag{5.14}$$

Each curve in Fig. 5.2 has a different pumping strength η in order to maintain the same minimum lattice depth of $3E_{\mathrm{R}}$. If the lattice becomes too shallow interband transition rates (e.g. due to Landau-Zener tunnelling around the band edges) become so high that the atoms effectively fall out of the lattice. On the other hand, if the lattice becomes too deep the contrast decreases (see Fig. 5.9a below and also Fig. 5 in [32]). A depth of $3E_{\mathrm{R}}$ gives a reasonable compromise. Therefore, although in the rest of this paper we will examine the effects of changing the various system parameters, we will always maintain the minimum lattice depth at $3E_{\mathrm{R}}$ (except in Fig. 5.9a and Fig. 5.14). This also allows us to make comparisons between the effects of different parameter values upon, e.g. the quantum fluctuations, whilst keeping the atomic meanfield dynamics as similar as possible.

As the coupling β is increased other effects appear apart from an increase in the contrast. These effects are visible in Fig. 5.3 (see also Fig. 2 in [15]). In Fig. 5.3a we see that small-amplitude fast oscillations of the lattice depth appear on top of the basic BO. Referring to the Fourier transform of $s(t)$ plotted in Fig. 5.3b, we see that the basic BO dynamics is governed by the fundamental ω_{B} and its low lying harmonics, whereas the fast oscillations are clustered around the tenth harmonic (see inset) and include a continuum of frequencies with some peaks at half harmonics. In this context it is important to bear in mind that the band gaps change continuously in time as q is swept through the Brillouin zone and so a range of frequencies is to be expected.

The precision to which ω_{B} can be measured in the scheme proposed in this paper depends upon the contrast. From the results shown in Fig. 5.2 it may therefore seem that in order to make the most sensitive measurement possible one should choose β to be as large as possible. However, this is false for two reasons. One is the effect of quantum fluctuations due to measurement backaction which is also controlled by β and will be the focus of Section 5.8. Another reason, which enters even at the meanfield level, is the possibility of bistability in cavity photon number for large values of β (when the pumping is sufficiently large). In [28] this bistability was studied experimentally in a uniform unaccelerated condensate, which in our language has a quasimomentum $q = 0$. In [32] we studied this problem theoretically and generalized it to include finite q: we showed that bistability arises from the appearance of swallowtail loops in the bands. In the semiclassical picture of a BO the quasimomentum scans adiabatically through the entire band and so when it encounters a swallowtail loop the system can follow a branch that suddenly terminates at some later time, leading to fundamentally nonadiabatic behavior [15, 50]. Hence, in a scheme to measure BOs, it would be better to be in a parameter regime where the cavity is not bistable for any value of q. In Fig. 5.4 we plot the pump strength required to maintain the lattice depth at a minimum value of $3E_{\mathrm{R}}$ as a function of β. The red (solid) and blue (dot-dashed) lines enclose the values of η for which the steady state photon number in the cavity displays bistability for at least some values of

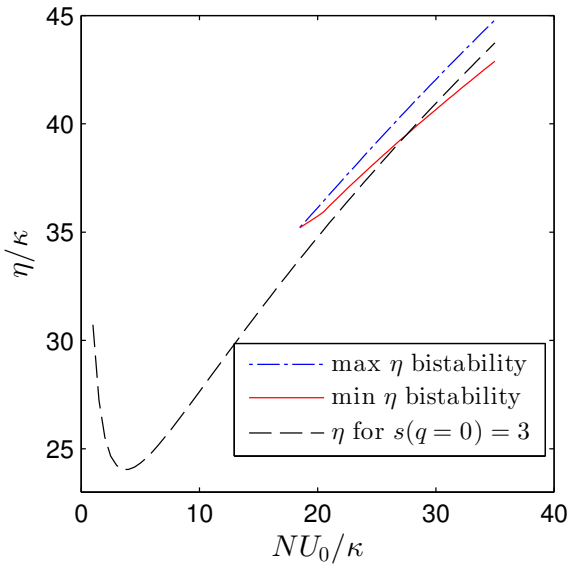

Figure 5.4. Plot of pump strength (dashed black line) required to maintain a minimum lattice depth of $3E_{\rm R}$ as a function of NU_0/κ. The red (solid) and blue (dash dotted) lines enclose the values of η for which the steady state photon number in the cavity is bistable for any value of the quasimomentum of the atomic wave function. One sees that for $NU_0/\kappa \sim 25$, the pump strength required to maintain the lattice depth leads to bistability. Other parameters for the plot are $\Delta_{\rm c} = -0.75\,\kappa$, $\kappa = 345\,\omega_{\rm R}$, $N = 5 \times 10^4$

.

the quasimomentum. We see that for β values as large as 25 (at the fixed detuning $\Delta_{\rm c} = -0.75\kappa$) one can avoid bistability and get large contrast in the lattice depth evolution.

Having emphasized that our choice for the pumping strength η is guided by the tradeoff between contrast and bistability according to Fig. 5.4, let us now explain how we chose the rest of the system parameters used in the calculations. There are three parameters we hold constant throughout this paper; the first is the cavity damping rate $\kappa = 345\,\omega_{\rm R}$ which is the value realized in the experiment [28]. As a guide to the magnitude of the atomic recoil frequency $\omega_{\rm R}$ used as the frequency unit, we note that for ^{87}Rb atoms in 780nm light $\omega_{\rm R} = 2\pi \times 3.8$ kHz. The second constant parameter is the Bloch frequency $\omega_{\rm B} = \omega_{\rm R}/4$. The gravitational force on ^{87}Rb atoms in a 780nm lattice provides a Bloch frequency very close to this value. Finally, unless specified otherwise, we keep the meanfield atom number fixed at $N = 5 \times 10^4$ and vary U_0 in order to vary β. This last choice is motivated by a scaling symmetry of the meanfield equations [Eqns. (5.6a)-(5.6b)], which also holds for the quantum operator equations [Eqns. (5.22a)-(5.22b)] below; solving the coupled equations for the set of parameters $\{U_0, N, \eta, \Delta_{\rm c}, \kappa\}$ is exactly the same as solving them for $\{U_0 r, N/r, \eta/\sqrt{r}, \Delta_{\rm c}, \kappa\}$, where r is some positive scaling factor. In both the scaled and unscaled versions the lattice depth $s(t) = U_0|\alpha(t)|^2$ is maintained at the same value. Thus, each specific calculation one performs represents a family of parameters. Our choice for N keeps the atomic density dilute enough in a typically sized cavity that the approximation of ignoring collisional atom-atom interactions remains

valid. There is some latitude in the choice of Δ_c, but the contrast one obtains at a given value of β is larger for Δ_c closer to the cavity resonance. On the other hand, one also has to make sure that the effective cavity detuning

$$\Delta_c^{\text{eff}} \equiv \Delta_c - NU_0\langle\cos^2(x)\rangle \tag{5.15}$$

is less than zero so that we are in the cavity cooling regime for the fluctuations [40] (see Section 5.6). We set $\Delta_c = -0.75\kappa$ since we find that it maximizes the contrast for the coupling value of $NU_0/\kappa = 1$. We will examine the effect of changing the number of atoms N and the minimum lattice depth when we examine the signal-to-noise ratio in Section 5.8.

5.5 Quantum Dynamics: theory

The approach we take to quantum dynamics is based upon a linearization about the meanfield solution, retaining the quantum operators $\delta\hat{a}$ and $\delta\hat{\Psi}$ only to first order in the equations of motion. This corresponds to the Bogoliubov level of approximation [51, 52], suitably generalized to describe coupled atomic and light fields. A new feature of our problem in comparison to previous linearization-based treatments of cavity-QED systems, e.g. [39, 41, 53], is that our meanfield is time-dependent because of the BOs. This means that the fluctuation modes, which must be orthogonal to the meanfield mode, also evolve in time (not just their occupations).

Linearizing about the meanfield solution may appear to be an innocent strategy, but, as is well known from the theory of Bose-Einstein condensation, care must be taken with such U(1) symmetry breaking approaches because they introduce a macroscopic (meanfield) wave function with a particular global phase at the cost of particle number conservation [54]. In particular, when performing a linearization about the condensate there is always a trivial fluctuation mode parallel to it with zero frequency (the "zero mode") which corresponds to unphysical fluctuations of the global phase. These issues are even more acute when the condensate is time-dependent and the boundary between condensate and fluctuation is further blurred [55].

The zero mode problem can be handled by only including fluctuations that are at all times orthogonal to the meanfield. We achieve this by applying the projector $\hat{P}(t)$ [55, 56]

$$\hat{P}(t) = \mathcal{I} - |\varphi(t)\rangle\langle\varphi(t)| \tag{5.16}$$

so that

$$\delta\hat{\Psi}_\perp(x,t) \equiv \hat{P}(t)\delta\hat{\Psi}(x,t) = \int dy\,[\delta(x-y) - \varphi(x,t)\varphi^*(y,t)]\,\delta\hat{\Psi}(y,t)\ . \tag{5.17}$$

One consequence of this is that the commutator between atomic fluctuations is given by [57]

$$\left[\delta\hat{\Psi}_\perp(x,t), \delta\hat{\Psi}_\perp^\dagger(y,t)\right] = \langle x|\hat{P}(t)|y\rangle = \delta(x-y) - \varphi(x,t)\varphi^*(y,t)\ . \tag{5.18}$$

Unlike the usual bosonic commutator for the fluctuation field $\delta\bar{\hat{\Psi}}$, this is time dependent.

Next, we transform the atomic fluctuation operator from the LF to the TF

$$\delta\bar{\hat{\Psi}}(x,t) = \delta\hat{\Psi}(x,t)e^{-ifkx} \tag{5.19}$$

which simplifies the calculation for the same reasons as mentioned in Section 5.3 for the meanfield. Since only "vertical" fluctuations between bands can occur, both the fluctuations and the meanfield have the same quasimomentum (which in the TF is frozen at its initial value), and so we can expand the fluctuations and meanfield in the same basis

$$\bar{\varphi}(x,t) = \sum_n c_n(t)e^{i2nx} \tag{5.20}$$

$$\delta\bar{\hat{\Psi}}_\perp(x,t) = \sum_n \delta\hat{c}_n(t)e^{i2nx}\ . \tag{5.21}$$

This makes the numerics a little easier. Note that we have set the initial quasimomentum in these equations to $q_0 = 0$ without loss of generality. Meanwhile, back in the LF, the quasimomentum evolves according to the Bloch acceleration theorem given by Eq. (5.11).

We can now write down the coupled equations of motion for the cavity and atomic fluctuation operators in the TF as

$$i\frac{d}{dt}\delta\hat{a}(t) = A(t)\delta\hat{a}(t) + \sqrt{N}U_0\alpha(t)\int dx\cos^2(x)\left[\bar{\varphi}^*(x,t)\delta\bar{\hat{\Psi}}_\perp(x,t) + \bar{\varphi}(x,t)\delta\bar{\hat{\Psi}}_\perp^\dagger(x,t)\right] + i\sqrt{2\kappa}\hat{\xi}(t) \tag{5.22a}$$

$$i\frac{\partial}{\partial t}\delta\bar{\hat{\Psi}}_\perp(x,t) = \bar{\mathcal{H}}(t)\delta\bar{\hat{\Psi}}_\perp(x,t) + \sqrt{N}U_0\hat{P}(t)\cos^2(x)\bar{\varphi}(x,t)\left[\alpha^*(t)\delta\hat{a}(t) + \alpha(t)\delta\hat{a}^\dagger(t)\right] \tag{5.22b}$$

where $A(t) \equiv \left(-\Delta_c + NU_0\langle\cos^2(x)\rangle(t) - i\kappa\right)$. The structure of these equations is such that without the Langevin term $\hat{\xi}(t)$ the operators $\delta\hat{a}$ and $\delta\bar{\hat{\Psi}}_\perp$ would be fixed at their initial values and so the quantum parts of the fields would remain zero for all time. The Langevin fluctuations appear as an inhomogeneous term in the cavity field equation and act as a source that drives the evolution of $\delta\hat{a}$ which in turn drives the evolution of $\delta\bar{\hat{\Psi}}_\perp$ via the atom-cavity coupling.

As pointed out in [41], the dynamics of the complex valued operators in the above equations can be solved either by separating out their real and imaginary parts (optomechanics approach) or by simultaneously solving the equations for the hermitian conjugates of the operators (the Bogoliubov-de Gennes approach). We choose the latter. Collecting the fluctuations into the column vector $\hat{R}(t) = \left(\delta\hat{a}\ \delta\hat{a}^\dagger\ \delta\bar{\hat{\Psi}}_\perp\ \delta\bar{\hat{\Psi}}_\perp^\dagger\right)^T$, and the noise operators that act as source terms into the column vector

$\hat{Z}(t) = \sqrt{2\kappa}\left(\hat{\xi}\ \hat{\xi}^\dagger\ 0\ 0\right)^T$, where T denotes transposition, we obtain the operator matrix equation

$$i\frac{\partial}{\partial t}\hat{R} = \mathbf{M}\hat{R}(t) + i\hat{Z}(t) \tag{5.23a}$$

with

$$\mathbf{M(t)} = \begin{bmatrix} A & 0 & \sqrt{N}U_0\alpha V^* & \sqrt{N}U_0\alpha V \\ 0 & -A^* & -\sqrt{N}U_0\alpha^* V^* & -\sqrt{N}U_0\alpha^* V \\ \sqrt{N}U_0\alpha^* W(x) & \sqrt{N}U_0\alpha W(x) & \hat{P}\ \bar{\mathcal{H}}(t) & 0 \\ -\sqrt{N}U_0\alpha^* W^\dagger(x) & -\sqrt{N}U_0\alpha W^\dagger(x) & 0 & -\hat{P}^\dagger\ \bar{\mathcal{H}}(t) \end{bmatrix} \tag{5.23b}$$

where we have introduced the operators

$$V \cdot g(x) \equiv \int dx\, \bar{\varphi}(x,t)\cos^2(x) g(x) \tag{5.23c}$$

$$W(x) \equiv \hat{P}(t)\cos^2(x)\bar{\varphi}(x,t) \tag{5.23d}$$

i.e. V is an integral operator that acts on a function $g(x)$. Since they fall on the off-diagonals, the terms involving V and W couple the cavity and atom fluctuations. Observe, however, that in the linear approximation used here the atomic fluctuation operators $\delta\bar{\hat{\Psi}}_\perp(x,t)$ are not directly coupled to the cavity fluctuation operators $\delta\hat{a}(t)$ because this would lead to terms which are of second order. Rather, the coupling between the two sets of quantum fields is mediated by the meanfields $\alpha(t)$ and $\bar{\varphi}(x,t)$.

The matrix $\mathbf{M}(t)$ is non-normal, i.e. it does not commute with its Hermitian adjoint and its left and right eigenvectors are not the same. However, it does have the following symmetry property: a linear transformation $\mathcal{T}$ that swaps the first and second, and simultaneously, the third and fourth rows, produces a matrix which is proportional to the complex conjugate of the original [40]

$$\mathcal{T}.\mathbf{M}.\mathcal{T} = -\mathbf{M}^*. \tag{5.24}$$

This symmetry, which is a general feature of Bogoliubov-de Gennes type equations [11], implies that the eigenvalues (and the associated eigenvectors) occur in pairs of the form $\pm\omega_n + i\gamma_n$ i.e. with the same imaginary parts but with real parts of opposite sign. We shall explore the spectrum of the fluctuation matrix $\mathbf{M}$ further in the Section 5.6. We also note that when written in matrix form the role of the projection operator becomes clear since one can immediately see that the vectors $(0\,0\,\bar{\varphi}(x,t)\,0)^T$ and $(0\,0\,0\,\bar{\varphi}^*(x,t))^T$ span the zero eigenvalue subspace of the matrix $\mathbf{M}$ and the trivial fluctuations live in this subspace.

The time evolution of the fluctuation operators is given by solving Eq. (5.23a). However, measurable observables are given by expectation values and correlation functions of these operators rather

than by the operators themselves. To this end we consider the covariance matrix $\mathbf{C}(t)$ associated with the vector $\hat{R}$

$$\mathbf{C}_{jk}(t) \equiv \langle \hat{R}_j \hat{R}_k \rangle(t). \tag{5.25}$$

Particular cases of $\mathbf{C}_{jk}(t)$ (or more precisely, its sum) include the total number of photonic and atomic fluctuations

$$\delta n(t) = \langle \delta\hat{a}^\dagger(t)\delta\hat{a}(t)\rangle \tag{5.26}$$

$$\delta N(t) = \int dx \langle \delta\bar{\hat{\Psi}}^\dagger_\perp(x,t)\delta\bar{\hat{\Psi}}_\perp(x,t)\rangle. \tag{5.27}$$

The latter correspond to the number of atoms excited out of the meanfield component (i.e. the atomic depletion).

To obtain the time evolution of the covariance matrix, consider the formal solution to Eq. (5.23) [58]

$$\hat{R}(t) = \mathbf{G}(t,0)\hat{R}(0) + \mathbf{G}(t,0)\int_0^t \mathbf{G}^{-1}(\tau,0)\hat{Z}(\tau)d\tau \tag{5.28}$$

where $\mathbf{G}(t)$ is a matrix satisfying:

$$\dot{\mathbf{G}}(t,0) = -i\mathbf{M}(t)\mathbf{G}(t,0)\ ; \quad \mathbf{G}(0,0) = \mathcal{I}\,. \tag{5.29}$$

We drop the dependence of $\mathbf{G}$ on the initial time for notational convenience in what follows. Inserting this formal solution in Eq. (5.25) we find

$$\mathbf{C}(t) = \mathbf{G}(t)\mathbf{C}(0)\mathbf{G}^T(t) + \mathbf{G}(t)\Sigma(t)\mathbf{G}^T(t) \tag{5.30}$$

$$\Sigma(t) \equiv \int_0^t\int_0^t \mathbf{G}^{-1}(\tau)\langle\hat{Z}(\tau)\hat{Z}(\tau')\rangle[\mathbf{G}^{-1}(\tau')]^T d\tau d\tau'. \tag{5.31}$$

Using the property of the Langevin noise terms given in Eq. (5.4c), we can simplify $\Sigma(t)$ as

$$\Sigma(t) = \int_0^t \mathbf{G}^{-1}(\tau)D[\mathbf{G}^{-1}(\tau)]^T d\tau \tag{5.32a}$$

$$D_{jk} \equiv 2\kappa\delta_{j1}\delta_{k2}. \tag{5.32b}$$

Our main numerical task is thus to solve the matrix differential equation given by Eq. (5.29). In addition, the matrix elements of $\mathbf{M}(t)$ have to be computed from the meanfields $\{\alpha(t), \bar{\varphi}(x,t)\}$ obtained by solving the coupled equations Eq. (5.6a) and Eq. (5.6b). These latter equations are simply a set of ordinary differential equations that we solve using an adaptive time-step Runge-Kutta scheme. We then solve the matrix differential equation for $\mathbf{G}(t)$ using the same time grid

as the meanfield solution. For the matrix differential equation, and the associated solution for the covariance matrix $\mathbf{C}(t)$, we can again use a Runge-Kutta algorithm or exponentiate the fluctuation matrix $\mathbf{M}(t)$ over the (small) time step intervals [59].

As a check on the results we can use the fact that the elements of the covariance matrix $\mathbf{C}(t)$ have to obey the commutator relations Eq. (5.18) for the operators making up $\hat{R}(t)$. For example, when the atomic operator is expanded as in Eq. (5.20), the expectation value of the commutator relation Eq. (5.18) gives

$$\langle \delta\hat{c}_n \delta\hat{c}_m^\dagger \rangle - \langle \delta\hat{c}_m^\dagger \delta\hat{c}_n \rangle = \delta_{nm} - \langle n|\bar{\varphi}(t)\rangle\langle\bar{\varphi}(t)|m\rangle. \tag{5.33}$$

The left hand side of this equation gives the difference between certain entries of the covariance matrix and we can calculate its expected value (the right hand side) from the meanfield solution. The degree of agreement between the two sides provides a measure of the accuracy of the fluctuation calculation. In general, we find that the accuracy can be increased by taking smaller time steps.

In closing this section, we would like to point out that the meanfield solution already includes Landau-Zener type tunnelling that causes the *coherent* excitation of higher bands. By contrast, the effect of Langevin fluctuations ξ is to *incoherently* populate different bands. Within the linear approximation used here, the depletion of the atomic meanfield by quantum excitations is not self-consistent, i.e. the meanfield is always normalized to N atoms, whatever the number of depleted atoms δN. The linearized equations are only valid when $\delta N << N$, as expected from a Bogoliubov-type approach.

5.6 Spectrum of elementary excitations

Before presenting the results of the combined meanfield and quantum dynamics (see the next section), we shall first examine the excitation spectrum of the atom-cavity system. The excitation spectrum gives insight into the dynamics, heating effects, and will also be of use in explaining resonances that affect the signal-to-noise ratio of the Bloch frequency measurement, a topic we will discuss in Section 5.9.

We first note that there are two distinct types of excitation, and hence spectra. The coupled atom-cavity band structure discussed in Section 5.3 refers to meanfield excitations which are labelled by a band index and a quasimomentum. They involve every atom and photon responding identically since, by the nature of the meanfield approximation, they are assumed to be described by a single wave function $\varphi(x,t)$ and the coherent amplitude $\alpha(t)$, respectively. On top of these, there are also elementary excitations or quasiparticles whose energies are the complex eigenvalues $\pm\omega_n + i\gamma_n$ of the matrix $\mathbf{M}(t)$ given in Eq. (5.23b). A clear description of the difference between the meanfield and the quasiparticle spectra for a BEC in a (non-cavity) optical lattice can be found in [60] and references therein. In the atom-cavity system the quasiparticles correspond to single quanta of the

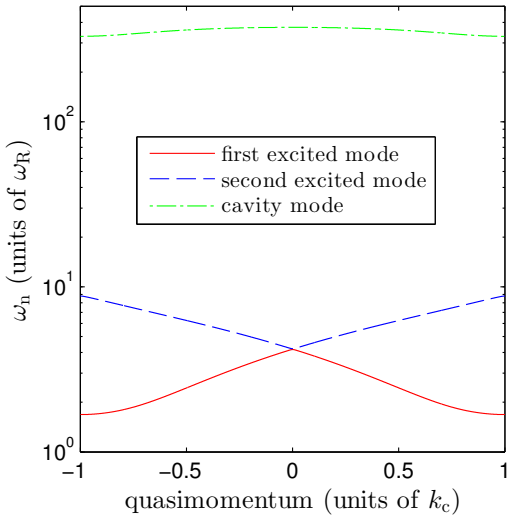

(a) Real part of the quasiparticle spectrum as a function of quasimomentum

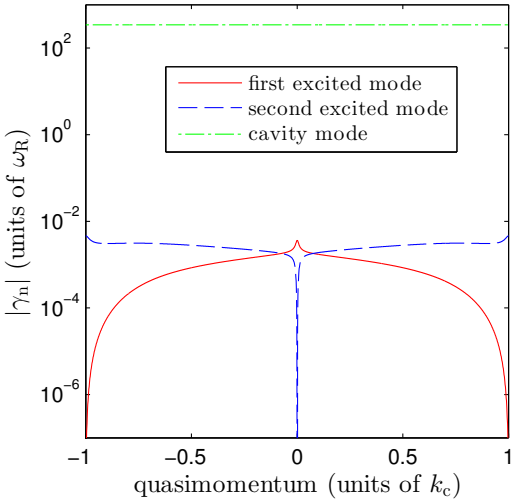

(b) Imaginary part of the quasiparticle spectrum as a function of quasimomentum

Figure 5.5. Low lying levels in the quasiparticle spectrum (elementary excitations). The frequency of the nth level is generally complex $\omega_n + i\gamma_n$. The parameters used in the plots are $U_0 = 0.01\,\omega_R$, $\kappa = 345\,\omega_R$, $\Delta_c = -0.75\,\kappa$, and $N = 5 \times 10^4$. The red (solid) and blue (dotted) lines correspond to hybridised atom-cavity modes and generally have non-zero imaginary parts except at certain special points such as at the band center and edges where they can become marginally stable and decouple from the cavity. The green (dash dotted) line corresponds to a cavity-like mode, i.e. the real part of its frequency is close to the effective detuning frequency $\Delta_c^{\text{eff}}(q)$, and the imaginary part is close to $-\kappa$.

combined fields and are thus *polaritons*. The fact that they come in pairs can be interpreted as an analogue of particles and antiparticles [11].

Whereas the meanfield band structure is always real, the quasiparticle energies have an imaginary part which comes from the leaking of the cavity field out of the cavity. If $\gamma_n < 0$, we have dynamical stability and $|\gamma_n|$ can be interpreted as the lifetime of the quasiparticle. This damping effect has potentially very important applications in cavity-assisted cooling [39, 61]. If, on the other hand, $\gamma_n > 0$ we have dynamical instability and heating.

In general, the elementary excitations have a band structure all of their own, i.e. the solutions of the Bogoliubov-de Gennes equations take the form of Bloch waves with a band index and quasimomentum that can differ from that of the meanfield solution about which we are linearizing. However, as discussed in Section 5.3, here we only allow excitations that preserve the quasimomentum (vertical transitions), and thus our quasiparticles have the same quasimomentum as their parent meanfield solution. Some examples of the quasiparticle band structure are plotted in Fig. 5.5 (see also Fig. 5.12a in Appendix 5.B).

The eigenvectors of $\mathbf{M}$ can be classified into three kinds: cavity-like modes, hybridised atom-cavity modes, and marginally stable modes [40]. The cavity-like modes (depicted by the green dash-dotted lines in Fig. 5.5) are close to being pure cavity field modes with only a small atomic component. Hence, their eigenvalues have a real part with magnitude close to the effective detuning $\Delta_{\rm c}^{\rm eff} = \Delta_{\rm c} - NU_0\langle\cos^2(x)\rangle$, and an imaginary part approximately equal to $-\kappa$. The hybridized modes (depicted by the red solid and blue dashed lines in Fig. 5.5) have some atomic and some cavity field properties, whereas the marginally stable modes are purely atomic in nature with zero cavity component. As we shall demonstrate below, the marginally stable modes occur at the points $q = 0$ and $q = \pm 1$, i.e. at the band center and edges, and their name derives from the fact that their imaginary part is zero.

The properties of the hybridised and marginally stable modes are determined by the sign of $\Delta_{\rm c}^{\rm eff}$. When $\Delta_{\rm c}^{\rm eff} < 0$ we find $\gamma_n < 0$ and we are on the cooling side of the effective resonance. On the contrary, when $\Delta_{\rm c}^{\rm eff} > 0$ we find $\gamma_n > 0$ and we are on the heating side. A calculation of the dynamics on the heating side is not stable since the linearization will fail after a short time due to the exponentially growing number of quasiparticles. Thus, the calculation of the spectra serves a very useful purpose: it guides our choice of $\Delta_{\rm c}$ so as to ensure that we are always on the cooling side of the resonance.

In Fig. 5.5a the red (solid) and blue (dashed) lines give the magnitudes of the real parts of the frequencies of the two lowest quasiparticle eigenmodes as a function of quasimomentum. The magnitudes of the imaginary parts are plotted in Fig. 5.5b. Notice that the imaginary part of one of the modes goes to zero at the band edges (red solid line) and the other goes to zero at the band center (blue dashed line). This implies that these excitations are only marginally stable at those specific values of the quasimomentum. The vanishing of the imaginary part of the frequencies at these points

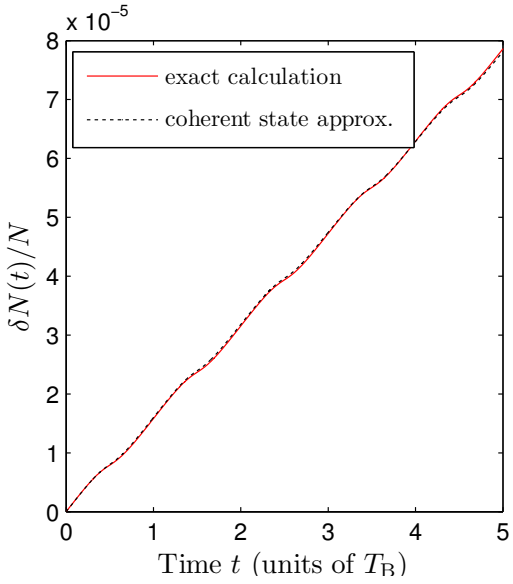

(a) Excited atom fraction versus time for $NU_0/\kappa = 0.1$

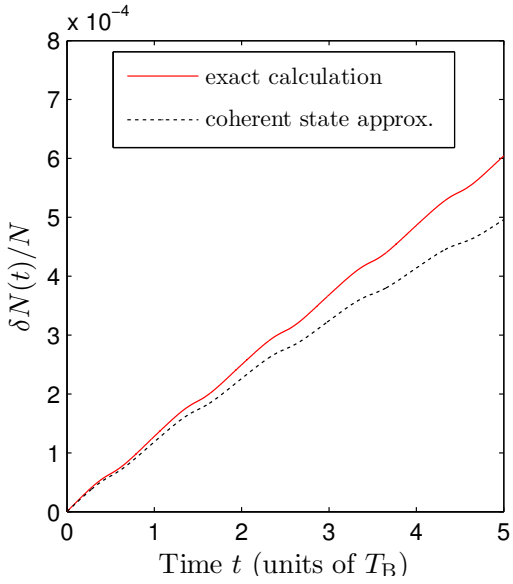

(b) Excited atom fraction versus time for $NU_0/\kappa = 1$

Figure 5.6. Growth of the excited atom fraction over five BO periods for (a) weak and (b) moderately strong atom-cavity coupling. The red (solid) curves are given by solving the full quantum problem in the form of Eq. (5.29), whereas the black (dashed) curves are the result of treating the atomic modes as independent oscillators plus assuming that the quantum fluctuations in the light come purely from vacuum shot noise, i.e. the coherent state approximation. The meanfield dynamics for (b) is given by the red (solid) curve in Fig. 5.2. The atom heating rate in these figures oscillates because it is lower at the Brillouin zone edges than at the center. Referring to Fig. 5.5 we see that at the zone edges the quasiparticle mode with the smallest real part (red solid curve) becomes marginally stable, i.e. the cavity light field part and the atomic part decouple.

can be understood as follows: a Bloch wave with $q = 0$ ($q = 1$) is even (odd) about the center of a single cell $[0, \pi]$ of the $\cos^2(x)$ potential. Since the atomic meanfield solution $\bar{\varphi}(x)$ is a Bloch wave it has well defined parity at these points. The same is also true for the atomic part of quasiparticle eigenmodes $\delta\bar{\hat{\Psi}}_\perp(x)$ [and of course $\delta\bar{\hat{\Psi}}^\dagger_\perp(x)$] of the fluctuation matrix $\mathbf{M}$, for these are also Bloch waves. In this case the integral $\int dx \bar{\varphi}^*(x) \cos^2(x) \delta\bar{\hat{\Psi}}_\perp(x)$ will sometimes vanish identically because the integrand can contain functions with opposite parity. Examination of the fluctuation matrix $\mathbf{M}$ given in Eq. (5.23b) shows that it is exactly this integral that controls the weight of the cavity part of the quasiparticle eigenmodes, and so at $q = 0, \pm 1$ we can have undamped quasiparticles with $\gamma = 0$. For other values of quasimomentum the meanfield wave function has no particular parity and there are no marginal modes.

5.7 Quantum Dynamics: results

In this section we present results from the numerical solution of the quantum equations of motion. We assume that at $t = 0$ the fluctuation fields corresponding to $\delta\hat{a}$ and $\delta\bar{\hat{\Psi}}_\perp$ are in their vacuum states and expand the atomic part in the basis given in Eq. (5.21). This allows us to construct the covariance matrix Eq. (5.25) $\mathbf{C}(t = 0)$ which we then evolve to later times using Eq. (5.29). In order to perform this task we need the fluctuation matrix $\mathbf{M}(t)$ as a function of time which in turn requires the meanfield solution $\{\bar{\varphi}(x, t), \alpha(t)\}$ as input. We therefore solve the meanfield dynamics on the same discretized time grid in parallel with the computation of Eq. (5.29).

Once we have computed $\mathbf{C}(t)$, we can use it to calculate the physical quantities of interest, such as the number of atomic excitations $\delta N(t)$, as defined in Eq. (5.27). This should not be confused with the number of quasiparticles, which are generally made up of both atomic and cavity field components. If it were not for the Langevin noise, the evolution would be perfectly coherent and δN would be zero. However, the presence of Langevin noise in the electromagnetic field generates atomic excitations via the atom-cavity coupling. In Fig. 5.6 we plot the fraction $\delta N(t)/N$ as a function of time for five Bloch periods for two different coupling values. The red (solid) curves are given by a full solution of the quantum equations, whereas the black (dashed) curves are made with a coherent state approximation for the cavity field, which will be outlined below and is discussed in more detail in Appendix 5.A. The gradient of the curves in Figs. 5.6 gives the heating rate and we note from Fig. 5.6b that the coherent state approximation slightly underestimates the true heating rate for atoms. The behaviour of $\delta N(t)/N$ over longer times (40 Bloch periods) is shown in Fig. 5.7a and the equivalent quantity for the photons is shown in Fig. 5.7b. We see that while the number of photons excited out of the meanfield saturates due to the damping by photon loss from the cavity, the atoms maintain a finite heating rate over all times we have investigated. This is curious because we are on the cooling side of the resonance [see Eq. (5.15)] all the time despite the modulations in the effective cavity detuning due to the BOs. In the inset in Fig. 5.7a we show the case without BOs, and as

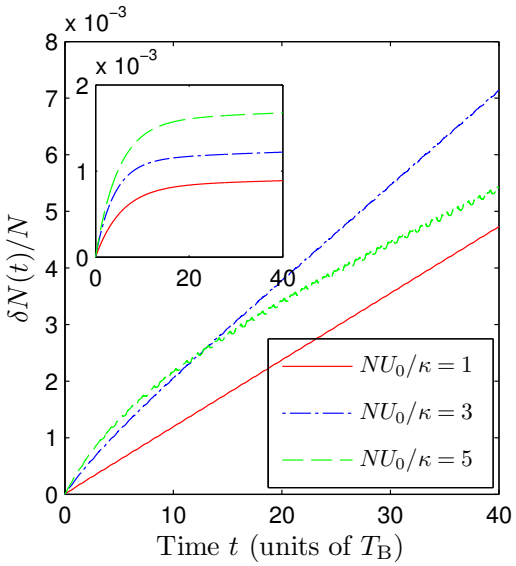

(a) Excited atom fraction versus time for different values of β.

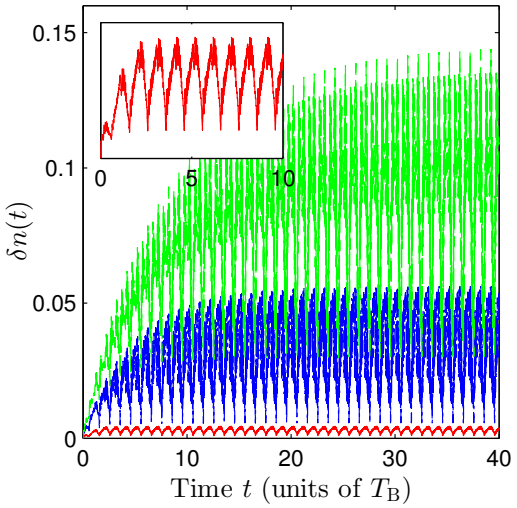

(b) Excited photon number versus time for different values of β.

Figure 5.7. Plots of (a) atomic and (b) photonic fluctuation occupation number over 40 BOs calculated using a numerical solution of Eq. (5.29). The inset in (a) shows $\delta N/N$ as a function of time for the case *without* an external force, and hence without BOs, whereas the main body of (a) shows the results with an external force: $\delta N/N$ quickly reaches a steady state in the former but not in the latter case. In (b) the lowest curve (red) is for $\beta = 1$, the middle curve (blue) is for $\beta = 3$ and the highest curve (red) is for $\beta = 5$. The inset in (b) shows a close up of the photonic fluctuation number as a function of time for $\beta = 1$. It can be seen how after a transient period the photonic fluctuation number oscillates at the Bloch period, thereby mirroring the meanfield dynamics.

can be seen, we recover the cooling. The presence of BOs clearly counteracts the cooling to some degree and prevents $\delta N(t)/N$ from reaching a steady state. This residual heating effect is analyzed in detail in Appendix 5.B, but it ultimately turns out to be due to the transport of quasiparticles to higher energy states by Landau-Zener transitions that are driven by the BOs.

In order to gain further insight into the dynamics, let us develop a semi-analytic model that we can compare against the exact results: it will allow us to see when atom-light correlations are important. The model makes two approximations: firstly we treat each eigenstate of the instantaneous meanfield Hamiltonian Eq. (5.10) as an independent oscillator mode uncoupled from the other modes, and secondly we approximate the state of the light inside the cavity as a coherent state. Coherent states have a noise spectrum that corresponds to the vacuum and so neglect correlations with the atoms. In fact, the second approximation follows naturally from the first as we show in Appendix 5.A. The results of the approximate model are the black dashed curves in Fig. 5.6. The agreement with the exact results at weak coupling ($\beta = 0.1$) is excellent, but begins to break down over time at stronger coupling ($\beta = 1$), thereby revealing the dynamic generation of correlations. In fact, as mentioned in the Introduction, the heating rate of a cloud of cold atoms inside a cavity has been measured by Murch *et al* [31], and they found it to be consistent with the predictions of vacuum noise. The new

feature in our problem is that the effective cavity drive detuning $\Delta_{\rm c}^{\rm eff}(t)$, which appears in the phase terms in Eq. (5.35), is Bloch periodic due to the meanfield dynamics.

To motivate the coherent state approximation consider the exact solution to the first order inhomogeneous differential equation for cavity field fluctuations Eq. (5.22a), which can be formally written as

$$\delta\hat{a}(t) = e^{-i\int_0^t dt' A(t')} \times \int_0^t dt' e^{i\int_0^{t'} dt'' A(t'')} [\sqrt{2\kappa}\hat{\xi}(t') - i\sqrt{N}U_0\alpha(t')\hat{X}(t')] \tag{5.34}$$

where $\hat{X}(t) \equiv \int dx\, \bar{\varphi}^*(x,t)\cos^2(x)\delta\bar{\hat{\Psi}}_\perp(t) + \text{h.c.}$, and $A(t) = -\Delta_{\rm c}^{\rm eff}(t) - i\kappa$, as above. We see that the cavity field fluctuation has two distinct contributions: the first term depends on the Langevin noise which accounts for vacuum fluctuations, whilst the second term depends on the state of the atoms. The coherent state approximation consists of dropping the latter term in favour of the former to give

$$\delta\hat{a}(t) \approx \sqrt{2\kappa}\int_0^t dt' e^{(i\Delta_{\rm c}^{\rm eff}(t)-\kappa)(t-t')}\hat{\xi}(t') \ . \tag{5.35}$$

In writing $\delta\hat{a}(t)$ in this way we have taken advantage of the fact that the cavity decay rate κ is much faster than the frequency $\omega_{\rm B}$ at which $\Delta_{\rm c}^{\rm eff}(t)$ evolves, and so the integrand is appreciable only for times $t - t' \lesssim \kappa^{-1}$ during which $\Delta_{\rm c}^{\rm eff}$ is a constant and can be evaluated at time t. The regime of validity of the coherent state approximation can be estimated from its derivation which requires $r \equiv \sqrt{N}U_0|\alpha(t)|/\sqrt{2\kappa} << 1$. Note that $r^2 = \beta s(t)/2$. In our earlier discussion (Section 5.4) of desirable parameters, we stipulated a minimum lattice depth of $s(t) \sim 3\,\omega_{\rm R}$, which implies that the validity of the coherent state approximation here is contingent upon $\beta \ll 1$, i.e. this is a weak coupling approximation.

The assumption of uncorrelated vacuum noise is a standard one in the field of cavity optomechanics [30, 62, 63, 64, 65]. The paradigmatic example is a cavity with one end mirror attached to a spring or cantilever i.e. a harmonic oscillator driven by radiation pressure. Although ultracold atoms in a very shallow lattice in a cavity can be mapped onto this system [31, 28, 41, 66, 67], that is not the case here because the atomic Bloch states do not map faithfully onto a single harmonic oscillator. Nonetheless, we have obtained our approximate model by applying a similar philosophy by mapping onto a collection of *independent* oscillators (the eigenstates of $\mathcal{H}$). The coherent state approximation for the atomic excitation occupation $\delta N(t)$ that is plotted as the black (dashed) curves in Fig. 5.6 is the sum over the occupation numbers of these independent oscillator modes $\delta N(t) = \sum_j \delta N_j(t)$. The details of the mapping are presented in the Appendix 5.A and here we shall only sketch out the main idea which is to consider the noise as a perturbation to the oscillator dynamics, and then use Fermi's golden rule to calculate the noise induced transition rates amongst each oscillator's states.

This leads to a rate equation describing the occupation number dynamics for each oscillator [63]

$$\frac{d\langle \delta N_j \rangle}{dt} = (\Gamma_{uj} - \Gamma_{dj}) \langle \delta N_j \rangle + \Gamma_{uj} \ , \tag{5.36}$$

which is Eq. (5.52) in Appendix 5.A. In this expression Γ_{uj} and Γ_{dj} are the transition rates "up" and "down" for the jth oscillator and they are proportional to $S_{\mathcal{F}\mathcal{F}}(-\omega_j)$ and $S_{\mathcal{F}\mathcal{F}}(\omega_j)$, respectively, where $S_{\mathcal{F}\mathcal{F}}(\omega)$ is the spectral density of force fluctuations (shot noise power spectrum). Thus, each oscillator is driven and damped by vacuum noise, with the rates of driving and damping being time dependent (due to the meanfield BO dynamics).

In the next two sections we examine the effects of the fluctuations upon a precision measurement, i.e. how the fluctuations put a limit on how large a value of β can be chosen for a precision measurement.

5.8 Signal-to-Noise Ratio: theory

We now explore how the inclusion of quantum noise affects the precision measurement proposal in [15]. Recall the basic idea shown schematically in Fig. 5.1: a cloud of cold atoms undergoes Bloch oscillations (e.g. due to gravity) inside a Fabry-Perot cavity, and the light field transmitted through the cavity is measured in order to determine the Bloch frequency. In order to quantify the measurement performance we will compute the signal-to-noise ratio using standard input-output theory [68].

Let us consider a double sided cavity with mirrors with matched reflectivities providing equal amplitude damping rates of $\kappa/2$. The quantum part of the input fields for both the top (driving side) and bottom (detection side) mirrors is given by the electromagnetic vacuum. Since we are not going to consider classical fluctuations of the driving laser we do not include a classical laser field contribution in the input field , but introduce it via the hamiltonian in Eq. (5.3). In our consideration of system dynamics in earlier sections we implicitly assumed a single sided cavity giving an amplitude damping rate of κ, and associated with this decay is a Langevin noise term $\sqrt{2\kappa}\hat{\xi}(t)$. In a double sided cavity we have two *independent* noise terms of the form $\sqrt{\kappa}\{\hat{\xi}_t(t), \hat{\xi}_b(t)\}$. It can be shown that the dynamics of the intracavity system (both meanfield and fluctuations) are independent of whether we assume a double sided or single sided cavity as long as we divide the net damping equally among the two mirrors (provided they have matched reflectivities). The transmitted light field is the output field at the bottom mirror which is related to the input field at the bottom mirror as

$$\hat{a}_{\rm out}(t) = -\hat{a}_{\rm in}(t) + \sqrt{\kappa}\hat{a}(t) = -\hat{\xi}_b(t) + \sqrt{\kappa}\hat{a}(t) \tag{5.37}$$

where $\hat{a}_{\rm in}$ and $\hat{a}_{\rm out}$ in this equation refer to the fields at the bottom mirror. The transmitted photon current is given by the operator $\hat{I}_{\rm out}(t) = \hat{a}^{\dagger}_{\rm out}(t)\hat{a}_{\rm out}(t)$, where again $\hat{a}_{\rm out}$ refers to the field leaving

the bottom mirror.

An experimentally straightforward method for measuring the Bloch frequency consists of recording the transmitted photon current using a photodetector. It is useful to consider the Fourier transform of the data [69]

$$\hat{N}(\omega, T) = \int_0^T dt \cos(\omega t) \hat{I}_{\rm out}(t) \tag{5.38}$$

and define the signal-to-noise ratio for the measurement as

$$\mathrm{SNR} \equiv \frac{|\langle \hat{N}(\omega, T)\rangle|^2}{\Delta N^2(\omega, T)} \tag{5.39}$$

where $\Delta N^2(\omega, T) \equiv \langle (\hat{N} - \langle \hat{N}\rangle)^2\rangle$. Thus, the SNR is the ratio of the spectral density of the photon current to its variance and provides one measure of the sensitivity of the scheme.

Let us first evaluate the SNR for a classical cavity field $\hat{a}(t) = \alpha(t)$. In this case one finds that the signal amplitude and variance are given by

$$\langle \hat{N}(\omega, T)\rangle = \kappa \int_0^T dt \cos(\omega t) |\alpha(t)|^2 \tag{5.40}$$

$$\Delta N^2(\omega, T) = \kappa \int_0^T dt \cos^2(\omega t) |\alpha(t)|^2 \,. \tag{5.41}$$

In order to obtain an approximate magnitude for the SNR we further assume that the detection rate goes as $\approx R(1 + \epsilon \cos[\omega_{\rm B} t])$ [15], where ϵ is the contrast parameter defined in Eq. (5.14). Setting the classical photon current $\kappa|\alpha(t)|^2$ in the above formulae equal to this detection rate gives

$$\mathrm{SNR}(\omega_{\rm B}, T) \approx \frac{\epsilon^2 RT}{2} \,. \tag{5.42}$$

Despite appearances, this result *does* include quantum noise to a certain degree because without the Langevin operators the variance given in Eq. (5.41) would have been zero, i.e. even when the cavity field is classical the output field contains a quantum part $\hat{a}_{\rm out} = \sqrt{\kappa}\alpha(t) - \hat{\xi}_b(t)$. Thus, the above calculation includes detector shot noise, also known as measurement imprecision [64], but neglects the effect of quantum fluctuations on the coupled dynamics inside the cavity, i.e. quantum measurement backaction. Note that this is a different approximation from the coherent state approximation used in Section 5.7, where quantum fluctuations were included in the cavity dynamics by using a Glauber coherent state, i.e. a state with vacuum noise, for the cavity field, albeit one whose fluctuations are unaffected by the presence of the atoms.

The SNR given by Eq. (5.42) predicts that the sensitivity of the scheme can be increased indefinitely by increasing the mean total number of photons collected RT and also the contrast ϵ. The former effect is the standard one expected from the general theory of measurements with un-

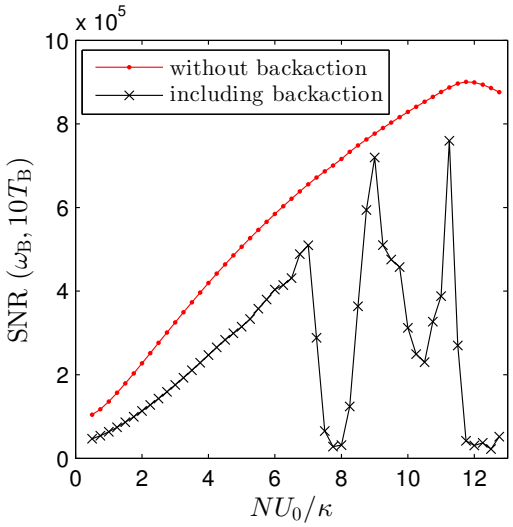

(a) Signal-to-noise ratio as a function of $\beta = NU_0/\kappa$.

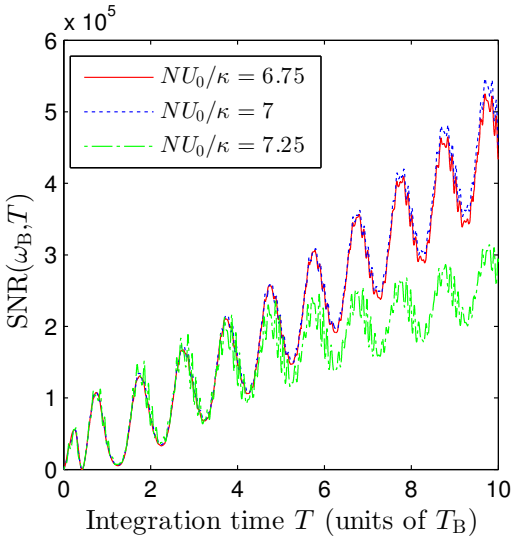

(b) Signal-to-noise ratio as a function of integration time

Figure 5.8. Plots of the SNR as a function of (a) coupling strength β, and (b) integration time T for different values of β. In (a) the SNR was computed for an integration time of 10 Bloch periods (T_B) and the red (dots) curve gives the meanfield dynamics plus detector shot noise result, whilst the black (crosses) curve includes measurement backaction, i.e. the effect of quantum fluctuations upon the coupled atom-cavity dynamics. In (b) the red (solid) and blue (dotted) curves lie almost on top of each other and correspond to values of β just before the first dip in the SNR shown in Fig. 5.8a, whereas the green (dash-dotted) curve corresponds to a value of β in the dip. For all plots the minimum lattice depth was $3E_R$. Other parameters are the typical ones mentioned in the text.

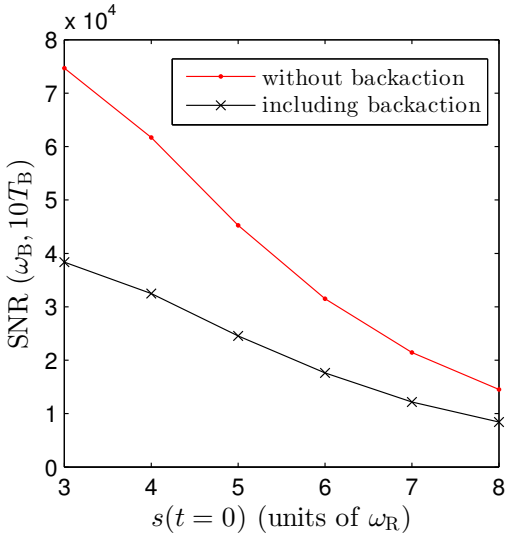

(a) Signal-to-noise ratio as a function of min. lattice depth

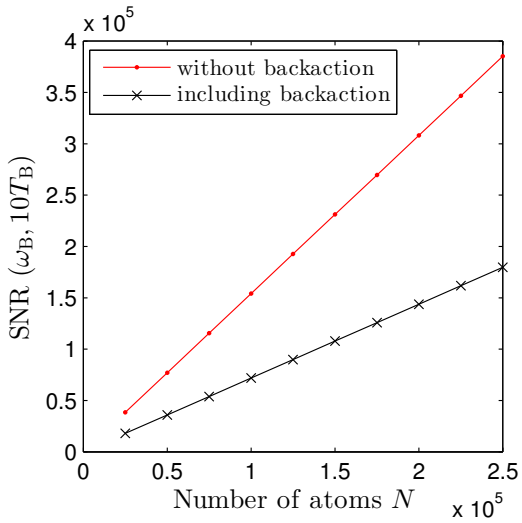

(b) Signal-to-noise ratio as a function of atom number

Figure 5.9. Plots of the SNR as a function of (a) minimum lattice depth $s(t=0)$, and (b) atom number N. In both plots the red (dots) curves were computed from meanfield theory plus detector shot noise, and the black (crosses) curves were computed including quantum measurement backaction. For all points $NU_0/\kappa = 1$ and the signal is integrated over 10 Bloch periods. In (a) it is evident that the SNR decreases in both cases for larger lattice depths. In (b) it is evident that the SNR increases linearly as a function of N in both cases.

correlated fluctuations. The latter is intuitively plausible too, but, however, can not be the whole truth because, as stated above, it neglects the effect of measurement backaction upon the dynamics which is expected to become important at larger values of β. When fluctuations are included $\hat{a}(t) = \alpha(t) + \delta\hat{a}(t)$, and the mean signal amplitude is given by

$$\langle \hat{N}(\omega, T) \rangle = \kappa \int_0^T dt \cos(\omega t) \left(|\alpha(t)|^2 + \langle \delta\hat{a}^\dagger(t) \delta\hat{a}(t) \rangle \right) . \tag{5.43}$$

In fact, this is not so very different from the meanfield photon number given by Eq. (5.40) because we are by design working in a regime where the meanfield dominates the fluctuations. However, the same is not true of the signal variance. The expression for the signal variance including fluctuations is cumbersome and is presented in Eq. (5.57) in Appendix 5.C. For present purposes it is enough to note that it includes a collection of terms that depend on integrals over two-time correlations of the photon fluctuations. These two-time correlations are challenging to evaluate numerically not only because the fluctuations occur on time scales κ^{-1} much shorter than the BOs, but also because they require the storage and manipulation of data at two times. Furthermore, the continuous driving by the BOs means that the correlations are not stationary in time, i.e. they do not just depend on $t_1 - t_2$, and this forces us to calculate the SNR in parallel to the system dynamics starting at $t = 0$. Unfortunately, due to limited computing power, we have only been able to track the SNR over ten

Bloch periods which is certainly shorter than the coherence time of the BOs for the parameters we use. An actual experiment would, of course, not suffer from this limitation and would benefit from running until the BO coherence time is reached. The main steps of our algorithm for calculating the two time correlations are provided in Appendix 5.C.

5.9 Signal-to-Noise Ratio: results

We now show how the SNR depends on the various system parameters. Due to the size of parameter space, this will not be an exhaustive study, but rather an *ad hoc* choice that nevertheless we hope is experimentally relevant. We begin by looking at the SNR as a function of the coupling parameter $\beta = NU_0/\kappa$. In Fig. 5.8a we plot the SNR evaluated at $\omega_{\rm B}$ for an integration time of 10 Bloch periods. We change β by increasing U_0 but also change η to maintain the same minimum lattice depth of $3E_{\rm R}$ throughout. The results without measurement backaction (i.e. the dynamics in the cavity is purely meanfield) are plotted by the red (dots) curve which monotonically increases until about $\beta = 12$. The initial increase of the SNR with β is in line with expectations based on Eq. (5.42). The turnover of the red curve near $\beta = 12$ is in a sense an artefact that arises from having evaluated our SNR at $\omega_{\rm B}$: it so turns out from the meanfield solution that for $\beta > 12$ the fraction of the power in the fundamental of $s(\omega)$ begins to decline and is diverted to higher harmonics. However, there is no real reason other than simplicity to only consider SNR($\omega_{\rm B}$) (any harmonic of $\omega_{\rm B}$ gives information about the applied force and inclusion of all of them in the data analysis would extract the maximum possible information from the measurement). The full calculation including measurement backaction is plotted by the black (crosses) curve. The first thing to notice is that measurement backaction always lowers the SNR. Secondly, the full SNR monotonically increases only until $\beta \approx 7$, and thereafter suffers from dramatic dips which we explain below as being due to resonances with quasiparticle excitation energies. These two observations are the main results of this paper. In Fig. 5.8b we plot the SNR as function of the total integration time T for three values of β, two before the first dip in the SNR and one in it. This plot further illustrates that for $\beta > 7$ there is a dramatic lowering of the SNR. The BO dynamics are also clearly visible due to the fact that the contrast is periodically growing and shrinking as the lattice depth grows and shrinks.

In Figs. 5.9a and 5.9b we show how the SNR depends on other parameters, namely the lattice depth and total number of atoms. In particular, in Fig. 5.9a we plot the SNR as a function of the minimum lattice depth in the cavity for the coupling value $NU_0/\kappa = 1$. The lattice depth is changed by increasing η. The red (dots) curve gives the SNR calculated using only meanfield dynamics plus the effect of shot noise at the detector and justifies the comment made in Section 5.4 that for larger lattice depth the contrast decreases. The SNR calculation including measurement backaction fluctuations is given by the black (crosses) curve, and has the same qualitative behaviour but is somewhat lower. Fig. 5.9b plots the SNR as a function of N, where for different values of N we

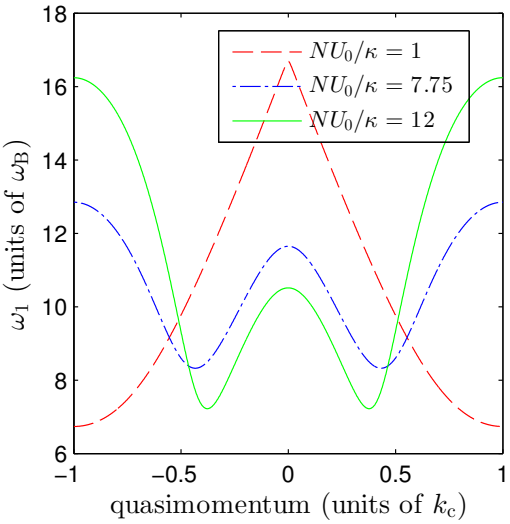

(a) Lowest excitation frequency for three different values of β

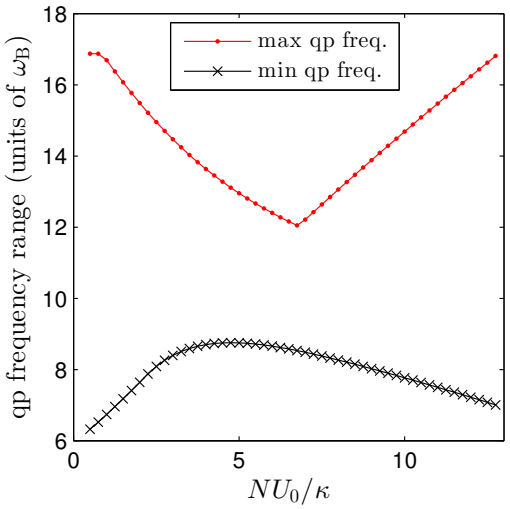

(b) Lowest excitation frequency for all q as a function of β

Figure 5.10. Plots of the lowest quasiparticle excitation frequency ω_1 about the adiabatic solution. In (a) this is given as a function of quasimomentum for three different values of β: For small β (red dashed curve) the minimum of the frequency occurs at $q = \pm 1$, but for larger values of β the minimum shifts in to smaller values of q. Since each quasiparticle excitation has an energy varying with q, in (b) we plot the range of possible excitation frequencies contained in ω_1 for all q as a function of β. The frequency units are the Bloch frequency ω_B.

keep $NU_0/\kappa = 1$ constant by scaling U_0. We also scale the pump strength η to maintain the same intracavity lattice depth $s(t)$ in all the cases. As we pointed out in Section 5.4, this method of scaling the system variables leaves the form of the meanfield and fluctuation equations unchanged. The only quantitative change is that the meanfield cavity field solution $\alpha(t)$ is scaled by the same $\sqrt{r}$ factor as the pumping. This leads to a linear scaling of the SNR as a function of N (with and without fluctuations) as shown in the plot. It is interesting to note that the rate of increase is different for the calculation including fluctuations compared to that without. Clearly there is a gain in the SNR with N.

Finally, we shall explain the physical origin of the complicated series of dips in the SNR when $\beta > 7$ that are seen in Fig. 5.8a. Consider the spectrum of quasiparticle excitations about the adiabatic meanfield solution introduced in Section 5.6. For the example shown in Fig. 5.5a, the smallest excitation frequency occurs at the band edge $q = \pm 1$ and the largest at $q = 0$. As β is increased in the usual manner (holding the minimum lattice depth constant), the q-dependence of the quasiparticle spectrum evolves, as shown for the quasiparticle mode ω_1 in Fig. 5.10a. Thus, the range of frequencies (i.e. across the entire Brillouin zone) contained in ω_1 also evolves with β and is shown in Fig. 5.10b. If the meanfield dynamics happens to contain any frequencies that fall in this range there is clearly the possibility of a resonance, exciting quasiparticles and lowering the SNR. This is exactly what happens as can be seen from Fig. 5.11 which plots the total power in the

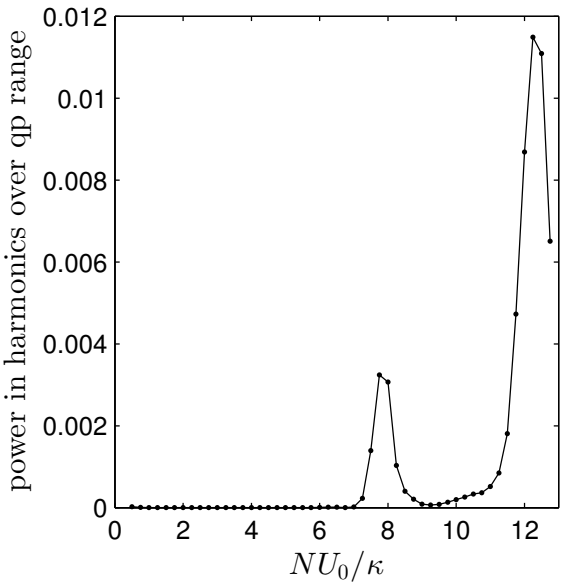

Figure 5.11. The normalized power in the harmonics of $\omega_{\rm B}$ as calculated from the Fourier transform of the meanfield solution (see Fig. 5.3b) that lies in the frequency range of the lowest quasiparticle excitation (see Fig. 5.10b).

harmonics of $\omega_{\rm B}$ that fall in the frequency range covered by ω_1. The two peaks in Fig. 5.11 at $\beta \approx 8$ and $\beta \approx 12$ coincide exactly with the dips in Fig. 5.8a. Referring back to the inset in Fig. 5.3b, which was deliberately evaluated at $\beta = 7.75$ for this very purpose, we can see the part of the meanfield spectrum that falls in the range spanned by ω_1. In the absence of BOs the quasiparticle excitation ω_1 is very narrow, with a width given by the imaginary part γ_1 evaluated at $q = 0$. However, the BO dynamics effectively broadens the resonance by orders of magnitude to that shown in Fig. 5.10b and this has a dramatic effect on the SNR.

5.10 Summary and Conclusions

In this paper we have extended our previous analysis of Bloch oscillations of ultracold atoms inside a cavity to include the effects of quantum noise in the electromagnetic field. The quantum noise originates from the open nature of the cavity and can be interpreted as a form of quantum measurement backaction because it perturbs the dynamics. The magnitude of the backaction is controlled by the dimensionless atom-light coupling parameter $\beta = NU_0/\kappa$ and we find that it can strongly affect the sensitivity of a measurement of the Bloch oscillation frequency $\omega_{\rm B}$ and therefore the determination of the magnitude of the external force F driving them.

Our treatment is based upon the coupled Heisenberg equations of motion for the atoms and light which we linearize about their meanfield solutions, i.e. a Bogoliubov level approximation. We solve the meanfield level dynamics exactly and hence coherent effects such as Landau-Zener tunneling

between bands are fully taken into account. A spectral decomposition of the meanfield solution shows that it is dominated by ω_{B} and its first few harmonics, but as β is increased spectral power begins to spread to higher frequencies.

Quantum noise is introduced via Langevin operators which act as inhomogeneous source terms in the Heisenberg equations. These terms excite quasiparticles (quantized excitations with a mixed atom-light character) out of the meanfield. In the standard situation [39, 61, 41] where there is no external force then if the system is started off with no quasiparticles their number initially grows in time but eventually saturates due to competition between cooling and heating processes (provided we are in the cooling regime $\Delta_c^{\mathrm{eff}} = \Delta_c - NU_0\langle\cos^2(x)\rangle < 0$ which means that the quasiparticle energy has a negative imaginary part). By contrast, in this work we have found that the presence of an external force, and hence BOs, profoundly changes this behaviour so that following some initial transients the heating rate settles down to a constant value even when we are nominally in the cooling regime. Nevertheless, for the parameter regimes we tested the heating rate was modest and the fraction of the atoms excited out of the coherent meanfield over the lifetime of the simulation was always less than 1% even for quite strong coupling.

In order to gain some insight into the numerical calculations we used Fermi's golden rule to develop a semi-analytic model for the heating rate in terms of a simple rate equation for the number of atomic excitations. In so doing we approximated the cavity light field by a coherent state whose quantum fluctuations are the same as those of the vacuum. This is a common approximation in cavity optomechanics but ignores the quantum correlations that build up between the atoms and the light. Comparing this with the exact numerical results for the number of atomic excitations, we infer that the field is close to a coherent state for small β, but differs from it as β is increased, as expected. Furthermore, this comparison allowed us to see the dynamic generation of atom-light correlations.

The above calculations can be applied to the estimation of the signal-to-noise ratio for a continuous measurement of ω_{B}. For example, we find that the SNR decreases with intracavity lattice depth, and increases with the number of atoms. Our principal result, however, concerns the dependence upon β. We find that the SNR can be severely reduced due to resonances between the quasiparticle spectrum and the Bloch oscillating meanfield for certain ranges of β. Indeed, the SNR behaviour depicted in Fig. 5.8 is much more complicated than that found in the standard example of a quantum limited position measurement of a harmonic oscillator, e.g. the end mirror of a resonant cavity [64]. In that system, the SNR is determined by the competition between the "measurement imprecision" (detector shot noise), which decreases with increasing measurement strength, and the measurement backaction, which increases with increasing measurement strength, and correlations between the two can be ignored to a good approximation. This leads to a smooth curve (see Fig. 5 on p.1171 of the review [64]) with a single maximum at the measurement strength where the two effects are equal. This is where the measurement should be performed for maximum sensitivity. By contrast, in our

case we have a cloud of atoms occupying Bloch states in an optical lattice and thus our system does not correspond very well to a single harmonic oscillator (except in the limit where the lattice is extremely weak so that the atoms are predominantly in a state which is uniform in space [28], but then Landau-Zener tunneling will be so severe that the atoms will quickly fall out of the lattice when the external force F is applied). Add to this the fact that our system is driven by an external force and so scans through the entire Bloch band in a time-dependent fashion, leading to the possibility of resonances, and it is not surprising that our resulting SNR in Fig. 5.8a does not have a simple maximum as a function of β. However, we can make the parameter dependent statement that it seems safest to choose $\beta < 7$ which lies below the point where the resonances set in (and for $\beta > 25$ we find optical bistability which will destroy the Bloch oscillations [32]). The resonances only occur in the calculation when quantum measurement backaction is included and so provide a salutary example of when the latter is important. Nevertheless, away from the resonances the SNR for this continuous measurement is large and is in pretty good agreement with an approximate calculation based upon purely meanfield dynamics in the cavity plus detector shot noise.

In comparison to previously studied cold atom cavity-QED systems, or even cavity optomechanical systems, a new feature of our Bloch oscillating system is the time-dependence of the meanfield. Apart from the resonances discussed above, this also has implications for the computational scheme we use to calculate the results. For example, all the fluctuation modes should be orthogonal to the meanfield mode as well as to each other, and hence they also evolve with time. Furthermore, the two-time correlation functions that are needed to calculate the signal variance that enters the SNR are not stationary in time, meaning that a large amount of data must be stored. This is especially true because the Bloch period is roughly three orders of magnitude larger than the quantum fluctuation timescale $1/\kappa$ and hence the calculation of the SNR over even a few Bloch periods is quite intensive in the regime where the coherent state approximation breaks down. In non-cavity BO experiments it has been shown that coherent dynamics can run for thousands of Bloch periods [9]. In a continuous measurement scheme, such as that proposed here, the quantum measurement backaction reduces the coherence time but unfortunately we have been unable to go much beyond ten Bloch periods with our numerical computations of the SNR and thereby find this coherence time for our scheme (we have, however, given an estimate in [15] based upon the idea that the spontaneous emission rate sets the upper limit on coherent dynamics). Nonetheless, our short time calculations illustrate quantitatively that it may be advantageous to remain at small β and integrate for longer times.

5.11 Acknowledgements

This research was funded by the Natural Sciences and Engineering Research Council of Canada. We thank A. Blais, E. A. Hinds, J. Goldwin, J. Larson, and M. Trupke for discussions related to this work and D. Nagy for helpful correspondence.

5.A Coherent State Approximation

In this appendix we provide details of how the coherent state approximation introduced in Section 5.7 can be used to derive a simple rate equation for the occupation numbers of atomic fluctuation modes. Working in the TF, consider the atomic fluctuation operator $\delta\bar{\hat{\Psi}}_\perp(t)$. Rather than expanding it in plane waves like in Eq. (5.21), let us instead expand in the instantaneous eigenbasis $\nu_k(x,t)$ of the time-dependent meanfield hamiltonian $\bar{\mathcal{H}}(t)$ [given in Eq. (5.10)]

$$\delta\bar{\hat{\Psi}}_\perp(x,t) = \sum_k \nu_k(x,t)\delta\hat{b}_k(t) \tag{5.44}$$

$$\text{where} \quad \bar{\mathcal{H}}(t)\nu_k(x,t) = E_k(t)\nu_k(x,t)\ . \tag{5.45}$$

Substituting the decomposition Eq. (5.44) into the equation of motion Eq. (5.22b) we obtain

$$\frac{d\delta\hat{b}_j(t)}{dt} = -iE_j(t)\delta\hat{b}_j(t) - \sum_k \langle\nu_j(t)|\frac{d}{dt}|\nu_k(t)\rangle\delta\hat{b}_k(t) - i\sqrt{N}U_0\left(\alpha^*(t)\delta\hat{a}(t) + \alpha(t)\delta\hat{a}^\dagger(t)\right)\langle\nu_j(t)|\hat{P}(t)\cos^2(x)|\bar{\varphi}(t)\rangle\ . \tag{5.46}$$

We see that the dynamics of the $\delta\hat{b}_j(t)$ are coupled amongst themselves: this is obvious from the second term on the right hand side, but also occurs due to the third term as can be seen from Eq. (5.34). In order to obtain a description in terms of independent oscillators the contribution from these two terms must vanish, and we will now examine when this happens.

We begin with the second term (with the time derivative) on the right hand side of Eq. (5.46). It can be shown that [70]:

$$\langle\nu_j(t)|\frac{d}{dt}|\nu_k(t)\rangle \overset{j\neq k}{=} \frac{1}{E_k(t) - E_j(t)}\langle\nu_j(t)|\frac{d\bar{\mathcal{H}}(t)}{dt}|\nu_k(t)\rangle$$

In general, contributions to the above overlap element are suppressed for states well separated in energy due to the denominator. Also, we will show below that for $k = j$ the element vanishes. Hence the dominant contribution comes from adjacent levels i.e. $k = j \pm 1$ and is given by

$$\begin{aligned}\langle\nu_j(t)|\frac{d}{dt}|\nu_{j\pm1}(t)\rangle &= \frac{1}{E_{j\pm1}(t) - E_j(t)}\langle\nu_j(t)|\frac{d\bar{\mathcal{H}}(t)}{dt}|\nu_{j\pm1}(t)\rangle \\ &= -2\frac{\omega_B}{\pi\Delta_\pm}\langle\nu_j|\hat{p}|\nu_{j\pm1}\rangle\end{aligned} \tag{5.47}$$

where the second line is obtained by taking a derivative of the instantaneous hamiltonian and realizing that, due to the opposing relative parity of adjacent states, the term in the overlap integral due to the potential is zero. The above term can be neglected if the Bloch frequency is small compared to the energy gap $\Delta_\pm$. To proceed further we will assume that this is the case but in the next appendix

we will see that this cannot be guaranteed in general. Specifically, this approximation is most likely to break down at the times when the quasimomentum comes close to the center or the edge of the Brillouin zone where there are avoided crossings. Thus, this calculation will be valid only for short times (since at longer times the system will have repeatedly gone through such crossings) and/or at parameter regimes where the gaps are large compared to Bloch frequency.

Coming back to the case when $k = j$ we have $\langle \nu_k(t)|\nu_k(t)\rangle = 1$ and so

$$\frac{d}{dt}(\langle \nu_k(t)|\nu_k(t)\rangle) = \langle \nu_k(t)|\frac{d}{dt}|\nu_k(t)\rangle + h.c. = 0$$

i.e. the derivative is purely imaginary. For the time dependent hamiltonian $\bar{\mathcal{H}}(t)$ the potential term $\cos^2(x)$ has an inversion symmetry about $x = 0$ and we can always choose the instantaneous eigenbasis $\nu_k(x,t)$ to have real coefficients when expanded over plane waves. As a result the above term goes to zero and the second term in Eq. (5.46) can be excluded.

Turning now to the third term on the right hand side of Eq. (5.46), we can see from Eq. (5.34) that it does not couple the different modes $\delta\hat{b}_j(t)$ if the light field fluctuations are independent of the atomic fluctuations i.e.

$$\delta\hat{a}(t) \approx \hat{d}(t) \equiv \sqrt{2\kappa}\int_0^t d\tau e^{-iA(t)(t-\tau)}\hat{\xi}(\tau) \tag{5.48}$$

which is exactly the coherent state approximation.

Having now seen the conditions under which the fluctuations in the instantaneous eigenmodes of $\bar{\mathcal{H}}(t)$ become independent, let us assume that these conditions are fulfilled so that the fluctuations obey the uncoupled equations of motion

$$\frac{d\delta\hat{b}_j}{dt} = -iE_j\delta\hat{b}_j(t) - u_j(t)\hat{\mathcal{F}}(t) \tag{5.49}$$

where

$$u_j(t) = i\sqrt{N}U_0\langle \nu_j(t)|\hat{P}(t)\cos^2(x)|\bar{\varphi}(t)\rangle \tag{5.50}$$

$$\text{and} \quad \hat{\mathcal{F}}(t) = \left(\alpha^*(t)\hat{d}(t) + \alpha(t)\hat{d}^\dagger(t)\right). \tag{5.51}$$

These equations describe the atomic fluctuation dynamics in terms of a collection of *independent* oscillator modes that are acted upon by the shot noise force $\hat{\mathcal{F}}(t)$. As described in [63], we can now use Fermi's golden rule to derive a rate equation for each of the oscillator occupation numbers $\delta N_j(t) = \langle \delta\hat{b}_j^\dagger\delta\hat{b}_j\rangle$

$$\frac{d\langle\delta N_j\rangle}{dt} = (\Gamma_{uj} - \Gamma_{dj})\langle\delta N_j\rangle + \Gamma_{uj} \tag{5.52}$$

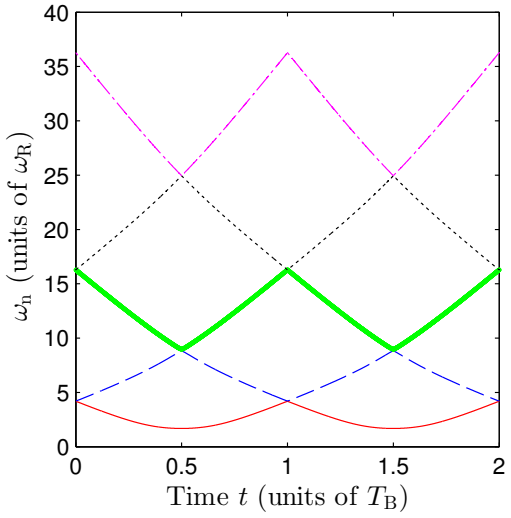

(a) Real part of quasiparticle spectrum as a function of time

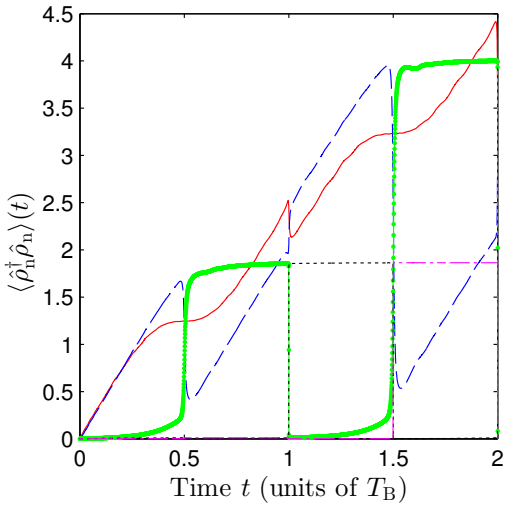

(b) Quasiparticle occupation number as a function of time

Figure 5.12. Plots of (a) the real part of the quasiparticle energy spectrum and (b) the occupation number as a function of time. The two plots are colour coded equivalently. For example, the red (solid) lowest lying level in (a) has occupation number dynamics shown by the red (solid) line in (b). Since the gaps in the spectrum in (a) are smaller than the Bloch frequency the level populations are partially exchanged at the avoided crossings: the gaps become smaller higher up in the spectrum and indeed we see that the exchanges between higher lying states are almost complete. The system parameters are the same as the case with $NU_0/\kappa = 1$ in Fig. 5.2

where the damping and diffusion rates are

$$\Gamma_{uj} = |u_j|^2 S_{\mathcal{F}\mathcal{F}}(-\omega_j); \quad \Gamma_{dj} = |u_j|^2 S_{\mathcal{F}\mathcal{F}}(\omega_j)\,.$$

These depend on the spectral density (power spectrum) of the shot noise force

$$S_{\mathcal{F}\mathcal{F}}(\omega) = \frac{2\kappa\bar{n}}{(\Delta_c^{\rm eff}+\omega)^2+\kappa^2}. \tag{5.53}$$

In the above expressions the shot noise spectrum is evaluated at the shifted oscillator frequencies defined by $\omega_j = E_j(t) - \mu(t)$ with the instantaneous chemical potential $\mu(t) = \langle\bar{\varphi}(t)|\bar{\mathcal{H}}(t)|\bar{\varphi}(t)\rangle$. This shifting helps in removing the slow time dependence of the couplings u_j (derived from the meanfield Bloch oscillations). Since the damping and diffusion rates for the different oscillators are not the same, it is in general not possible to write down an equation similar in form to Eq. (5.52) for the total $\delta N(t)$, and we have to settle instead for $\delta N(t) = \sum_j \delta N_j(t)$.

5.B Absence of cavity cooling in the presence of Bloch oscillations

In this appendix we analyze the long-time behaviour of the number of atomic fluctuations δN. We do this in order to understand the apparent absence of a cavity cooling effect in the results shown in Fig. 5.7a. In the standard case where there is no external force [40, 41], cavity cooling occurs when the effective detuning $\Delta_{\rm c}^{\rm eff} \equiv \Delta_{\rm c} - NU_0\langle\cos^2(x)\rangle$ is negative. This ensures that the quasiparticle energies have a negative imaginary part $\gamma_n < 0$ which implies dynamical stability as explained in Section 5.6. Under these circumstances δN reaches a steady state and the heating rate vanishes as shown in the inset in Fig. 5.7a. This is, however, not what we see in the presence of an external force as shown in the main body of Fig. 5.7a where the heating rate settles down to a constant nonzero value. The external force must therefore disrupt the cooling mechanism, and in this appendix we shall see that indeed the periodic driving due to the BOs drives the quasiparticles to higher energy states thereby heating the system.

The heating rate is given by the change in the occupation numbers of the various quasiparticle states as a function of time. These states are nothing but the instantaneous eigenvectors of the fluctuation matrix $\mathbf{M}(t)$ introduced in Section 5.6 [40]

$$\mathbf{M}(t)\; r^{(n)}(t) = (\omega_n(t) + i\gamma_n(t))\; r^{(n)}(t)\;, \tag{5.54}$$

and have a mixed atom-photon character. However, the fluctuation matrix $\mathbf{M}(t)$ is non-normal and so its left and right eigenvectors are not the same. The left eigenvectors $l^{(n)}$ are defined as

$$\mathbf{M}^\dagger(t)\; l^{(n)}(t) = (\omega_n(t) - i\gamma_n(t))\; l^{(n)}(t). \tag{5.55}$$

The left eigenvectors can be used to define the quasiparticle mode operator $\hat{\rho}_n(t)$ corresponding to the nth mode as

$$\hat{\rho}_n(t) \equiv \left(l^{(n)}(t), \hat{R}(t)\right) \tag{5.56}$$

where the bracket on the right in the above equation denotes a scalar product and $\hat{R}(t) = \left(\delta\hat{a}(t)\, \delta\hat{a}^\dagger(t)\, \delta\bar{\hat{\Psi}}_\perp(t)\, \delta\bar{\hat{\Psi}}^\dagger_\perp(t)\right)^T$ is the fluctuation operator in the basis of atoms and photons [see Eq. (5.23a)]. We therefore see that the required quasiparticle occupation numbers $\langle\rho_n^\dagger\rho_n\rangle(t)$ as a function of time can easily be computed from the numerical solution of the covariance matrix $\mathbf{C}(t)$ [Eq. (5.30)] once the eigenvectors $l^{(n)}(t)$ are obtained. Before we look at the results, we should first comment on the relation between the quasiparticle occupation number and the atomic fluctuation number $\delta N(t)$. As mentioned in Sec. 5.6, quasiparticle modes come in three types and the most relevant ones are the hybridized atom-light modes which have the strongest atom-light coupling and tend to lie lowest in the spectrum.

Since the hybridized modes contain both atomic and light components, their occupation number is not exactly equal to the atomic fluctuation occupation number. Nonetheless, in this system the atom-light entanglement is not very large [41] and the total quasiparticle occupation number closely tracks the atomic fluctuation number (as we have verified). Moreover, to establish a connection with the calculation in Appendix 5.A, we note that for small NU_0/κ the atomic part of the hybridised quasiparticle modes are very close to the higher band eigenstates of the instantaneous meanfield hamiltonian $\bar{\mathcal{H}}(t)$. Thus, the mode occupation of the oscillators in Appendix 5.A can be roughly mapped to the quasiparticle occupation numbers here.

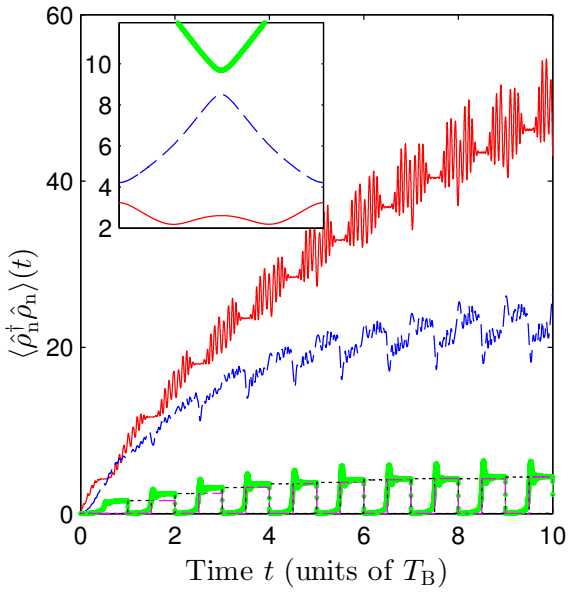

Figure 5.13. Plot of quasiparticle (qp) occupation number as a function of time when $NU_0/\kappa = 5$. The red (solid) line corresponds to the qp band with the smallest energy, followed by the blue (dashed), green (dot dashed), black (dotted) and magenta (dash dotted) lines in ascending order. The inset shows the real part of the qp energy measured in units of ω_R as a function of time over a single Bloch period T_B for the lowest three bands. Since the gap between the lowest two bands (red (solid) and blue (dashed) lines) and the rest of the spectrum is larger than the Bloch frequency, their dynamics is decoupled from the rest. System parameters are as in Fig. 5.2.

In order to understand the occupation number dynamics, consider first the real part of the quasiparticle spectrum plotted in Fig. 5.12a as a function of time for $NU_0/\kappa = 1$. The quasiparticle energy bands have avoided crossings every half Bloch period which alternate between being with the band above and below. On the scale of the plot, the gaps at the crossings are not discernible but for the present parameters it turns out that even the gap between the lowest two bands is smaller than the Bloch frequency (recall that in this paper we have set $\omega_B = 0.25\omega_R$) and the magnitude of the gaps gets smaller as we go higher up in the spectrum. During the course of Bloch oscillations these avoided crossings are repeatedly traversed at the Bloch frequency and consequently the occupation number dynamics at the avoided crossings are increasingly non-adiabatic as we go up

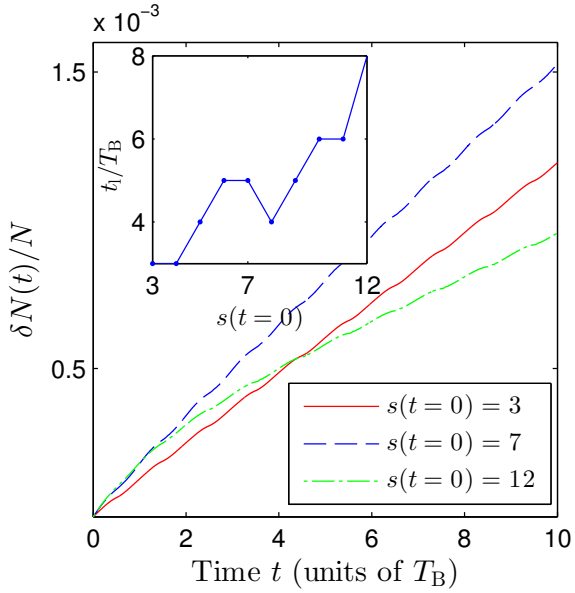

Figure 5.14. Plot of the quasiparticle occupation number as a function of time for different values of initial lattice depth at the fixed coupling value $\beta = NU_0/\kappa = 1$. The initial lattice depths $s(t=0)$ are measured in the units of ω_R and are obtained by setting the pump-strength to $\eta = \{44.2, 56.1\}\kappa$ for the blue (dashed) and green (dash dotted) curves, respectively. The inset plots the time t_l at which the linear increase in the quasiparticle number is established as a function of the initial lattice depth.

in the spectrum due to Landau-Zener transitions. For example, in Fig. 5.12a at $t = T_B/2$ the green (dot-dashed) curve of the third band approaches the blue (dashed) curve of the second band and as a result the populations of the two levels are almost completely exchanged as can be seen at the corresponding time in Fig. 5.12b. We therefore have the following picture: the occupation number of a given quasiparticle band increases either by direct scattering out of the meanfield due to quantum noise or by upcoming quasiparticles from the immediately lower band by a Landau-Zener transition. The occupation decreases due to quasiparticles scattering back into the meanfield [the hermitian conjugate term to the excitation processes in Eqns. (5.22a) and (5.22b)], or due to the finite lifetime of quasiparticles associated with cavity decay at rate κ as described by the $A(t)$ term in Eq. (5.22a), or due to Landau-Zener transitions to the next higher band. This has to be contrasted with the dynamics without BOs where the quasimomentum is fixed at $q = 0$ and the fluctuations occupy a stationary quasiparticle ladder. Without Landau-Zener transitions there is no directed transport of quasiparticles up the ladder and cooling effects, due to the finite quasiparticle lifetime $1/\gamma_n$, have time to act.

In Fig. 5.7a notice that the linear behaviour is established at later times for larger NU_0/κ. In order to understand why this happens we explore the quasiparticle number dynamics for $NU_0/\kappa = 5$ in Fig. 5.13, i.e. a factor of 5 greater than in Figs. 5.12a and 5.12b. From the inset we can immediately see that the two lowest quasiparticle bands are well isolated (by more than ω_B) from the rest of the

ladder. As a result, the occupation numbers in these modes evolves in an adiabatic manner, in contrast to the situation for $NU_0/\kappa = 1$. In fact, over the times plotted in Fig. 5.13, the blue (dashed) band reaches a steady average occupation number. But the higher quasiparticle energy levels represented, for instance, by the green (dotted) and black (dot dashed) lines have smaller gaps and behave akin to Fig. 5.12b because they are rapidly emptied by Landau-Zener transitions. Another relevant observation comes from Fig. 5.7b, where we see that the fluctuation photon number reaches its quasi-steady state around the same time as the atomic fluctuation number begins to exhibit *linear* growth. This can be understood now in the light of the above discussion since the lowest quasiparticle modes are coupled most strongly to the light field. The red (solid) band in the inset of Fig. 5.13 has two minima and demonstrates how for larger NU_0/κ the quasiparticle bands can be strongly modified from the single particle (linear) band structure.

We conclude this appendix by examining another way to control the band gaps in the quasiparticle spectrum and as a result the time taken for the linear increase behaviour (denoted by t_l henceforth) to set in. In Fig. 5.14 we plot the atomic fluctuation number as a function of time for $\beta = NU_0/\kappa = 1$ and three different initial meanfield lattice depth values that are set by the pump strength. Since the initial atomic state has $q = 0$, the initial lattice depth is the minimum lattice depth over the Bloch period. Furthermore, we are at relatively small β, and so the linear band picture holds good and one can anticipate that t_l increases with lattice depths due to the widening of band gaps. In the inset in Fig. 5.14 we plot t_l as a function of the initial lattice depth for a range of values at $NU_0/\kappa = 1$. As expected, we see a general trend of increasing t_l for larger lattice depths. We have identified t_l from the numerical simulation for atomic fluctuation number by requiring that the average change in the rate of increase of $\delta N(t)$ over a Bloch period converge to three significant figures.

5.C Two-time correlation calculation

When the intracavity light field is written as $\hat{a}(t) = \alpha(t) + \delta\hat{a}(t)$, the signal variance is given by:

$$\begin{aligned}\langle \Delta\hat{N}^2(\omega,T)\rangle = \kappa \left[\int_0^T \cos^2(\omega t)\left(|\alpha(t)|^2 + \langle \delta\hat{a}^\dagger\delta\hat{a}(t)\rangle\right) dt\right] + \\ 2\kappa^2\,\mathrm{Re}\left[\int_0^T dt_1 dt_2 \cos(\omega t_1)\cos(\omega t_2)\alpha(t_1)\alpha(t_2)\langle\delta\hat{a}^\dagger(t_1)\delta\hat{a}^\dagger(t_2)\rangle\right] \\ + \kappa^2\left[\int_0^T dt_1 dt_2 \cos(\omega t_1)\cos(\omega t_2)\alpha^*(t_1)\alpha(t_2)\langle\delta\hat{a}(t_1)\delta\hat{a}^\dagger(t_2)\rangle\right. \\ \left. + \int_0^T dt_1 dt_2 \alpha(t_1)\alpha^*(t_2)\cos(\omega t_1)\cos(\omega t_2)\langle\delta\hat{a}^\dagger(t_1)\delta\hat{a}(t_2)\rangle\right] \\ -2(\kappa)^{3/2}\,\mathrm{Re}\left[\int_0^T dt_1 dt_2 \alpha^*(t_1)\alpha(t_2)\cos(\omega t_1)\cos(\omega t_2)\langle\hat{\xi}_b(t_1)\delta\hat{a}^\dagger(t_2)\rangle\theta(t_2-t_1)\right].\end{aligned} \tag{5.57}$$

In this appendix we provide details of how we numerically compute the signal variance (and hence the SNR). The important extra computational step compared to the covariance matrix calculation in Eq. (5.29) is the evaluation of the two time correlations such as $\langle \delta\hat{a}^\dagger(t_1)\delta\hat{a}^\dagger(t_2)\rangle$. In the vector notation for the fluctuations, the two time correlations are elements of the correlation matrix $\mathbf{\Lambda}(t_1,t_2) = \langle \hat{R}(t_1)\hat{R}^T(t_2)\rangle$. The time evolution for the correlation matrix is given by:

$$i\frac{d}{dt}\mathbf{\Lambda}(t,t_0) = \mathbf{M}(t)\mathbf{\Lambda}(t,t_0) + i\langle \hat{Z}(t)\hat{R}^T(t_0)\rangle. \tag{5.58}$$

Let us consider the case when $t > t_0$. Then the last term in above equation gives a correlation between the Langevin operators at some future time t and the system fluctuation operators at t_0. Due to the delta-correlated nature of the Langevin noise this term will be zero. This means that Eq. (5.58) becomes homogeneous and we can solve it with the initial condition at $t = t_0$, $\mathbf{\Lambda}(t_0,t_0) = \mathbf{C}(t_0)$. Also note that the time evolution operator for the numerical evolution in Eq. (5.58) is same as the one for the covariance matrix [denoted by $\mathbf{G}(t)$ in Eq. (5.29)], which is an expression of the quantum regression theorem [68]. A separate computation for $t < t_0$ is not needed since they are related to the elements of $\mathbf{\Lambda}(t,t_0)$ with $t > t_0$ by complex conjugation. For example:

$$\langle \delta\hat{a}^\dagger(t_0)\delta\hat{a}(t)\rangle = \langle \delta\hat{a}(t)\delta\hat{a}^\dagger(t_0)\rangle^*.$$

We can evaluate the correlation $\langle \hat{\xi}_b(t_1)\delta\hat{a}^\dagger(t_2)\rangle$ using a similar approach as above for the time evolution of the vector $\langle \hat{\xi}_b(t_1)\hat{R}(t_2)\rangle$. In this case the initial condition for the evolution is $\langle \hat{\xi}_b(t_0)\delta\hat{a}^\dagger(t_0)\rangle = \sqrt{\kappa}/2$. Since the evolution operators for the correlation matrix and covariance matrix evolution are the same the calculation can be performed without additional computational cost. The main difficulty in computing the signal variance arises from the fact that the two time correlation functions are not stationary. As a result, in order to evaluate the integrals in Eq. (5.57) the correlation matrix needs to be computed for all values of $0 < t_1, t_2 < T$. This is the memory intensive step in the computation and we simplify the situation by performing the correlation matrix computation over a coarser grid than the one used in the numerical solution of Eq. (5.29). This is justified since we find typically the correlation matrix elements do not change significantly over the very short time steps chosen in the solution of Eq. (5.29). Moreover, for the results presented in Section 5.9, we have taken care to check that the numerical solutions converge to a value independent of the size of the coarse grid. The necessity of evaluating two-time correlators over a two dimensional time grid is the main limiting factor to the maximum integration time for the SNR calculations. Another point to bear in mind is that for β values larger than the ones that we have presented here we have found that the size of the coarse grid needs to be essentially matched with the size of the finer computational grid over which Eq. (5.29) is solved. As a result the calculation for strong coupling becomes very memory intensive indeed.

Bibliography

[1] F. Bloch, Z. Phys. **52**, 555 (1928); C. Zener, Proc. R. Soc. London, Ser. A **145**, 523 (1934).

[2] M. Ben Dahan, E. Peik, J. Reichel, Y. Castin, and C. Salomon, Phys. Rev. Lett. **76**, 4508 (1996); E. Peik, M. Ben Dahan, I. Bouchoule, Y. Castin, and C. Salomon, Phys. Rev. A **55**, 2989 (1997).

[3] S. R. Wilkinson, C. F. Bharucha, K. W. Madison, Q. Niu, and M. G. Raizen, Phys. Rev. Lett. **76**, 4512 (1996).

[4] R. Battesti, P. Cladé, S. Guellati-Khélifa, C. Schwob, B. Grémaud, F. Nez, L. Julien, and F. Biraben, Phys. Rev. Lett. **92**, 253001 (2004); P. Cladé, E. de Mirandes, M. Cadoret, S. Guellati-Khélifa, C. Schwob, F. Nez, L. Julien, and F. Biraben, ibid. **96**, 033001 (2006).

[5] I. Carusotto, L. Pitaevskii, S. Stringari, G. Modugno, and M. Inguscio, Phys. Rev. Lett. **95**, 093202 (2005).

[6] B.P. Anderson and M.A. Kasevich, Science **282**, 1686 (1998).

[7] O. Morsch, J. H. Müller, M. Cristiani, D. Ciampini, and E. Arimondo, Phys. Rev. Lett. **87**, 140402 (2001).

[8] G. Roati, E. de Mirandes, F. Ferlaino, H. Ott, G. Modugno, and M. Inguscio, Phys. Rev. Lett. **92**, 230402 (2004).

[9] G. Ferrari, N. Poli, F. Sorrentino, and G. M. Tino, Phys. Rev. Lett. **97**, 060402 (2006).

[10] S. Burger, F. S. Cataliotti, C. Fort, F. Minardi, M. Inguscio, M. L. Chiofalo and M. P. Tosi, Phys. Rev. Lett. **86**, 4447 (2001).

[11] B. Wu and Q. Niu, N. J. Phys. **5**, 104 (2003).

[12] V. V. Ivanov, A. Alberti, M. Schioppo, G. Ferrari, M. Artoni, M. L. Chiofalo, and G. M. Tino, Phys. Rev. Lett. **100**, 043602 (2008).

[13] N. Poli, F.-Y. Wang, M. G. Tarallo, A. Alberti, M. Prevedelli, and G. M. Tino, Phys. Rev. Lett. **106**, 038501 (2011).

[14] M.G. Tarallo, A. Alberti, M.L. Chiofalo, F.-Y. Wang, and G. M. Tino, arXiv:1207.2123v1

[15] B. Prasanna Venkatesh, M. Trupke, E. A. Hinds and D. H. J. O'Dell, Phys. Rev. A **80**, 063834 (2009).

[16] B. M. Peden, D. Meiser, M. L. Chiofalo, and M. J. Holland, Phys. Rev. A **80**, 043803 (2009).

[17] A. Boca, R. Miller, K. M. Birnbaum, A. D. Boozer, J. McKeever, and H.J. Kimble, Phys. Rev. Lett. **93** 233603 (2004).

[18] P. Maunz, T. Puppe, I. Schuster, N. Syassen, P. W. H. Pinkse, and G. Rempe, Phys. Rev. Lett. **94** 033002 (2005).

[19] J. Klinner, M. Lindholdt, B. Nagorny, and A. Hemmerich Phys. Rev. Lett. **96**, 023002 (2006)

[20] Y. Colombe, T. Steinmetz, G. Dubois, F. Linke, D. Hunger, and J. Reichel, Nature (London) **450**, 272 (2007).

[21] H. Mabuchi, Q. A. Turchette, M. S. Chapman, and H. J. Kimble, Opt. Lett. **21**, 1393 (1996); C. J. Hood, M. S. Chapman, T. W. Lynn, and H. J. Kimble, Phys. Rev. Lett. **80**, 4157 (1998).

[22] P. Münstermann, T. Fischer, P. W. H. Pinkse, and G. Rempe, Opt. Commun. **159**, 63 (1999); P. Münstermann, T. Fischer, P. Maunz, P. W. H. Pinkse, and G. Rempe, Phys. Rev. Lett. **82**, 3791 (1999).

[23] M. Trupke, J. Goldwin, B. Darquié, G. Dutier, S. Eriksson, J. Ashmore, and E. A. Hinds, Phys. Rev. Lett. **99**, 063601 (2007).

[24] J. Ye, D. W. Vernooy, and H. J. Kimble, Phys. Rev. Lett. **83**, 4987 (1999); C. J. Hood, T. W. Lynn, A. C. Doherty, A. S. Parkins, and H. J. Kimble, Science **287**, 1447 (2000).

[25] P. W. H. Pinkse, T. Fischer, P. Maunz, and G. Rempe, Nature (London) **404**, 365 (2000).

[26] B. Nagorny, Th. Elsässer, and A. Hemmerich Phys. Rev. Lett. **91**, 153003 (2003)

[27] S. Gupta, K. L. Moore, K. W. Murch, and D. M. Stamper-Kurn, Phys. Rev. Lett. **99**, 213601 (2007).

[28] F. Brennecke, S. Ritter, T. Donner, and T. Esslinger, Science **322**, 235 (2008); S. Ritter, F. Brennecke, K. Baumann, T. Donner, C. Guerlin and T. Esslinger, App. Phys. B **95**, 213 (2009).

[29] P. Horak, G. Hechenblaikner, K. M. Gheri, H. Stecher, and H. Ritsch, Phys. Rev. Lett. **79**, 4974 (1997); P. Domokos and H. Ritsch, Phys. Rev. Lett. **89**, 253003 (2002).

[30] F. Marquardt, J. P. Chen, A. A. Clerk, and S. M. Girvin, Phys. Rev. Lett. **99**, 093902 (2007).

[31] K. W. Murch, K. L. Moore, S. Gupta, and D. M. Stamper-Kurn, Nature Physics **4**, 561 (2008); N. Brahms, T. Botter, S. Schreppler, D. W. C. Brooks, and D. M. Stamper-Kurn, Phys. Rev. Lett. **108**, 133601 (2012).

[32] B. Prasanna Venkatesh, J. Larson, and D. H. J. O'Dell, Phys. Rev. A **83**, 063606 (2011).

[33] M. Coles and D. Pelinovsky, Studies in Applied Mathematics **128**, 300 (2012).

[34] B. Wu and Q. Niu, Phys. Rev. A **64**, 061603(R) (2001); B. Wu, R. B. Diener, and Q. Niu, ibid. **65**, 025601 (2002); B. Wu and Q. Niu, New J. Phys. **5**, 104 (2003).

[35] D. Diakonov, L. M. Jensen, C. J. Pethick, and H. Smith, Phys. Rev. A **66**, 013604 (2002); M. Machholm, C. J. Pethick, and H. Smith, ibid. **67**, 053613 (2003); M. Machholm, A. Nicolin, C. J. Pethick, and H. Smith, ibid. **69**, 043604 (2004).

[36] E. J. Mueller, Phys. Rev. A **66**, 063603 (2002).

[37] A. Smerzi, A. Trombettoni, P. G. Kevrekidis, and A. R. Bishop, Phys. Rev. Lett. **89**, 170402 (2002).

[38] W. Chen, D. S. Goldbaum, M. Bhattacharya and P. Meystre, Phys. Rev. A **81**, 053833 (2010).

[39] P. Horak and H. Ritsch, Phys. Rev. A **63**, 023603 (2001).

[40] G. Szirmai, D. Nagy, and P. Domokos, Phys. Rev. Lett. **102**, 080401 (2009).

[41] G. Szirmai, D. Nagy, and P. Domokos, Phys. Rev. A **81**, 043639 (2010).

[42] C. Maschler and H. Ritsch, Phys. Rev. Lett. **95**, 260401 (2005); I. B. Mekhov, C. Maschler and H. Ritsch, Nat. Phys.**3**, 319 (2007); C. Maschler, I. B. Mekhov, and H. Ritsch, Euro. Phys. J. D **46**, 545 (2008).

[43] J. Larson, B. Damski, G. Morigi, and M. Lewenstein, Phys. Rev. Lett. **100**, 050401 (2008); J. Larson, S. Fernandez-Vidal, G. Morigi, and M. Lewenstein, New J. Phys **10**, 045002 (2008).

[44] M. Gustavsson, E. Haller, M. J. Mark, J. G. Danzl, G. Rojas-Kopeinig, and H.-C. Nägerl, Phys. Rev. Lett. **100**, 080404 (2008).

[45] L. Zhou, H. Pu, H. Y. Ling, and W. Zhang, Phys. Rev. Lett. **103**, 160403 (2009).

[46] R. Mottl *et al.*, Science **336**, 1570 (2012).

[47] F.W.J. Olver *et al.* (Eds), *NIST Handbook of Mathematical Functions* (C.U.P., Cambridge, 2010).

[48] M. Glück, A. R. Kolovsky, H. J. Korsch, Phys. Rep. **366**, 103 (2002).

[49] H. Kroemer, Am. J. Phys. **54**, 177 (1986).

[50] B. Wu and Q. Niu, Phys. Rev. A **61**, 023402 (2000).

[51] C. J. Pethick and H. Smith, *Bose Einstein Condensation in Dilute Gases*, 2nd ed. (Cambridge University Press, Cambridge, 2008).

[52] L. P. Pitaevskii and S. Stringari, *Bose-Einstein Condensation* (Oxford University Press, New York, 2003).

[53] S. K. Steinke and P. Meystre, Phys. Rev. A **84**, 023834 (2011).

[54] M. Lewenstein and L. You, Phys. Rev. Lett. **77**, 3489 (1996).

[55] Y. Castin and R. Dum, Phys. Rev. Lett. **79**, 3553 (1997); Y. Castin and R. Dum, Phys. Rev. A **57**, 3008 (1998).

[56] S. A. Gardiner, D. Jaksch, R. Dum, J. I. Cirac, and P. Zoller, Phys. Rev. A **62**, 023612 (2000).

[57] A. Fetter, Annals of Physics **70**, 67 (1980).

[58] J-Q. Liao and C. K. Law, Phys. Rev. A **83**, 033820 (2011).

[59] C. F. Van Loan, IEEE Transactions on Automatic Control **23**, 395 (1978).

[60] M. Krämer, C. Menotti, L. Pitaevskii, and S. Stringari, Eur. Phys. J. D **27**, 247 (2003).

[61] S. A. Gardiner, K. M. Gheri, and P. Zoller, Phys. Rev. A **63**, 051603(R) (2001).

[62] V. B. Braginsky, *Measurement of Weak Forces in Physics Experiments* (Univ. of Chicago Press, Chicago, 1977); V. B. Braginsky, Y. I. Vorontsov, K. S. Thorne, Science **209**, 547 (1980).

[63] F. Marquardt, A. A. Clerk and S. M. Girvin, J. Mod. Opt. **55**,3329 (2008).

[64] A. A. Clerk, M. H. Devoret, S. M. Girvin, F. Marquardt, and R. J. Schoelkopf, Rev. Mod. Phys. **82**,1155 (2010).

[65] A. A. Clerk, F. Marquardt, and J. G. E. Harris, Phys. Rev. Lett. **104**, 213603 (2010).

[66] T. P. Purdy, D. W. C. Brooks, T. Botter, N. Brahms, Z.-Y. Ma, and D. M. Stamper-Kurn, Phys. Rev. Lett. **105**, 133602 (2010).

[67] D. Nagy, P. Domokos, A. Vukics and H. Ritsch, Eur. Phys. J D **55**, 659 (2009).

[68] D. F. Walls and G. J. Milburn, *Quantum Optics*, 2nd Edition, (Springer, Berlin, 2008).

[69] B. M. Peden, Ph.D. Thesis, University of Colorado (2010).

[70] A. Bohm, *Quantum Mechanics Foundations and Applications*, (Springer Verlag, Berlin, 2001).

Chapter 6

Conclusion

One unique advantage of ultracold atoms research is the ability to engineer many ideal quantum mechanical situations in a highly controllable manner. Thus, phenomena that are hard to observe in conventional situations such as Bloch oscillations of electrons in a metal subject to uniform electric field are routinely realised in the cold atoms. In a metal defects and impurities cause quick dephasing of the Bloch oscillations (BOs) whereas in the cold atoms experiments coherence times can extend to many thousands of oscillations [36, 39]. One drawback with the cold atoms BO experiments in optical lattices performed so far is the measurement protocol. BOs are interrupted at many time instants by destructively imaging the atomic cloud to measure the momentum distribution as a function of time. Moreover, following each measurement the initial conditions have to be recreated as faithfully as possible in order to obtain the same dynamics. In the proposal that we introduced in Chapter 3 and discussed extensively in the rest of the thesis, the periodic lattice potential is provided by the standing wave inside an optical cavity. The strong atom-light coupling that can be realised in cQED means the atoms exert a significant backaction on the cavity light field. As a result the atomic dynamics can be probed by measuring the light escaping out of the cavity. This is the main message of the first paper that was presented in Chapter 3 of the thesis. As we emphasized in the introductory section in Chapter 5, current state of the art experiments in cQED have already demonstrated the basic tools required to implement our proposal. This includes experiments where single atoms have been detected in a cavity [50, 52, 66], and their dynamics followed in real time [53, 54, 55]. The collective dynamics of ultracold atomic gases have also been tracked using cavities [69, 82, 79]. Thus, we hope that our theoretical proposal will be implemented in the near future in an experiment.

In the second paper presented in this thesis (Chapter 4), we considered multistability in cQED, where a given set of experimental parameters can yield more than one possible steady configuration for the cavity field and atomic wavefunction as a function of quasimomentum. From the point of view of the atoms we can draw an analogy to the case of BECs in optical lattices. There the contact

interaction can be tuned [102, 103] to yield multistable solutions which lead to characteristic loop shapes for the band energy as a function of quasimomentum. In the atom-cavity system we do not include contact interactions. Hence, we understand the multistable solutions as a manifestation of the nonlinearity due to the effective mutual interaction due to the atoms being coupled to a common cavity mode. This induced interaction has attracted a lot of attention in the last few years [86, 84, 87, 100] not least because it can be made very strong and lead to interesting many-body states in the atom-cavity system [98, 99]. This is a very active and open area of current research. We have also gone beyond simply finding such multistable solutions and have employed the general tool of catastrophe theory to organize and classify the different possibilities. The presence of loops in the band can lead to a breakdown of adiabaticity and hence disrupt the Bloch oscillations. In this manner we have used lessons learnt from this work in guiding parameter choices for the Bloch oscillation measurement proposal in Chapter 5(see Sec. 5.4).

In Chapters 3 and 4 we adopted a meanfield description for the light field and atoms. In Chapter 5 we focused on the dynamics of linear fluctuations about the time-dependent meanfield solutions to the cavity Bloch oscillation problem. One important result we found was that the inclusion of the force term modifies the damping rate of the fluctuations in comparison with the force free situation. However, our main result was the computation of the signal-to-noise ratio (SNR), including fluctuations, for short integration times. At large values of NU_0/κ one might have expected the SNR to increase due to the increased contrast of the mean intracavity photon number. On the contrary, we found that when fluctuations are included, resonances between the quasiparticle spectrum and harmonics of the Bloch frequency can lead to a lowering of the SNR. Hence we concluded that it may be a wiser strategy to stay at smaller NU_0/κ and integrate for longer times. Since the system is continuously driven by the Bloch oscillations, the correlations between the different fluctuation operators do not reach a steady state and this makes the calculation of the SNR numerically intensive. As part of our future research we would like to devise a method to circumvent this numerical issue. Since the SNR is sensitive to the parametric resonances between the quasi-particle spectrum and harmonics of the Bloch frequency we will also look into the prospects for actually using this for precision measurements.

In this thesis we have explored a few facets of the cold atoms-cavity quantum electrodynamics paradigm, which is fast emerging as an active field of research [100]. Two of the most interesting features of current research in cold atoms physics are: ability to experimentally create various interesting many body hamiltonians [23] and study the real time dynamics of a variety of systems [113]. In the different topics considered in this thesis, although we have not explicitly mentioned these aforementioned themes, we have developed some useful insights that will enable us to contribute to these topics in the future.

Bibliography

[1] M. H. Anderson, J. R. Ensher, M. R. Mathhews, C. E. Wieman, and E. A Cornell, Science **269**, 198 (1995)

[2] K. B. Davis, M. O. Mewes, M. R. Andrews, N. J. van Druten, D. S. Durfee, D. M. Kurn, and W. Ketterle, Phys. Rev. Lett **75**, 3969 (1995)

[3] I. Bloch, Science **319**, 1202 (2008)

[4] J. M. Raimond, M. Brune, and S. Haroche, Rev. Mod. Phys. **73**, 565 (2001).

[5] S. Bose, Z. Phys. **26**, 178 (1924).

[6] A. Einstein, Sitzungsber. K. Preuss. Akad. Wiss., Phys. Math. Kl. **3** (1925)

[7] A. Ashkin, Phys. Rev. Lett. **24**,156 (1970)

[8] D. J. Wineland, R. E. Drullinger, and F. L. Walls,Phys. Rev. Lett. **40**,1639 (1978)

[9] W. D. Phillips and H. Metcalf, Phys. Rev. Lett. **48**, 596 (1982)

[10] W. Paul, Rev. Mod. Phys. **62**, 531 (1990)

[11] S. Chu, L. Hollberg, J. E. Bjorkholm, A. Cable, and A. Ashkin **55**, 48 (1985)

[12] J. P. Gordon and A. Ashkin, Phys. Rev. A **21**, 1606 (1980)

[13] R. Grimm, M. Weidemüller, and Y.B.Ovchinnikov,Adv. At. Mol. Opt. Phys. **42**,95 (2000)

[14] E. L. Raab, M. Prentiss, A. Cable, S. Chu, and D. E. Pritchard, Phys. Rev. Lett. **59**, 2631 (1987)

[15] J. Dalibard and C. Cohen-Tannoudji, J. Opt. Soc. Am. B **6**, 2023 (1989)

[16] C. Cohen-Tannoudji, Rev. Mod. Phys. **70**, 707 (1998)

[17] S. Chu, Rev. Mod. Phys. **70**, 685 (1998)

[18] W. D. Phillips, Rev. Mod. Phys. **70**, 721 (1998)

[19] H. F. Hess, Phys. Rev. B **34**, 3476 (1986)

[20] E. A. Cornell and C. Wieman, Rev. Mod. Phys. **74**, 875 (2002)

[21] W. Ketterle,Rev. Mod. Phys. **74**, 1131 (2002)

[22] U. of . Innsbruck., *Atom traps worldwide*, http://www.uibk.ac.at/exphys/ultracold/atomtraps.html

[23] I. Bloch, J. Dalibard, and W. Zwerger, Rev. Mod. Phys. **80**, 885 (2008)

[24] S. Giorgini, L. P. Pitaevskii, and S. Stringari, Rev. Mod. Phys. **80**,1215 (2008)

[25] C. Zener,Proc. R. Soc. A **145**, 523 (1934)

[26] F. Bloch,Z. Phys. **52**, 555 (1928)

[27] J. Feldmann, K. Leo, J. Shah, D. A. B. Miller, J. E. Cunningham, T. Meier, G. von Plessen, A. Schulze, P. Thomas, and S. Schmitt-Rink, Phys. Rev. B **46**, 7252 (1992); C. Waschke, H. G. Roskos, R. Schwedler, K. Leo, H. Kurz, and K. Khler, Phys. Rev. Lett.**70**, 3319 (1993)

[28] J. P. Reynolds and M. Luban, Phys. Rev. B **54**, R14301 (1996)

[29] M. Ben Dahan, E. Peik, J. Reichel, Y. Castin, and C. Salomon, Phys. Rev. Lett. **76**, 4508 (1996); E. Peik, M. BenDahan, I. Bouchoule, Y. Castin, and C. Salomon, Phys. Rev. A **55**, 2989 (1997).

[30] B. P. Anderson and M. A. Kasevich, Science **282**, 1686(1998)

[31] O. Morsch, J. H. Mller, M. Cristiani, D. Ciampini, and E. Arimondo,Phys. Rev. Lett. **87**, 140402 (2001)

[32] G. Roati, E. de Mirandes, F. Ferlaino, H. Ott, G. Modugno, and M. Inguscio, Phys. Rev. Lett. **92**, 230402 (2004)

[33] R. Battesti, P. Cladé, S. Guellati-Khélifa, C. Schwob, B. Grémaud, F. Nez, L. Julien, and F. Biraben, Phys. Rev. Lett. **92**, 253001 (2004)

[34] P. Cladé, E. de Mirandes, M. Cadoret, S. Guellati-Khélifa, C. Schwob, F. Nez, L. Julien, and F. Biraben, Phys. Rev. Lett. **96**, 033001 (2006)

[35] I. Carusotto, L. Pitaevskii, S. Stringari, G. Modugno, and M. Inguscio, Phys. Rev. Lett. **95**, 093202 (2005)

[36] G. Ferrari, N. Poli, F. Sorrentino, and G. M. Tino, Phys. Rev. Lett. **97**, 060402 (2006)

[37] A. Alberti, G. Ferrari, V. V. Ivanov, M. L. Chiofalo and G. M. Tino, NJP **12**, 065037 (2010)

[38] M. G. Tarallo, A. Alberti, N. Poli, M. L. Chiofalo, F.-Y. Wang, and G. M. Tino, Phys. Rev. A **86**, 033615 (2012)

[39] M. Gustavsson, E. Haller, M. J. Mark, J. G. Danzl, G. Rojas-Kopeinig, and H.-C. Nägerl, Phys. Rev. Lett. **100**, 080404 (2008)

[40] B. P. Venkatesh, Masters Thesis, McMaster University (2008).

[41] B. M. Breid, D. Witthaut and H. J. Korsch, NJP **8**, 110 (2006); F. Dreisow, A. Szameit, M. Heinrich, T. Pertsch, S. Nolte, A. Tünnermann, and S. Longhi, Phys. Rev. Lett. **102**, 076802 (2009)

[42] E. M. Purcell, Phys. Rev. **69**, 681 (1946).

[43] P. Goy, J. M. Raimond, M. Gross, and S. Haroche, Phys. Rev. Lett **50**, 1903 (1983)

[44] D. J. Heinzen, J.J. Childs, J. E. Thomas,and M. S. Feld, Phys. Rev. Lett **58**, 1320 (1987)

[45] D. J. Heinzen and M. S. Feld, Phys. Rev. Lett **59**, 2623 (1987)

[46] P. Pinkse and G. Rempe, Chapter 13, Experimental methods in the physical sciences **40** 255-295 (edited by Roger van Zee and Patrick Looney), Elsevier Science (2002).

[47] G. Rempe, Ann. Phys. **9**,843 (2000)

[48] M. Brune, F. Schmidt-Kaler, A. Maali, J. Dreyer, E. Hagley, J. M. Raimond, and S. Haroche, Phys. Rev. Lett. **76**, 1800 (1996)

[49] M. Brune, E. Hagley, J. Dreyer, X. Maître, A. Maali, C. Wunderlich, J. M. Raimond, and S. Haroche, Phys. Rev. Lett. **77**, 4887 (1996)

[50] H. Mabuchi, Q. A. Turchette, M. S. Chapman, and H. J. Kimble, Opt. Lett. **21**, 1393 (1996)

[51] C. J. Hood, M. S. Chapman, T. W. Lynn, and H. J. Kimble, Phys. Rev. Lett **80**, 4157 (1998)

[52] P. Münstermann, T. Fischer, P. Maunz, P. W. H. Pinkse, and G. Rempe, Phys. Rev. Lett. **82**, 3791 (1999)

[53] J. Ye, D. W. Vernooy, and H. J. Kimble, Phys. Rev. Lett. **83**, 4987 (1999)

[54] C. J. Hood, T. W. Lynn, A. C. Doherty,A. S. Parkins,and H. J. Kimble, Science **287**, 1447 (2000)

[55] P. W. H. Pinkse, T. Fischer, P. Maunz, and G. Rempe, Nature **404**, 365 (2000)

[56] D. Schrader, S. Kuhr, W. Alt, M. Müller, V. Gomer, and D. Meschede, Appl. Phys. B **73**, 819 (2001)

[57] J. A. Sauer, K. M. Fortier, M. S. Chang, C. D. Hamley, and M. S. Chapman,Phys. Rev. A **69**, 051804(R) (2004)

[58] S. Nußmann, M. Hijlkema, B. Weber, F. Rohde, G. Rempe, and A. Kuhn, Phys. Rev. Lett. **95**, 173602 (2005)

[59] T. W. Mossberg, M. Lewenstein, and D. J. Gauthier, Phys, Rev. Lett. **67**, 1723 (1991)

[60] J. I. Cirac, M. Lewenstein, and P. Zoller, Phys, Rev. A **51**, 1650 (1995)

[61] P. Horak, G. Hechenblaikner, K. M. Gheri, H. Stecher, and H. Ritsch, Phys. Rev. Lett. **79**, 4974 (1997)

[62] G. Hechenblaikner, M. Gangl, P. Horak, and H. Ritsch, Phys. Rev. A. **58**, 3030 (1998)

[63] V. Vuletić and S. Chu, Phys. Rev. Lett. **84**, 3787 (2000)

[64] P.Domokos and H.Ritsch, J. Opt. Soc. Am. B **20**, 1098 (2003)

[65] P. Maunz, T. Puppe, I. Schuster, N. Syassen, P. W. H. Pinkse, and G. Rempe, Nature Physics **428**, 20 (2004)

[66] M. Trupke, J. Goldwin, B. Darquié, G. Dutier, S. Eriksson, J. Ashmore, and E. A. Hinds, Phys. Rev. Lett. **99**, 063601 (2007).

[67] Benjamin L. Lev, András Vukics, E. R. Hudson, B. C. Sawyer, P. Domokos,H. Ritsch,and J. Ye, Phys. Rev. A **77**, 023402 (2008)

[68] P. Münstermann, T. Fischer, P. Maunz, P. W. H. Pinkse, and G. Rempe, Phys. Rev. Lett. **84** (2000)

[69] B. Nagorny, Th. Elsässer, and A. Hemmerich, Phys. Rev. Lett **91**, 153003 (2003)

[70] Th. Elsässer, B. Nagorny, and A. Hemmerich, Phys. Rev. A **69**, 033403 (2004)

[71] M. Gangl and H. Ritsch, Phys. Rev. A **61**, 011402R (1999)

[72] P. Horak and H. Ritsch, Phys. Rev. A **64**, 033422 (2001)

[73] P. Domokos and H. Ritsch, Phys. Rev. Lett. **89**,253003 (2002)

[74] A. T. Black, H. W. Chan and V. Vuletic, Phys. Rev. Lett. **91**,203001 (2003)

[75] J.K.Asbóth, P. Domokos, H. Ritsch, and A. Vukics, Phys. Rev. A **72**, 053417 (2005)

[76] D. Kruse, C. von Cube, C. Zimmermann, and Ph. W. Courteille, Phys. Rev. Lett. **91**, 183601 (2003)

[77] S. Slama, G. Krenz, S. Bux, C. Zimmermann, and Ph. W. Courteille, Phys. Rev. Lett. **75**, 063620 (2007)

[78] P. Horak, S. M. Barnett and H. Ritsch, Physical Review A **61**, 033609(2000)

[79] F. Brennecke, T. Donner, S. Ritter, T. Bourdel, M. Khl, and T. Esslinger, Nature **450**, 268-271 (2007); F. Brennecke, S. Ritter, T. Donner, and T. Esslinger, Science **322**, 235 (2008); S. Ritter, F. Brennecke, K. Baumann, T. Donner, C. Guerlin and T. Esslinger, App. Phys. B **95**, 213 (2009).

[80] T. J. Kippenberg and K. J. Vahala, Opt. Exp. **15**,17172 (2007)

[81] H. M. Gibbs, S. L. McCall, and T. N. C. Venkatesan, Phys. Rev. Lett. 36, 1135 (1976).

[82] S. Gupta, K. L. Moore, K. W. Murch, and D. M. Stamper-Kurn, Phys. Rev. Lett. **99**, 213601 (2007).

[83] K.W. Murch, K. L.Moore, S.Gupta, and D. M.Stamper-Kurn, Nature Physics **4**, 561 - 564 (2008)

[84] K. Baumann, C. Guerlin, F. Brennecke, and T. Esslinger, Nature **464**, 1301(2010).

[85] D. Nagy, G. Szirmai, and P. Domokos, Eur. Phys. J. D **48**, 127 (2008)

[86] D. Nagy, G. Kónya, G. Szirmai, and P. Domokos, Phys. Rev. Lett. **104**, 130401 (2010)

[87] R. Mottl, F. Brennecke, K. Baumann, R. Landig, T. Donner, and T. Esslinger, Science **336**, 1570 (2012)

[88] D. Jaksch, C. Bruder, J. I. Cirac, C. W. Gardiner, and P. Zoller, Phys. Rev. Lett. **81**, 3108 (1998)

[89] M. Greiner, O. Mandel, T. Esslinger, T. W. Hänsch, and I. Bloch, Nature **415**, 39 (2002)

[90] J. Larson, B. Damski, G. Morigi, and M. Lewenstein, Phys. Rev. Lett. **100**, 050401 (2008); J. Larson, S. Fernandez-Vidal, G. Morigi, and M. Lewenstein, New J. Phys **10**, 045002 (2008).

[91] W. Chen, K. Zhang, D. S. Goldbaum, M. Bhattacharya, and P. Meystre, Phys. Rev. A **80**, 011801(R) (2009)

[92] W. Chen, D. S. Goldbaum, M. Bhattacharya, and P. Meystre, Phys. Rev. A **81**, 053833 (2010)

[93] Y. Dong, J. Ye, and H. Pu, Phys. Rev. A **83**, 031608(R) (2011)

[94] K. Zhang, L. Zhou, H. Y. Ling, H. Pu, and W. Zhang, Phys. Rev. A **83**, 063624 (2011)

[95] L. Zhou, H. Pu, K. Zhang, X. Zhao, and W. Zhang, Phys. Rev. A **84**, 043606 (2011)

[96] J. Keeling, M. J. Bhaseen, and B. D. Simons, Phys. Rev. Lett. **105**, 043001 (2010)

[97] M. J. Bhaseen, J. Mayoh, B. D. Simons, and J. Keeling, Phys. Rev. A **85**, 013817 (2012)

[98] S. Gopalakrishnan, B. L. Lev, and P. M. Goldbart, Nature Physics **5**, 845 (2009)

[99] P. Strack and S. Sachdev, Phys. Rev. Lett. **107**, 277202 (2011)

[100] H. Ritsch, P. Domokos, F. Brennecke, T. Esslinger, Rev. Mod. Phys. **85**, 553 (2013)

[101] W. Heisenberg, Z. Phys. **43**, 172 (1927)

[102] B. Wu and Q. Niu, Phys. Rev. A **64**, 061603(R) (2001); B. Wu, R. B. Diener, and Q. Niu, Phys. Rev. A **65**, 025601(2002); B. Wu and Q. Niu, New J. Phys. **5**, 104 (2003).

[103] D. Diakonov, L. M. Jensen, C. J. Pethick, and H. Smith, Phys. Rev. A **66**, 013604 (2002); M. Machholm, C. J. Pethick, and H. Smith, Phys. Rev. A **67**, 053613 (2003); M. Machholm, A. Nicolin, C. J. Pethick, and H. Smith, Phys. Rev A **69**, 043604 (2004).

[104] C. M. Caves and G. J. Milburn, Phys. Rev. A **36**,5543(1987).

[105] L. Diósi, Phys. Lett. A **129**, 419 (1988).

[106] S. M. Barnett and P. M. Radmore, Optics Communications **68**, 364 (1988)

[107] M. O. Scully and M. S. Zubairy, *Quantum Optics*, (Cambridge University Press, 1997).

[108] C. W. Gardiner and P. Zoller, *Quantum Noise*, (Springer-Verlag Berlin, 1991)

[109] D. F. Walls and G. J. Milburn, *Quantum Optics*, (Springer-Verlag Berlin, 1994)

[110] C. Cohen-Tannoudji, J. Dupont-Roc, and G. Grinberg, *Atom-Photon Interactions* (Wiley, New York, 1992).

[111] D. Nagy, PhD Thesis, Research Institute for Solid State Physics and Optics, Budapest (2010)

[112] J. D. Miller, R. A. Cline, and D. J. Heinzen, Phys. Rev. A **47**, R4567 (1993).

[113] A. Polkovnikov, K. Sengupta, A. Silva, and M. Vengalattore, Rev. Mod. Phys. **83**, 863 (2011)

[114] R. Thom, *Structural Stability and Morphogenesis*, (Benjamin, London, 1975).